INVESTIGATION OF PROCESSES INVOLVED IN QUASI-ELASTIC AND Δ EXCITATION REGION WITH $(e, e'p)$ REACTION ON ^{12}C NUCLEI

BY MAHESH KUMAR YADAV

A dissertation submitted to the

Graduate School—New Brunswick

Rutgers, The State University of New Jersey

in partial fulfillment of the requirements

for the degree of

Doctor of Philosophy

Graduate Program in Physics and Astronomy

Written under the direction of

Ronald Ransome

and approved by

_____

_____

_____

_____

New Brunswick, New Jersey

May, 1997

ABSTRACT OF THE DISSERTATION

Investigation of processes involved in Quasi-Elastic and Δ excitation region with $(e, e'p)$ reaction on ^{12}C nuclei

by Mahesh Kumar Yadav
Dissertation Director: Ronald Ransome

We have studied the ^{12}C$(e, e'X)$ reaction with an incident electron energy of 705 MeV and electron scattering angle of 34.4°. A large solid angle detector, the LAMPF BGO ball, was used to detect protons, pions, deuterons, photons, and neutrons in coincidence with the electron. The electron energy loss was varied from 40 to 450 MeV, thus covering kinematical regions from quasi-elastic scattering to the $\Delta(1232)$ resonance.

The main focus of the thesis is a study of the Δ region with one or two protons in coincidence with the electron. A simulation program, ENIGMA, was used to model various reactions leading to emission of one or more protons plus neutrons or pions. We found that only two channels were required to reproduce the energy spectra and angular distributions of the $(e, e'p)$ final state: $(e, e'p\pi)$ and $(e, e'pnn)$. The two nucleon final state $(e, e'pn)$ was less than 10% of the cross section.

The peak of the $\Delta(1232)$ resonance for various coincidences was found to be close to the position of the inclusive spectrum, except for the $(e, e'pp)$ reaction where it increases to the highest measured values in energy loss, in contrast to proton induced reactions. The cross section for $(e, e'pp)$ was found to be small and does not appear to result from direct two nucleon decay of the $\Delta(1232)$ resonance.

In the quasi-elastic region we found that the kinetic energy spectrum of the proton

could be reproduced by a combination of 80% $(e, e'p)$ and 20% $(e, e'pn)$. We were not able to determine whether or not the pn final state was due to final state interactions or two nucleon absorption.

Acknowledgements

Completing the Ph.D. to me was not as much a learning experience in Physics as to develop discipline, skills and critical thinking for carrying through a lengthy project and most importantly finishing to a good conclusion. This exercise gave me realistic picture of my abilities which will definitely help me in facing the world. I am thankful to many persons – wonderful and otherwise – who helped me in overcoming many of my shortcomings.

I like to thank my thesis advisor Ron Ransome for his guidance and patience throughout the course of this research. I appreciate for giving me independence and for never getting mad at me. I bet there were more than one reason for being dissatisfied with me.

Many thanks to Gerfried Kumbartzki for teaching me C programming and solving many computer problems anytime – day or night. He always has a solution to any problem! I also enjoyed hiking with him and sharing his adventures throughout the world.

Thanks to the people at Mainz for all their help. Most importantly thanks to Eddy Offermann who gave me so much of his time for transfering the spectrometer computer code into my program. It is difficult to imagine completing the thesis without the critical help.

Thanks to Charlie Glashausser for giving me the opportunity in working at TJNAF where I met interesting persons such as Stan Majewski, Steve Christo and Brian Kross who provided me insights in solving the hardware problems and for many interesting conversations.

Many thanks to computer personnel in CERN and to John Maraffino from Fermi Lab who provided solutions via e-mail for learning of GEANT program.

Dedication

To my parents

and

my sisters Vidya and Satya

Table of Contents

List of Tables

List of Figures

Chapter 1

Introduction

1.1 Scattering Experiments

Most experiments with the objective of studying nuclei are done by exciting the bound nucleons in nuclei or by scattering experiments. Some of the other types of experiments are based on the study of decay of nuclei. In scattering experiments the probe, consisting of electrons, pions, or light nuclei, impinges on the target nuclei and outgoing particles or the probes are recorded. By studying many such events, an understanding of the inner dynamics of the nucleus can be obtained. As we study smaller distances, according to the de Broglie principle, one must use probes with larger momentum. With larger energy probes one can also eject nucleons or excite nucleon resonances, giving additional means of studying the nucleus.

1.2 Scattering Experiments in Nuclear Physics

Most of the experiments in nuclear physics rely on the scattering of beams of electrons, pions, protons, or nuclei on a nuclear targets. The scatterer usually excites the nucleons in the nucleus which then decays into the ground state by emitting gammas or even breaking up the nucleus into smaller nuclei. These scattering experiments fall in the domain of low energy nuclear physics. In this region it is possible to study the mean-field due to nucleons in the nuclei, the shell model and collective properties.

Intermediate energy scattering uses higher energy beams to probe even smaller distances, of order the size of a nucleon. The energy transferred to the nuclei is large enough to remove one or more nucleons from the nucleus. Detecting the scattered probe or/and byproducts from the nucleus helps us to understand the structure of

nuclei. Using even higher energy probes enables us to study the nucleon itself. The effects at these very high energies range has been experimentally studied in detail and can be well explained by QCD (quantum chromodynamics).

QCD is considered to be the exact theory of strong interactions in which the nucleon can be understood to be made of constituent quarks and gluons. Unfortunately, QCD is tractable only at very short distances where QCD can be expanded perturbatively. At the distance of a nucleon the perturbation expansion of QCD breaks down and even non-perturbative QCD studied with the help of enormous computing power can barely explain the few nucleon system. On the other hand, at low energies the nucleus can be readily explained by the mean field generated by nucleons. The intermediate energy lies in between these two extremes.

1.3 Inelastic Electron Scattering
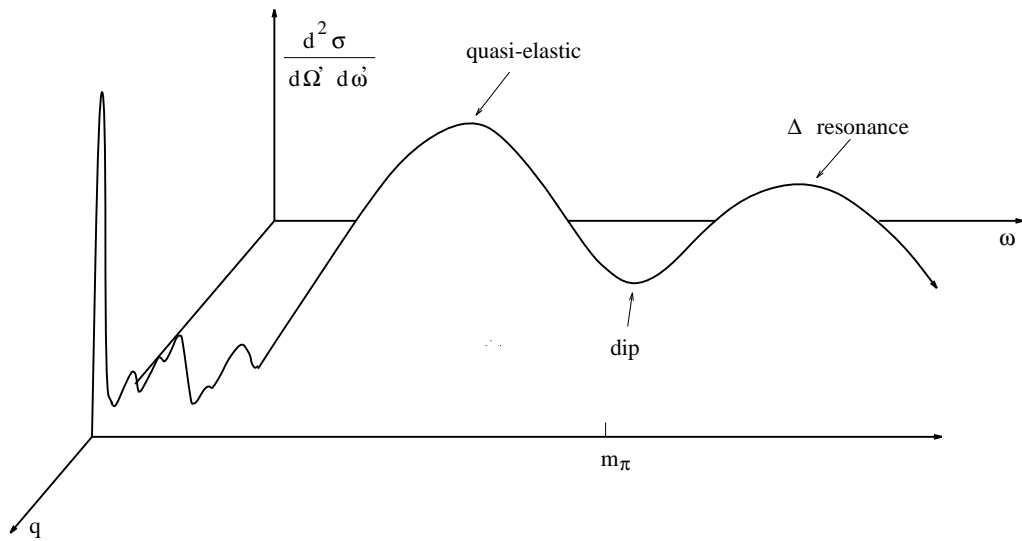
Figure 1.1: Typical cross-section for inelastic electron scattering showing various resonances. m_π is the mass of pion. ω and $\vec{q}$ are the energy loss and momentum transfer from the electron.

In the intermediate energy range, electron scattering in the inelastic region can be broadly classified into four regions. These regions can be easily seen when the cross-section is plotted in energy transfer and momentum transfer as in figure 1.1. The regions are described as follows:

1. At low energy transfer, the cross-sections consist of sharp spikes due to excitation of bound nucleons in the mean field of nucleus.

2. Giant resonances: At higher energy transfer, the energy absorbed by the nucleon is sufficient to leave the nucleus, but via quasi-bound states. This give rise to narrow resonance peaks called giant resonances.

3. Quasi-Elastic peak: Beyond giant resonances lies a large and broad peak where the nucleons struck by virtual photons are emitted without passing through any quasi-bound state. The energy and angle of the nucleon is approximately the same as expected for scattering from a free nucleon.

4. Delta region: The energy transfer in this region is high enough to excite the nucleon to $\Delta(1232)$ isobar. In terms of valence quark model, the excitation of nucleon results in flipping of the spin of the valence quark to spin $\frac{3}{2}$ and isospin $\frac{3}{2}$ state.

5. The region between QE scattering and the Δ resonance is simply known as the "dip" region. The cross section is much larger than a simple extrapolation from QE scattering and the Δ resonance would predict, indicating that other non-resonant physical processes may contribute significantly around the dip region.

1.4 Quasi-Elastic Region

The broad peak forming the QE resonance can be simply explained by assuming the nucleus to be a non-interacting Fermi gas [1, 2]. The kinematics for the QE region can be then given by,

$$\omega = \frac{(\vec{q} + \vec{k})^2}{2m_N} - \frac{\vec{k}^2}{2m_N} + \bar{\epsilon} \tag{1.1}$$

where $\vec{k}$ is the momentum of nucleon in the target nuclei, $\vec{q}$ is the momentum transfer from electron and m_N is the mass of nucleon. It is interesting to note that in the case of elastic scattering from a proton, we expect a spike at $\omega = q^2/2m_N$ as there is no Fermi momentum associated with a single free nucleon.

For any given nucleus, $\bar{\epsilon}$ and k_F (Fermi momentum) can be appropriately chosen to fit the experimental cross-section. The parameter $\bar{\epsilon}$ is related to the correlations of the nucleons in the nucleus.

The experimental cross-section for a wide range of nuclei from $^6\text{Li} - ^{208}\text{Pb}$ gives a remarkably good fit to non-interacting Fermi gas model with $\bar{\epsilon}$ and k_F appropriately chosen for each case [3]. For these nuclei $\bar{\epsilon}$ increases from 17 to 44 MeV and k_F varies from 169 to 265 MeV. This range of values of $\bar{\epsilon}$ and k_F are in reasonable agreement with the theoretical estimates. Hence the QE region was considered to be basically understood with minor modifications such as inclusion of final state interactions and using a finite temperature Fermi gas model to remove the sharp cut off of the energy of the nucleus.

However, as more detailed electron scattering experiments were performed, it was found that while the cross-section from the transverse part of the virtual photon agreed with experimental values, the longitudinal part agrees only for ^3He and significantly overestimated for all other nuclei. For instance, in ^{12}C at a given kinematic condition the longitudinal part was experimentally seen to be quenched by 40%. The longitudinal and transverse separation of (e, e') cross-section is possible because in electron scattering with the one photon approximation, a model independent cross-section can be obtained in the following form:

$$\frac{d^2\sigma}{d\Omega_{e'}d\omega} = \frac{4\pi}{M_T}\sigma_M\left[v_L R_L(\vec{q}, \omega) + v_T R_T(\vec{q}, \omega)\right] \tag{1.2}$$

where,

$$\sigma_M = \frac{\alpha^2 \cos^2(\theta/2)}{4E_0^2 \sin^4(\theta/2)}$$

$$v_L = \left(\frac{q^2}{\vec{q}^2}\right)^2$$

$$v_T = \frac{1}{2}\left(\frac{q^2}{\vec{q}^2}\right) + \tan^2\frac{\theta}{2}$$

M_T is the mass of target nucleus, kinematic variables $\vec{q}$, ω are momentum transfer and energy transfer respectively, four vector, $q^2 = \vec{q}^2 - \omega^2$, and σ_M is the Mott cross-section. E_0 and θ denotes the initial energy and the scattering angle of electron respectively.

$R_L(\vec{q}, \omega)$ and $R_T(\vec{q}, \omega)$ represent the longitudinal and transverse response functions respectively. These two response functions contain all possible information that can be obtained from (e, e') inclusive scattering.

The response functions are related to form factors by the following expression [4]:

$$R_L(\vec{q}, \omega) = \frac{A}{|\vec{q}|} G_E^2(q^2) \frac{\vec{q}^2}{q} f_L(\vec{q}, \omega) \tag{1.3}$$

$$R_T(\vec{q}, \omega) = \frac{A}{|\vec{q}|} G_M^2(q^2) \left(\frac{q^2}{2m_N^2} \right) f_T(\vec{q}, \omega) \tag{1.4}$$

f_L and f_T are dimensionless (reduced) response functions and $G_E(q^2)$ and $G_M(q^2)$ are form factors describing the distribution of charge and magnetic moment of nucleus.

One of the ways to explain the suppression of the longitudinal cross-section while retaining the Fermi gas model of nucleus is to reduce $G_E(q^2)$ with respect to $G_M(q^2)$. Noble [5] and Sick [6] proposed the swollen-nucleon model for nucleons in nuclei. By considering an enhancement of the charge radius of a nucleon by 30% in the nuclear medium has the desired effect of reducing the anomalous moment $G_E(q^2)$. This prescription could explain the longitudinal cross-section but also gave an enhancement to transverse cross-section due to a corresponding increase in $G_M(q^2)$. The experiments, however, suggested that the radius of nuclei may increase at most by a few percent.

When, in addition to the electron, one also detects an outgoing nucleon in coincidence, two additional response functions are present. One of them results from an interference between the longitudinal and transverse components of the nuclear electromagnetic current and the other from interference between the two transverse components. The kinematics from $(e, e'p)$ are shown in Figure 1.2. The coincidence cross section is given by

$$\begin{aligned} \frac{d^4\sigma}{d\Omega_{e'} d\Omega_p d\omega dE_p} &= \frac{4\pi}{M_T} \sigma_M \left[v_L W_L(\vec{q}, \omega, \theta_p, E_p) + v_T W_T(\vec{q}, \omega, \theta_p, E_p) \right. \\ &\quad + v_{LT} W_T(\vec{q}, \omega, \theta_p, E_p) \cos(\phi_p) \\ &\quad \left. + v_{TT} W_{TT}(\vec{q}, \omega, \theta_p, E_p) \cos(2\phi_p) \right] \end{aligned} \tag{1.5}$$

Where v_L and v_T are given above,
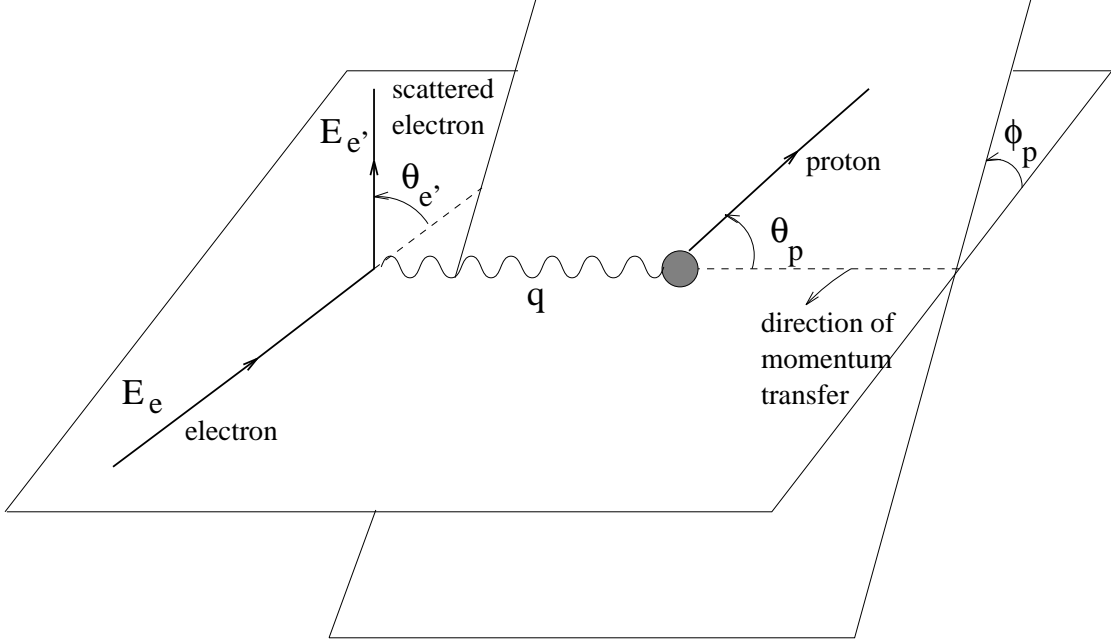
Figure 1.2: Feynman diagram for the electron scattering from nucleus with one outgoing proton in one-photon exchange approximation.

$$v_{LT} \quad = \quad \frac{1}{\sqrt{2}} \left(\frac{q^2}{\vec{q}^{\,2}} \right) \sqrt{\frac{q^2}{\vec{q}^{\,2}} + \tan^2 \left(\frac{\theta_e}{2} \right)} \tag{1.6}$$

$$v_{TT} \quad = \quad \frac{1}{2} \left(\frac{q^2}{\vec{q}^{\,2}} \right) \tag{1.7}$$

So far none of the theories consistently agree with experiments. By far the most successful model is that of Mulders [7] which considers the scattering in terms of a struck quark in a six quark environment. This seems plausible because there is significant overlapping of two nucleons in the nuclei. For instance the calculation shows 40% overlapping of a nucleon with other nucleons in ^{12}C. As a result, the magnetic radius increases by 30% while the charge radius changes by only 5%. The calculation is also consistent with (e, e') and $(e, e'p)$ cross-sections.

1.5   Delta Region

The $\Delta(1232)$ is the the simplest excitation of the nucleon [8]. From the kinematics of electron scattering, the resonance can be seen at $\omega \approx \sqrt{q^2 + m_\Delta^2} - m_N$. A free Δ is a very short lived particle reflected by the large decay width of $120 \, \mathrm{MeV}$. It decays mostly

π or π*

Δ

N

π*

N

(a)

N

π

(b)

π or π*

π*

(c)

Δ

π or π*

N^{-1}

(d)
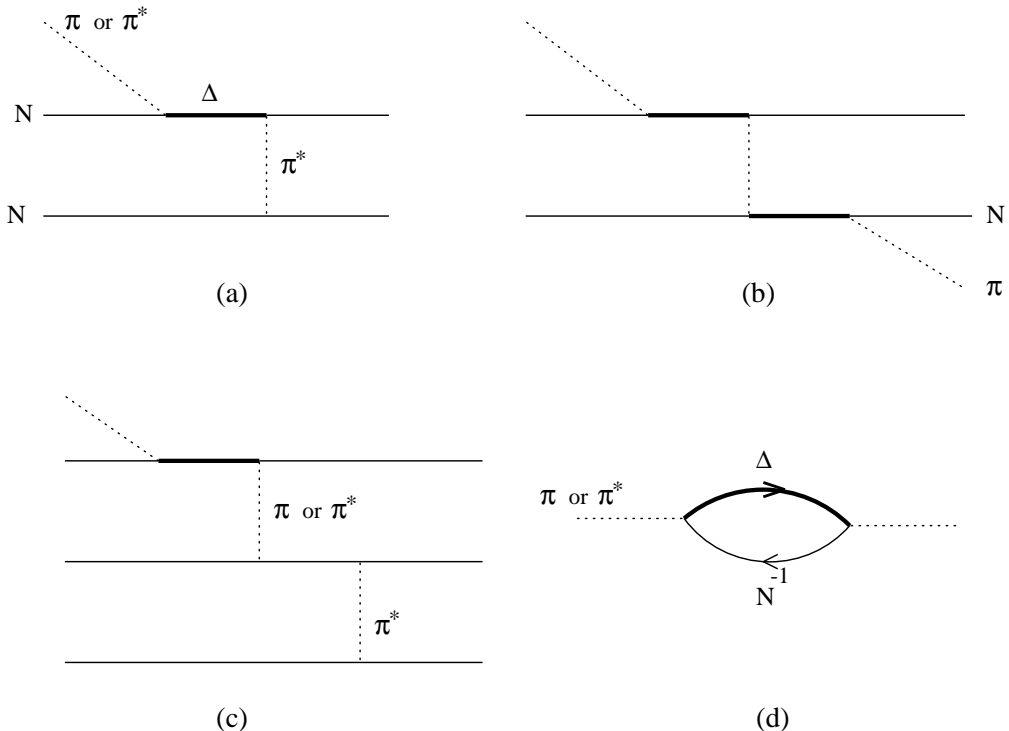
Figure 1.3: The generic diagram for virtual pion (π^*) or real pion (π) induced reactions can manifest itself in many different reactions. The virtual pions can be considered to be produced from Single Charge Exchange reactions such as (p, n), $(^3\mathrm{He}, \mathrm{t})$, $(^{40}\mathrm{Ar}, ^{40}\mathrm{Cl})$, $(^{40}\mathrm{Ar}, ^{40}\mathrm{K})$ etc. The pions are shown by dotted lines, nucleons by solid lines and Δ by thick solid lines.

(a) represents the pion absorption on a quasi-deutron reactions which is present in $\pi^+ d \to pp$ or (π, NN) reactions. A real pion absorption by a single nucleon is kinematically forbidden.

(b) The delta formed from the absorption undergoes an elastic collision with other nucleon, $\Delta N \to \Delta N$. It may be present in Double Charge Exchange reactions (DCX) such as (π^+, π^-)

(c) is the pion absorbed by three nucleons. There could be "genuine" three-body absorption if all the pions exchanged are virtual. If Δ decays to real pion followed by quasi-deutron absorption. Such reactions are categorized as Final State Interactions (FSI) and are not genuine three-body absorption.

(d) The Δ created from the pion absorption, interacts with the hole (N^{-1}) and may result in reducing the mass giving rise to the shift of the resonance. This reaction is also responsible for coherent pion production.

as $\Delta \to \pi N$ and $\Delta \to \gamma N$ with branching ratios of 99.4% and $\sim 0.6\%$ respectively. The resonance is also symbolized as $P_{33}(1232)$ because the pion-nucleon interacts or decays in a $l = 1$ state with $I = \frac{3}{2}$ and $J = \frac{3}{2}$.

We are interested in investigating if the basic properties of the Δ particle are changed in nuclear matter compared to when it is free. We can expect some modifications due to following reasons:

1. The Fermi momentum and binding effects have similar effects on broadening and shifting as in the QE region. For instance, the width of the Δ resonance from the $^{12}C(e, e')$ data [9] for various beam energies is seen to about 250 MeV. This is primarily due to the Fermi motion[*]

2. The Δ decaying to a low energy nucleon ($< 2k_F$) will be suppressed due to Pauli-blocking. From the Pauli principle, the decaying nucleon from a Δ cannot decay into a state already occupied by another nucleon in the nucleus.

3. In the nucleus there is another channel, $\Delta N \to NN$, which is available for the decay of Δ. This process plays a dominate role in pion absorption which proceeds through $\pi N N \to \Delta N \to NN$ because the pion cannot be absorbed by a single nucleon.

4. Creation of a Δ also creates a hole with similar quantum numbers. The Δ-hole pair can be coupled to each other as Δ propagates through nuclei. The self energy term changes the effective mass of the Δ—very much like in QED mass renormalisation – which results in shifting of the Δ-peak. This process can also lead to coherent pion production through $\Delta + N^{-1} \to \pi$.

5. The Δ may propagate for a longer time by scattering elastically on a nucleon in the nucleus as $\Delta N \to \Delta N$ reaction.

---

[*]Using the Fermi-width, k_F for ^{12}C and free delta width to be 221 MeV/c and 120 MeV respectively. Assuming distribution is Gausssian, the combined width is $\sqrt{221^2 + 120^2} \approx 251$ MeV. Note that the correct distribution for Δ resonance is given by Breit-Wigner resonance and not a Gaussian.

1.5.1 Investigation of Interactions From Hadron-Nucleus Experiments

We shall now give some experimental evidence to the expected interactions stated above. The hadrons are strongly interacting and therefore a hadron probes primarily the surface of the nucleus, but have much bigger cross-sections than electro-magnetic probes. Experiments with hadron probes have played a leading role in the understanding of the Δ in the nuclear environment in last 15 years. The experiments were mainly done at LAMPF, KEK (Japan), Saturne (France) with pion, proton, or light nuclei beams.

With a real pion beam, one can study elastic scattering, inelastic scattering, and absorption. In the pion absorption reaction there are no pions present in the final state and therefore the energy of $\approx 140\,\mathrm{MeV}$ (m_π) is absorbed in the nucleus.

The strength of the $\Delta N \rightarrow NN$ reaction can be estimated from the $\pi^+ d \rightarrow 2p$ cross section. The cross-section for ${}^3\mathrm{He}(\pi^+, 2p)$ is $\approx 1.5\sigma_{\pi^+ d \rightarrow 2p}$ and can be simply explained by the pion interaction with the quasi-deutron in the ${}^3\mathrm{He}$ [10]. The ${}^3\mathrm{He}$ can be considered to as 1.5 (T=0) quasi-deutron pairs. Further studies from $(\pi, 2N)$ on light and heavy nuclei shows that the angular distribution of protons is similar to protons in the $\pi + d \rightarrow 2p$ reactions. However, in heavier nuclei less than half of the cross section is due to the $(\pi, 2N)$ reaction, suggesting that pions could be absorbed by more than two nucleons.

The nucleus can also be studied using virtual pions produced by charge exchange reactions such as (p, n), $({}^3\mathrm{He}, t)$, $({}^{40}\mathrm{Ar}, {}^{40}\mathrm{Cl})$, $({}^{40}\mathrm{Ar}, {}^{40}\mathrm{K})$, etc. Such reactions can be considered to exchange the virtual π and ρ $(740\,\mathrm{MeV})$ mesons with the target nuclei. The study of the nucleus using virtual pions has an advantage that the momentum transfer $\vec{q}$ and the energy transfer ω are not constrained as in the case of real pion absorption reactions by:

$$q^2 + m_\pi^2 = \omega^2$$

. Hence, the response of the nuclei for different $\vec{q}$ in the Δ region can be studied by the single charge exchange reactions.

One such interesting result from virtual pions is that the peak of the Δ-resonance is shifted to lower energy. For instance, the ${}^{12}\mathrm{C}(\mathrm{He}, t)$ reaction at a lab angle of $0°$

with respect to the beam energy of ^{3}He at $2\,\mathrm{GeV}$, is shifted towards lower energy by $\approx 70\,\mathrm{MeV}$ compared to the $p(\mathrm{He,t})\Delta^{++}$ [11]. Such a shift has been seen in all the charge exchange reactions. The shift is even more pronounced in $(^{40}\mathrm{Ar},^{40}\mathrm{Cl})$ and $(^{40}\mathrm{Ar},^{40}\mathrm{K})$ reactions on ^{12}C target at $0°$ with a $780\,\mathrm{MeV/nucleon}$ beam energy [12].

The shift in the peak generated much attention as it indicates that the Δ may be lighter in the nuclear medium. However, the magnitude of the shift is seen to depend upon the incident energy which implies that the shift cannot be attributed to a simple modification of the Δ mass. Udagawa [13] was able to explain this $70\,\mathrm{MeV}$ downward shift by considering the following nuclear medium effects:

1. The effects of one body mean field on the target nucleon and excited Δ.

2. The effect of Δ-hole correlations particularly due to the π exchange interaction

Theoretical work based on these considerations shows that there are attractive correlations in the longitudinal channel $(\vec{S}\cdot\vec{q})$ which results in the downward shift. The transverse channel $(\vec{S}\times\vec{q})$ does not have these correlations.

To get further insight into the shifts in the Δ peak, the next step is to look for coincidence experiments which may help isolating the reactions contributing to the shift. Chiba $et\ al.$ [14] studied the coincidence reactions $(p,n\pi^+)$, (p,npp), and $(p,np\pi^+)$ on carbon and hydrogen targets. These reactions can be better visualized if (p,nx) is considered as (π^*,x). They observed that although the $(p,np\pi^+)$ reaction did not show appreciable shifts of the Δ peak, $(p,n\pi^+)$ and (p,npp) did show significant shifts which may largely explain the shift in the inclusive (p,n) reaction. The study also found that the invariant mass of the $p\pi^+$ in reaction $(p,np\pi^+)$ was $1207\,\mathrm{Mev}$ for the carbon target compared to $1225\,\mathrm{MeV}$ for the hydrogen target. This may prove to be first direct evidence of decrease in Δ mass. However since the $(p,np\pi^+)$ reaction does not contribute to the shift of the peak, it is not very certain if the low invariant mass is due to a decrease in the Δ mass or due to final state interactions(FSI) of the outgoing proton and pion.

1.6 Multi-nucleon Knockout

The study of $(\pi^{\pm}, p)$ reaction by McKeown et $al.$ [15] gave the first evidence that in the Δ region, pions are absorbed by more than two nucleons in the nucleus. The experiment used ^{12}C, ^{27}Al, ^{58}Ni, and ^{181}Ta targets and the Lorentz invariant cross-section plot in P_T versus rapidity gave an indication that the pions are absorbed by ~ 3 nucleons for ^{12}C increasing to ~ 5.5 for ^{181}Ta. This result generated further interest and more coincidence experiments were performed in order to determine the number of nucleons involved in the absorption.

Although $(\pi, 2N)$ for various nuclei has substantial strength, other components are also contribute significantly to pion absorption. For instance, a study by Burger et $al.$ [16] showed that $(\pi, 2N)$ in the Δ region for ^{58}Ni corresponds to less than 50% of the total absorption cross-section. The pion absorption itself constitutes about one-third of the total pion cross-section, for pion energies between 100 and 200 MeV [17].

In electron scattering the study of the $(e, e'p)$ reaction by Weinistein et $al.$ [22] and Lourie et $al.$ [27] suggests that more than one nucleon is involved in scattering process. For instance, Lourie studied the coincidence experiment $(e, e'p)$ in parallel kinematics on ^{12}C in the dip region $(\omega = 200 MeV, \vec{q} = 400 MeV/c)$. The missing energy spectrum $(\epsilon_m = \omega - T_p)$ shows nearly uniform continuum strength from 30 to 160 MeV which cannot be explained by a one-body process. The spike due to p-shell knockout and a broad bump over the continuum accounts for 20-30% QE process. Takaki [18] made a theoretical study of final state interactions to explain the experiment and claimed that even the two body process cannot fully explain such a large strength in missing energy. The contribution from three-nucleon absorption becomes more significant for missing energy > 80 MeV.

The same collaboration, Weinstein et $al.$ made a study in the QE region at three different momentum transfers $(\vec{q} = 585, 775, 827 MeV/c)$ and found that only 60% of the cross section can be explained by a one body processes. The missing energy spectrum ϵ_m showed a constant cross-section between 50 and 150 MeV, a region beyond single-nucleon knockout and below the pion threshold. They also found that two nucleon

correlations cannot explain strength beyond $\epsilon_m \approx 80 MeV$.

The theoretical work using microscopic calculations for medium size nuclei has been recently done at Valencia by Oset and Gent by Ryckebusch. The calculations from Oset [20] shows that for photon absorption in nuclei, the contribution of 3-body absorption is just 10% of the total. The strength of the three-body absorption initially increases with increasing photon energy reaching a maximum of 60% of the total direct absorption at $E_\gamma = 400\,\mathrm{MeV}$. In a recent experiment, Cross *et al.* [21] studied the $^{12}\mathrm{C}(\gamma, p)$ reaction for various photon energies, angular distribution of proton and wide acceptance of proton energy. The theoretical prediction, which includes $(\gamma, 2N)$, $(\gamma, \pi N)$, $(\gamma, 3N)$, and $(\gamma, \pi N N)$ processes, cannot explain the proton energy distribution for all photon energies and all angle of protons.

In our experiment we made a detailed study for $^{12}\mathrm{C}(\gamma^*, p)$ reaction in the Δ region. The analysis suggests that the three-body photon absorption is a larger component than calculated by the Oset group.

Chapter 2

Details of the Experiment

2.1 Introduction

This experiment was done at MAMI, Mainz, Germany. The data was taken in December of 1993. The experiment was performed with the aim of studying the ^{12}C$(e, e'$X$)$ reaction, where "X" denotes various hadrons or photons. The cross-sections of special interest were $(e, e'p)$ and $(e, e'pp)$. The electron beam energy was 705 MeV and the scattered electron was detected by the high resolution electron spectrometer at a scattering angle of $34.4°$.

The BGO ball detector identifies and measures the energy of the scattered byproducts from the nucleus: protons, deuterons, pions, photons, and neutrons. The BGO ball detector surrounded the target and therefore provided large angular acceptance for the scattered byproducts from nuclei.

The electron spectrometer had a momentum acceptance of $\pm 10\%$ of the selected central momentum. Six different central momenta were chosen so that entire region from quasi-free scattering to the $\Delta(1232)$ resonance could be studied.

2.2 Accelerator

2.2.1 Description of Working Principles

The MAMI accelerator (MAinz MIcrotron) is capable of producing a continuous beam of electrons with maximum energy of 855 MeV. The intensity of the beam can go up to 200 μA and has a duty factor of 100%. The schematic layout of the accelerator is shown in Figure 2.1. The beam originates from the electron gun with an energy of 100 KeV. This is fed to the injector (linear accelerator) where the electrons are accelerated to an
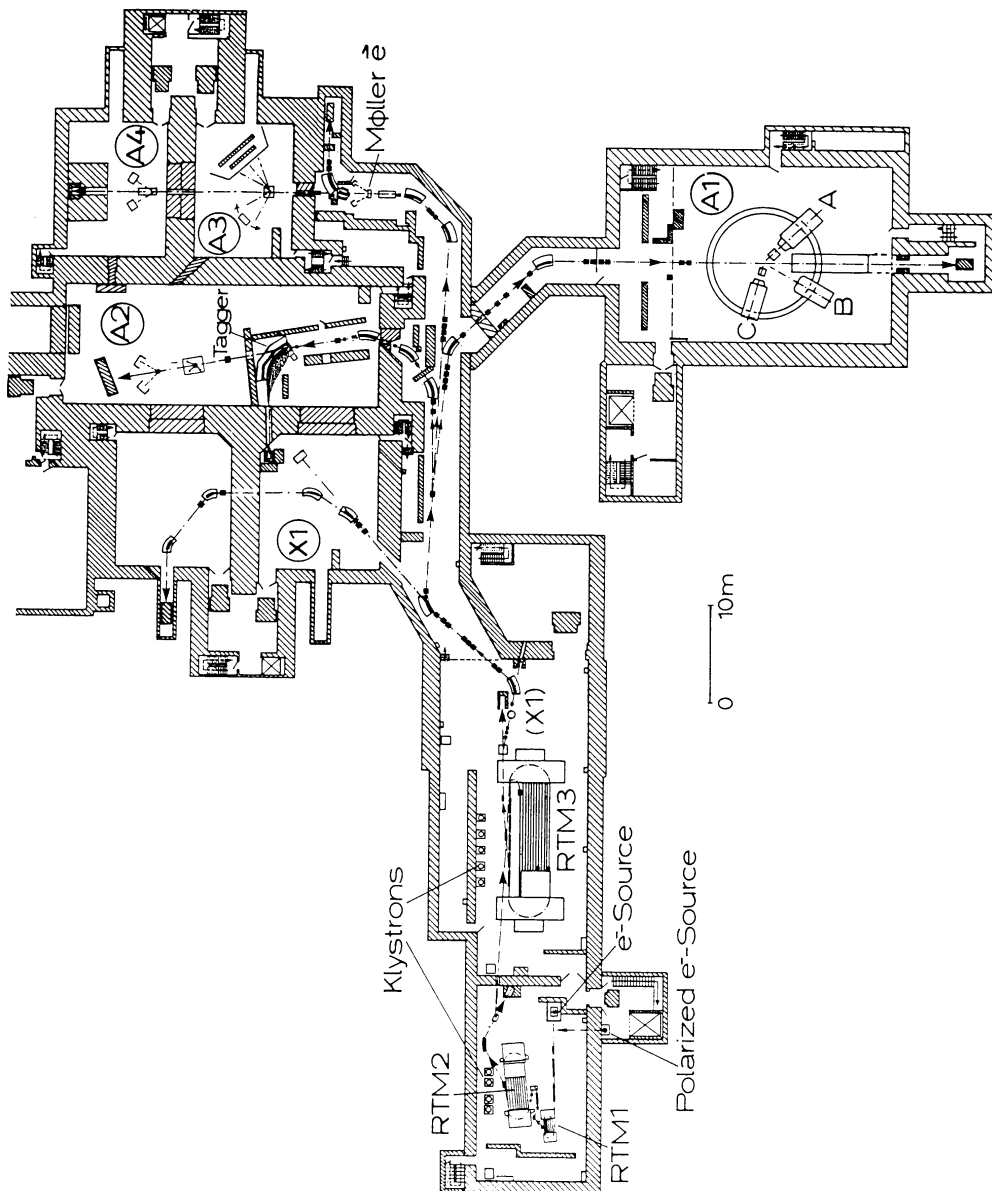
Figure 2.1: Outline of MAMI accelerator with various halls. RTM1, RTM2, and RTM3 are the three microtrons in cascade configuration used in accelerating the electrons.

energy of 3.5 MeV. From the injector the beam is injected to three microtrons one after the other. The accelerated electron energy at the exit of each microtron is 14 MeV, 180 MeV, and 855 MeV, respectively.

The microtron is essentially a linear accelerating element placed between two big dipole magnets. The purpose of each dipole magnet is to deflect the electrons by 180°. The electrons are accelerated in the accelerating structure then brought back to the same accelerating element repeatedly by the two dipole magnets. Thus electrons of different energies have different trajectories outside the accelerating element. However, in the accelerating element electrons with different energies are together in the same path and therefore accelerated simultaneously. This feature results in production of continuous beam.

The three microtrons have a similar designs and differ mainly in the size. As the electron energy increases from one microtron to the next, successively bigger dipole magnets are needed. In the third stage the dipole magnets are huge, weighing 450 tons, to keep the electrons on their race tracks. High field precision is necessary to guarantee exact recirculation with the right phase. This characteristic design also ensures a very low beam energy spread, typically < 200 keV.

The beam is then brought to experimental hall A1, one of the experimental halls, by series of beam deflections by dipoles and periodic focusing by quadrupoles.

2.2.2 Significance of High Duty Factor

The duty factor is a measure of the efficiency of an accelerator. In all of the accelerators, the accelerated particles are packed into bunches. Therefore the experiment receives the particles for only a fraction of the overall run time. The duty factor is defined as [23]:

$$
\begin{aligned}
\text{duty factor} \ &= \ \frac{\text{actual time beam of particles available to the experiment}}{\text{total time of the run}} \\
&= \ \text{duration of a bunch in seconds} \times \text{number of bunches/sec}
\end{aligned}
$$

Until recently there were not many accelerators with high duty factors. For example, Bates, SLAC, and the electron synchrotron DESY had duty factors of 0.1%, 0.04%,

5% respectively. The high duty factor implies that the electrons in the beam are less bunched and hence the accelerator is more efficient. For instance, for the same luminosity beam, an accelerator with a 100% duty factor has 100 times lower accidentals than a 1% duty factor machine. It is therefore crucial to have high duty accelerator to study coincidence experiments with electrons. The electron-nucleus cross-section is small because it interacts with nuclei primarily via the electro-magnetic interaction. To give some measure of the strength, the total absorption cross-sections for real photons (which also interact via the electromagnetic interaction) by protons in the Δ-excitation region is ~ 0.5 mbarns. In comparison, the total cross-section for the $\pi^+ p$ reaction in the same region is ~ 200 mb [24]. In this experiment, the cross section for 705 MeV electrons scattering from ^{12}C to an angle of $34.4°$ has a peak at the Δ region of ~ 10 nb/MeV-sr. The coincidence experiments $(e, e'\mathrm{X})$ will have even smaller cross-sections than the inclusive (e, e') reaction.

This experiment used a beam current of about 30 nA. The low beam current was required to keep the accidental rate, primarily due to low energy electrons from Møller (electron-electron) scattering, to an acceptable level.

2.3 Spectrometer A

The electron/hadron spectrometer [25] is capable of distinguishing various charged particles and determining their positions and momenta with a high resolution. The angular acceptance of Spectrometer A is 28 msr and the particles are detected within $\pm 10\%$ range of the chosen central momentum. The entire spectrometer can be moved from $18°$ to $160°$ on the left side of the beam. The position accuracy of the spectrometer is $0.005°$ with angular resolution better than 3 mrad. The momentum resolution, $(\delta P/P)$ is less that 0.01%. Some specific details of the spectrometer A are summarized in the Table 2.1

The spectrometer can be roughly divided into three sections. The first section is where the particle's position and momentum are determined by the charged particle optics. This is done by dispersing and imaging by magnetic fields and tracking by

spectrometer A	units	specification
magnet configuration		QSDD
maximum momentum	MeV/c	735
maximum induction	T	1.51
solid angle	msr	28
scattering angle range	deg.	$18 - 160$
length of central trajectory	m	10.75
momentum acceptance	%	20%
angle acceptance:		
dispersive plane	mrad	± 70
non-dispersive plane	mrad	± 100
momentum resolution (with retracing)		$\leq 10^{-4}$
angular resolution at target	mrad	≤ 3
position resolution at target	mm	$3 - 5$

Table 2.1: Salient features of Spectrometer A

Vertical Drift Chambers (VDCs). The second region consists of two planes of scintillator for timing purposes as well as for discrimination between pions and protons. The third region consists of Čherenkov detectors where electrons can be discriminated from other heavier charged particles and from cosmic rays.

Each section is described in some detail below. Details of Vertical Drift Chambers can be found in Richter's thesis [30]. Some description of offline ray tracing which improves the resolution of the position and momentum by an order of magnitude is described in Section 4.1.

2.3.1 Scintillator Detectors

There are two planes of Plastic scintillator behind VDCs, as shown in the figure 2.2. The two planes are segmented in 14 and 15 detectors which overlap each other. Signals from the segmented detectors are read on both sides by the photomultiplier tubes.

The first layer (behind VDCs) is 3mm thick and called the ΔE-plane. Pions and protons can be distinguished from each other using pulse height in the PMT of the ΔE-plane. This fact is utilized in making the triggers for various experiments. The second plane, called the ToF-plane, is 10 mm thick which is used for timing.

In the off-line analysis, the signal from both the sides of the scintillator detector can

Photomultiplier

light guide

Scintillator segment

ΔE plane

ToF plane
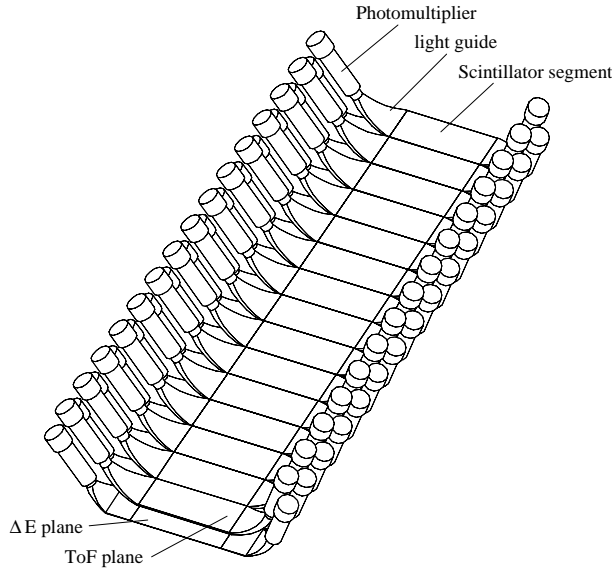
Figure 2.2: The Figure shows two Scintillator planes which are located between VDCs and Čherenkov detectors

be used for better particle discrimination as well as better time determination. The time measurement is further improved in offline by taking into account the path length of the particles from the target through the VDCs.

2.3.2 Čherenkov Detector

The Čherenkov counter is able to select the electrons over other heavy charge particles with nearly 100% efficiency. It is based on the principle that low energy photons are emitted from a charged particle traveling with a velocity greater than that of light in that medium. The Čherenkov radiation is emitted in a conical form similar to the wake in the lake caused by a moving boat. The condition for emission of the photons or Čherenkov radiation and its direction is mathematically given by,

$$v > c/n$$

$$\cos\theta_c = \frac{c}{vn}$$

Where v is the velocity of the particle, c is the speed of the light, n is refractive index of the medium, and θ_c is the direction of the Čherenkov photon with respect to the particle.

VUV Cherenkov detector

Sheilding

Vacuum Window

Plastic Scintillator

Vertical Drift Chamber (VDC)

Particle Tracks

Platform

©1993, Arnd P. Liesenfeld
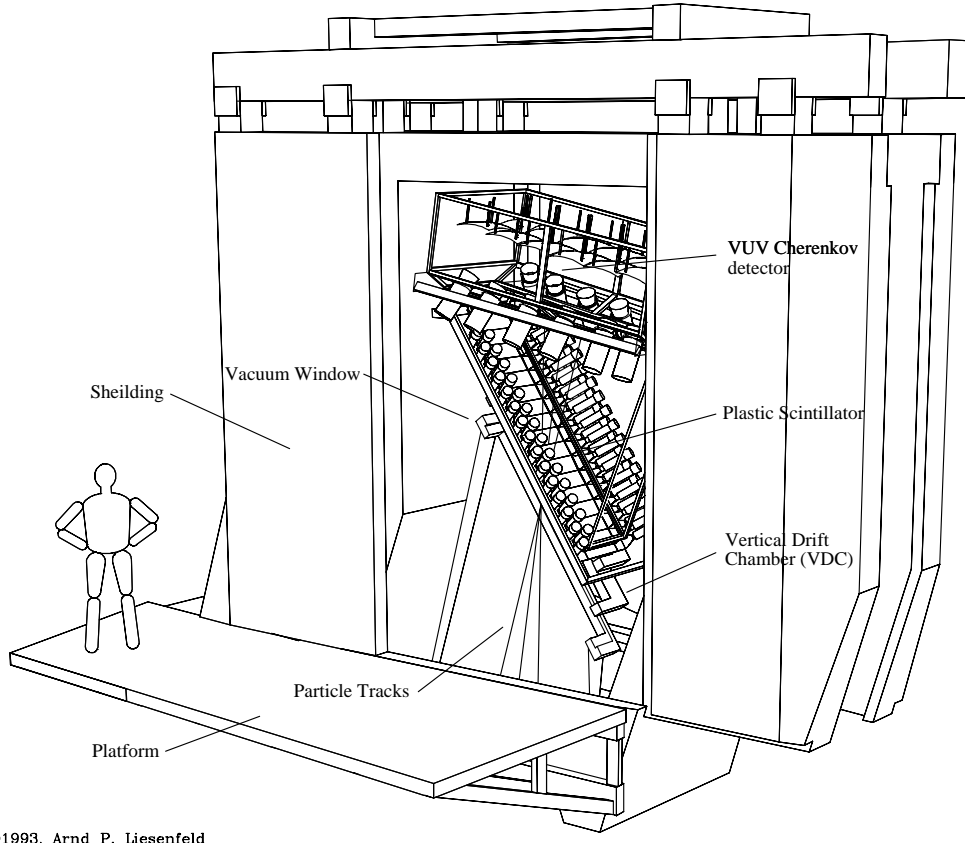
Figure 2.3: Upper part of Spectrometer-A showing the VDC, two scintillator planes and Čherenkov detector

We are able to select electrons over pions by choosing the medium such that only the electrons are able to emit the Čherenkov photons. We also utilize the direction sensitivity of the Čherenkov radiation to eliminate the accidental coincidences from cosmic rays because they travel in the opposite direction of the electrons.

In Spectrometer A, $4\,m^3$ of Freon 114 at atmospheric pressure and room temperature is used as the radiator gas for the Čherenkov counter. Under these conditions the refractive index of the gas is 1.001 in the ultra-violet region, which leads to the threshold (to emit the Čherenkov radiation) of $9\,MeV/c$ for electrons, and over $2.5\,GeV/c$ for pions.

The Čherenkov photons are collected and reflected by an array of twelve mirrors arranged in 2×6 fashion (see Figure 2.3). Each mirror focuses the light onto a PMT which has large cathode ($11\,cm^2$). Since the Čherenkov radiation is predominantly

UV, the mirrors are coated by aluminum which is covered with MgF$_2$ which has high reflectivity for UV. Each PMTs has a window which transmits UV light.

2.4 BGO Ball Detector

2.4.1 Overview of the Detector

The BGO ball detector, developed at Los Alamos [26], is used in this experiment to detect particles produced in the reaction, other than the primary electron. The BGO ball detector originally consisted of thirty detectors compactly arranged in such a way that the solid angle of each BGO detector as seen from the target remains the same. The structure is based on a simple arrangement of hexagonal and pentagonal shapes called a truncated-icosahedron (similar to a soccer ball) which can surround the target without any gaps. It consists of 12 pentagons (with equal sides) and 20 hexagons (with opposite sides of same length). Two of the pentagonal detectors were removed so that the beam pipe can pass through unobstructed. The closest distance of the detectors from the center (where the target is placed) is approximately six cm. The physical appearance of the BGO ball with μ-metal which encloses the photomultiplier tube (PMT) is shown in the Figure 2.4. In our experiment the BGO ball detector was further modified by removing two hexagonal detectors in the most downstream row to allow the scattered electron to reach the spectrometer. The other three downstream detectors were displaced further by about 1.5 cm from the target center to reduce the low energy electron background. The low energy electron background is further described in Section 2.4.3. The final arrangement of assembled BGO crystals with beam pipe and magnets is shown in the Figure 2.10

2.4.2 Single BGO Detector

Each of the hexagon and pentagon detector in BGO ball has the ability to detect protons, deuterons, pions, and high energy gammas with $\sim 100\%$ efficiency. Neutrons can also be detected with lower efficiency. The identification of various particles is possible because of the phoswich design, which consists of a 3 mm thick plastic scintillator
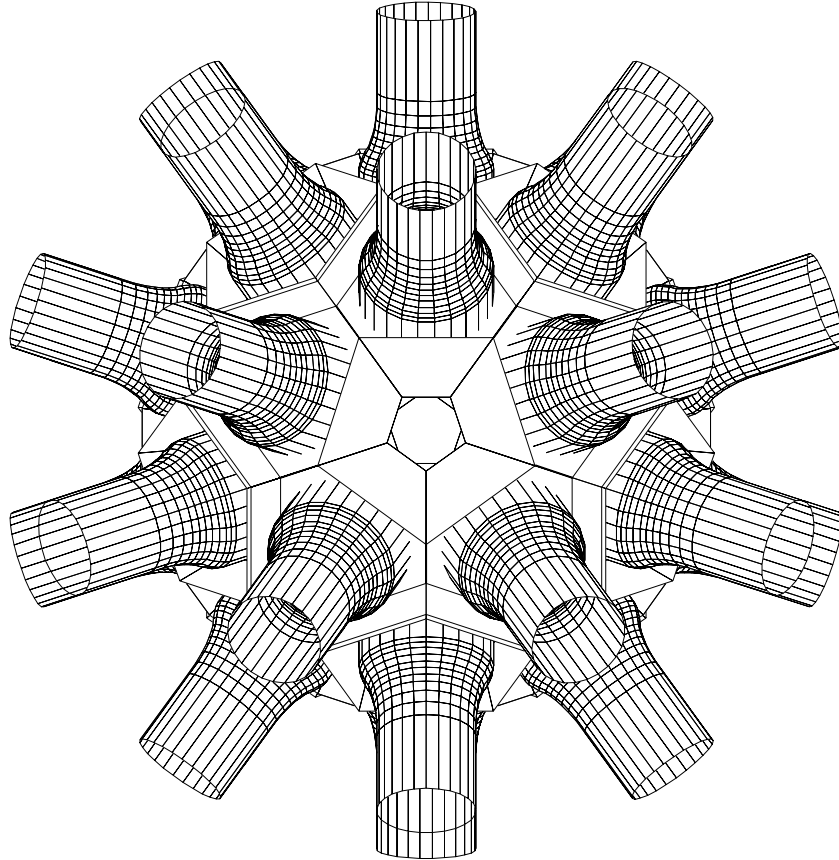
Figure 2.4: Physical profile of original BGO ball detector (shown without PMT)

(NE102A) attached to 5.6 cm thick BGO crystal which is then attached to a photo-multiplier (see Figure 2.5). The scintillator and BGO crystal are enclosed in a 0.5 mm thick nickel can to make it light tight. The nickel side of each metal enclosure facing the target is 0.05 mm thick. Some of the properties of plastic scintillator and BGO crystal are given in Table 2.2.

It is possible to identify the particles passing through the BGO detectors by knowing the energy deposited in the scintillator and the BGO crystal. The energy deposited in the plastic scintillator is proportional to dE (energy deposited in the scintillator) (energy loss from Bethe-Bloch equation). The rest of the energy is collected in the BGO crystal. Knowledge of dE/dx and the total energy helps in identification of the particle. The identification is more distinct when the energy loss of the particle is much larger than the minimizing ionization value. However, due to the finite thickness of the BGO crystals, particles with higher energy cannot be stopped in a crystal. In such

Phoswich design
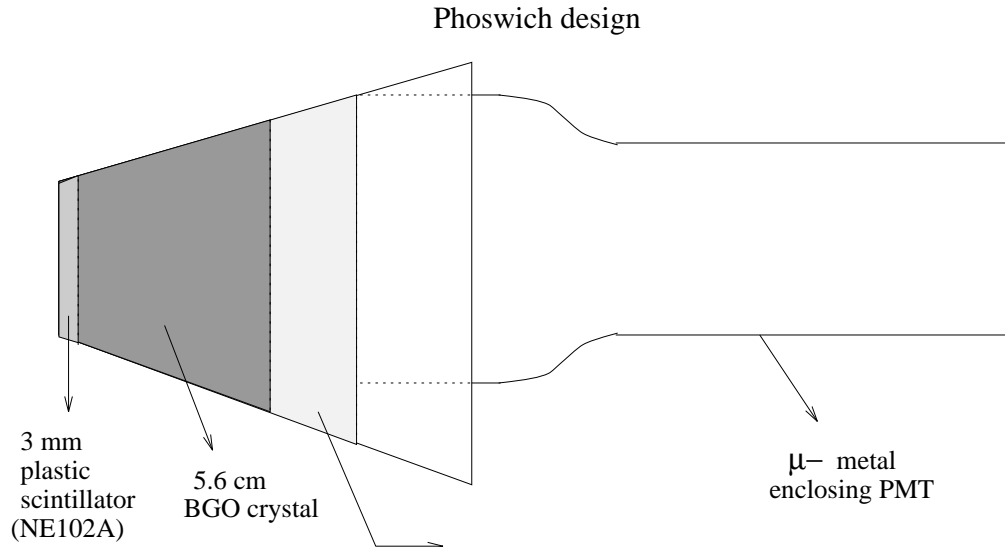
Figure 2.5: Anatomy of a BGO Detector

	Scintillator	BGO crystal
specification	NE102A (Plastic)	Bismuth Germanate
compound	CH (polymer)	$Bi_4Ge_3O_{12}$
density(gm/cm^3)	1.032	7.13
Radiation length (cm)	42.4	1.12
dE/dx (MeV/cm) (minimum ionizing)	1.95	9.2
index of refraction	1.58	2.19
non-hygroscopic	yes	yes
light yield (photons/MeV)	about 10,000	about 2800
light output decay time (ns)	10	300

Table 2.2: Some relevant properties of plastic scintillator and BGO crystal

cases, the total energy deposited is less than that of the particle. These particles can also be identified. The plot in Figure 2.6 shows the expected energy deposited (derived from Bethe-Bloch equation with the geometry of the detector) in the scintillator and the BGO crystal for protons, deuterons and pions. Each of the curves in the plot shows a decrease in dE/dx with increasing total energy. The sudden backward turn is at the point where the particles can no longer be stopped completely in the BGO crystal. Wider separation of curves signifies better separation and closer separation calls for careful calibration of energies for successful identification. The energy loss in the plastic scintillator and the BGO crystal is determined by recording the output pulse of the PMT, which is proportional to detected light. The signal from each PMT is
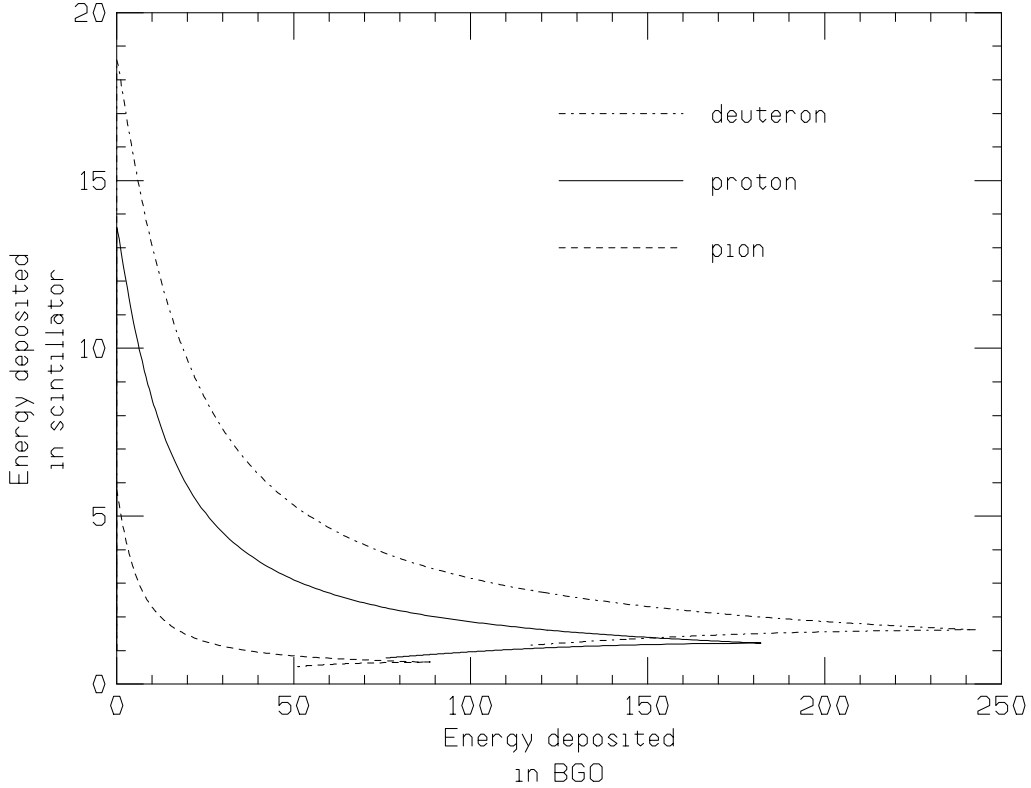
Figure 2.6: Expected energy deposited in scintillator and BGO crystal

fanned out into three signals which are attenuated and fed to three ADCs. Each ADC's

has different gate length which record integrated charge of the pulse from PMTs within

each ADC gate. I will call the three gates Short-gate, Long-gate and Delayed-gate. The

attenuators decreased the signal to 1/2, 1/8, and 1/4 for Short-, Long- , and Delayed-

gates which were required to place the integrated pulse in the acceptable range of the

ADCs. Figure 2.7 shows the typical placement of ADC gates with respect to signals

from scintillator and BGO Crystal. The Short-gate and Long-gate start at the same

time and had widths of about 85 ns and 580 ns respectively. The delayed gate is 2700 ns

wide and begins at the end of Long-gate.

Short-gate and Long-gate play the main role of identifying the particles whereas the

Delayed-gate is used to eliminate signals from multiple hits. The signal from a single

event decays exponentially and the gates were adjusted in such a way that the signals

into the different gates were similar in size. However we did not utilize the Delayed-gate

as the rates of particles detected in the BGO detectors was low and identification was

Scintillator signal (decay time 10 ns)

BGO crystal signal (decay time 300ns)

Short Gate (85 ns width)

Long Gate (580 ns width)

Delayed gate (2700 ns width)
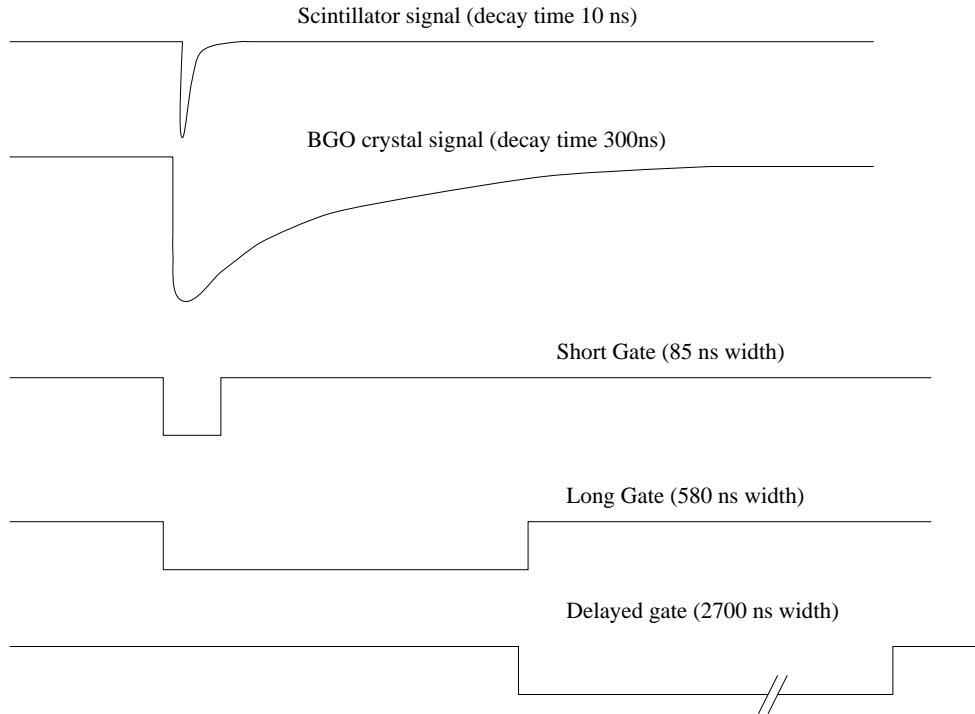
Figure 2.7: Typical Short, Long and Delayed gates with the signals from scintillator and BGO crystal in BGO detector.

fairly clean.

The light signal from the scintillator has a short decay time of 10 ns and was placed near the start of the Short-gate. Most of the signal from the scintillator is within the Short-gate ADC. The BGO crystal has a decay time of 300 ns and therefore part of the light output is measured by the short gate and a significant part is measured by the Long gate. Thus both the Short-gate and Long-gate contain a mixture of the signal from both the plastic scintillator and BGO crystal.

From the Short-gated and Long-gated ADCs, the individual scintillator and BGO crystal signals can be isolated, as described in section 4.3.1 and Appendix A. Figure 2.8 shows a typical two-dimensional plot of Short-gate (y-axis) and Long-gate (x-axis) from a single BGO detector. It can be seen that the events in the form of line (closest to the y-axis) are of particles stopped in the scintillator (also see Figure A.1). These events do not give any signal in the BGO crystal. Similarly the neutrals such as gammas or neutrons do not generate any signal in the scintillator. Therefore by transforming the plot to a coordinate system where the particles stopped in scintillator are along the
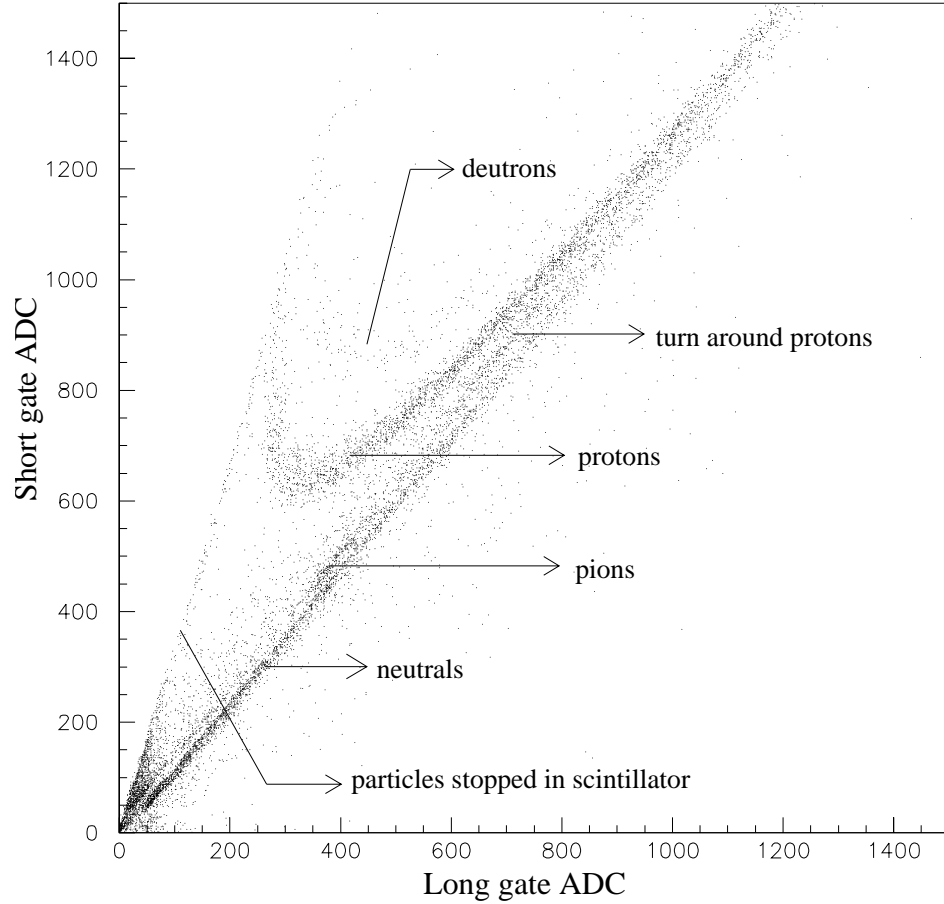
Figure 2.8: ADCs of Short-gate and Long-gate of one BGO ball detector)

y′-axis and the neutrals are along the x′-axis, we can separate the scintillator and BGO crystal signals.

After separation of the signals we did an energy calibration of the scintillator and BGO crystal signals. We made a two dimensional plot which was used for particle identification. We plotted energy deposited in scintillator vs. energy deposited in BGO crystal. In the plot, the pions, protons, and deuterons lay along the expected line for the respective particles as shown in the Figure 2.6. After proper energy normalization the plots for all BGO detectors were sufficiently similar to allow the same cut to be used for particle identification for all runs and for all the detectors.

2.4.3 Permanent Magnet Array

An array of six permanent magnets was glued outside the aluminium beam pipe and placed inside the BGO ball as shown in the Figure 2.9 and 2.10. The upstream edge of
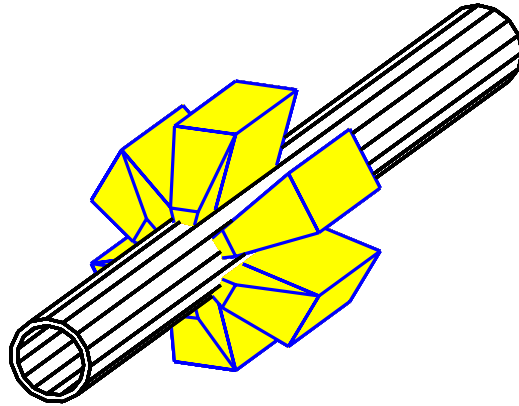
Figure 2.9: Six permanent magnets on the beam pipe

the magnets was aligned with respect to the target. The magnets covered half of the solid angle in the forward hemisphere. The purpose of introducing the magnets was to reduce the background due to low energy Møller electrons.

Møller electrons are produced by collisions of the beam electrons with atomic electrons. In the center-of-mass frame, the Møller (electron-electron) scattering has large cross-section for small angle collisions. In the lab frame this gives low energy electrons in the forward angles with respect to beam. Therefore to reduce the background a configuration of permanent magnets was designed which could deflect the low energy electrons back towards the beam pipe.

The magnets were made up of NdFeB (mainly iron) and the magnetic field between the magnets was 0.6 T. A GEANT (CERN Program Library W5013) simulation program showed that this configuration of magnets could reduce the background due to Møller electrons by a factor of 20. This helped in having manageable rates in the BGO detectors at forward angles. To further lower the rates, the BGO detectors at forward angles were pushed out giving a larger minimum angle.
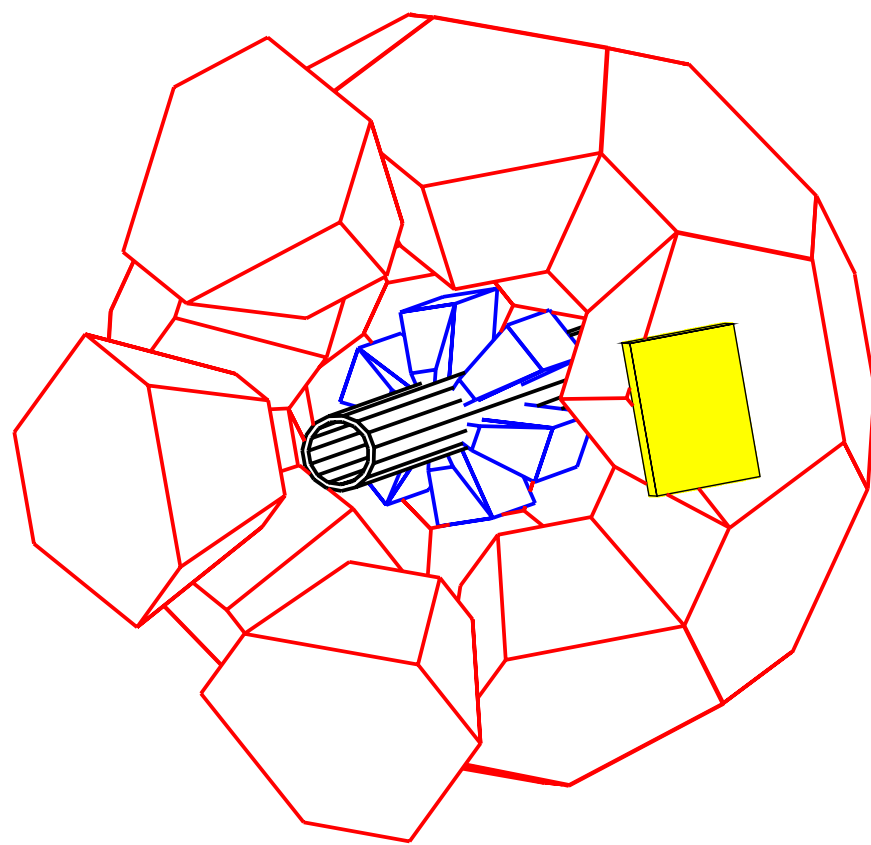
Figure 2.10: Active BGO ball detector elements are shown with the magnets on the beam pipe. The solid angle of the acceptance of scattered electron from spectrometer is shown as a rectangular grey area.

Chapter 3

Running the Experiment

The BGO ball with its electronics was brought from LAMPF before running the experiment. The electronics were augmented with the electronics of spectrometer-A, a data acquisition system and workstations where the functioning of various detectors could be monitored on-line. The data presented in the thesis were taken during November 12-29 in 1993.

The useful quantities in the data collected for the off-line analysis were analog to digital converter (ADC) (energy), time to digital (TDC) (time interval), scalers (rates) from various detectors and wire hits in the VDC chamber in spectrometer. Although the handling of the signals at the detector's end are usually fast (50-100 ns), the electronics at the higher end (where the ADC and TDC are calculated) usually takes a few microseconds to process. At an even higher level is the computer's CPU which processes and writes the information to the disk at the speed of a few milliseconds per event. Therefore, a selective trigger is needed to help reduce the volume of analog or logic signals being processed by the higher level electronics. This reduces the dead time* of the experiment.

To maintain clarity in describing the electronics, we roughly divide the electronics as follows:

- BGO ELECTRONICS: From analog signals of the 28 BGO detectors to measuring the ADCs, TDCs and scalers.

- VETO ELECTRONICS: The electronics for measuring the ADCs and TDCs from the analog signals produced by six veto scintillators behind the magnets.

---

*dead time is the fraction of time when data cannot be taken because the electronics at various levels are busy processing the data

- SPECTROMETER ELECTRONICS: Electronics in the electron arm spectrometer.

- Trigger and other electronics

The electronics related to the BGO and veto detectors are illustrated in Figure 3.1. The spectrometer and spectrometer trigger electronics were well studied before the experiment. Therefore, the spectrometer and trigger electronics are only briefly described at a level which is sufficient for understanding the experiment. The details of the spectrometer and its trigger electronics are described in detail in Richter's dissertation [30].

3.1 BGO Electronics

A particle passing through a BGO detector produces analog signals. Figure 3.1 shows that the analog signals from each BGO detector are connected to a linear fan out which splits the analog signal into three equal analog signals. One branch is utilized for measuring the ADCs, the other for TDCs, and the third for the BGO trigger. They are described sequentially in the following three paragraphs.

The **ADC** branch is divided further into three analog signals by linear fan outs. The analog signals are attenuated by 1/2, 1/8, and 1/4 before being input to short-gated, long-gated, and delayed-gated Fast Encoding Readout ADC (FERA), respectively. The signal size and the different gates are shown in perspective in Figure 2.7. The ADCs measure the integrated signal or charge for the duration of the gate and signals differing in size must be properly attenuated to put the integrated charge from the signal in the measurable range.

The other branch of the analog signal from each BGO detector is converted into a logical signal by a discriminator. This logic signal is used as a **TDC** stop (for stopping the time measurement). The time measurement is started for all the TDC's by a common start. The logic signal from the discriminator, which also goes to TDC stop, is connected to **scaler**. This is used to measure the rates of signals from each BGO detector during the entire run time – independent of the trigger or during the dead-time when the electronics is busy.

The third bunch of analog signals from the 28 BGO detectors is summed by connecting into fan ins. This summed signal is converted to one logic signal by the discriminator with a threshold of 30 mV. The threshold is carefully chosen such that an analog signal produced by a particle passing through the BGO detector will produce the logic signal. This logic signal defined the **BGO Event**.

In the rest of this section we explain the reason for adding the delay cables shown in the Figure 3.1. The reason for the delay after the gate-generator is trivial due to the placement of the delayed gate after the long gate.

The common-start was created from the coincidence of the Spectrometer-Event and the BGO-Event signals. The BGO-Event signal was generated much earlier than the Spectrometer-Event because the BGO ball was just six centimeters away from the target. The Spectrometer-Event was created when the charged particle hits the scintillator planes which was about 11 m away from the target. Hence to create a common-start, the BGO-Event was delayed such that it arrived in coincidence with the Spectrometer-Event signal. The common-start started the TDC and triggered the generation of ADC gates.

Since the TDC-start precedes the TDC-stop signal and ADC signals are expected to arrive within the ADC gates, long delays were added to all 28 channels of the TDC-stop and the signals feeding the analog-splitter to create the ADC signals.

3.2   Veto Electronics

The plastic scintillators behind the permanent magnets produce a signal when a particle is able to reach the scintillator after passing through a magnets. The signal from each scintillator is split by a fan out into two signals. One of the signals is used to measure the ADCs and the other signal is converted to a logic signal by a discriminator which is used as a TDC stop. As in the case of the BGO electronics the TDC is started by the same common start. Hence we are able to measure the strength and timing of the signal from any of the scintillators behind the magnets.

3.3 Trigger and Others

The trigger is responsible for generating the common-start signal which activates the higher level electronics such as ADCs and TDCs. The PLU (Programmable Logic Unit) was responsible for generating the trigger based on the BGO Event and Spectrometer Event signals. The output from the PLU was written in the data for every event so that the trigger information could be extracted during the off-line analysis. We can interpret the PLU output as consisting of three triggers. One is the coincidence trigger which is generated when both a BGO Event and a Spectometer Event signal are present. This is also the most important trigger for our experiment as it indicates the detection of an electron in the spectrometer and another particle in the BGO ball. The other two triggers are generated when a BGO Event or a Spectrometer-Event signal reached the PLU. However, both these Event signals were prescaled by 10 before reaching the PLU. This means that the trigger for singles was created once for every 10 events for BGO-singles or Spectrometer-singles.

The prescaling of 1:10 was necessary to have the rate of singles recorded to be comparable with the rate of the coincidence events. The singles contain mostly accidentals. For instance, the rate of cosmic rays striking the paddles (scintillators of the spectrometer) which constituted the spectrometer singles trigger was 80 Hz, whereas genuine events were about 1–3 Hz. The BGO singles rates were also high because of the Møller electrons and close proximity of the target to the 28 BGO detectors.

The singles trigger helped in checking for consistency and diagnostics. The spectrometer single trigger can be used to determine the (e, e') cross-section which can be checked with the cross-sections from other experiments. The BGO singles can help to check if BGO detector rates are comparable to each other and if the detectors are functioning properly.

3.4 On-line Monitoring and Data Collection

With such a complex electronics and detectors, it is essential to monitor the electronics and detectors during the run of the experiment. Each run lasted for about one hour.

During the run the data were written to disk and were also accessible for the on-line analysis though various computer workstations. Various spectrometer quantities such as the currents in sextuple and quadrupole magnets, water flow and temperature, and voltages for the four drift chambers were also monitored independently of the data acquisition system. Likewise, in the BGO ball, the plots of Short gated ADCs vs. Long gated ADCs (like the Figure 2.8) were plotted to see if the proton events were reasonably placed. The beam intensity was measured periodically by a Faraday cup and other devices. The scalers, TDCs and ADCs for all various BGO detectors, veto scintillators were also monitored to check for consistency and stability.

Sometimes the background rates increased when the momentum acceptance of spectrometer was changed to another region or due to a change in the beam profile. This required changing the beam current or the voltages of some of the BGO detectors to make them less sensitive to background.

The data collected from the BGO events and the spectrometer events were written on disk separately. Only after the run, were the two files were combined by the "event builder" program. The data files were written sequentially for all the runs and brought to Rutgers University for analysis.
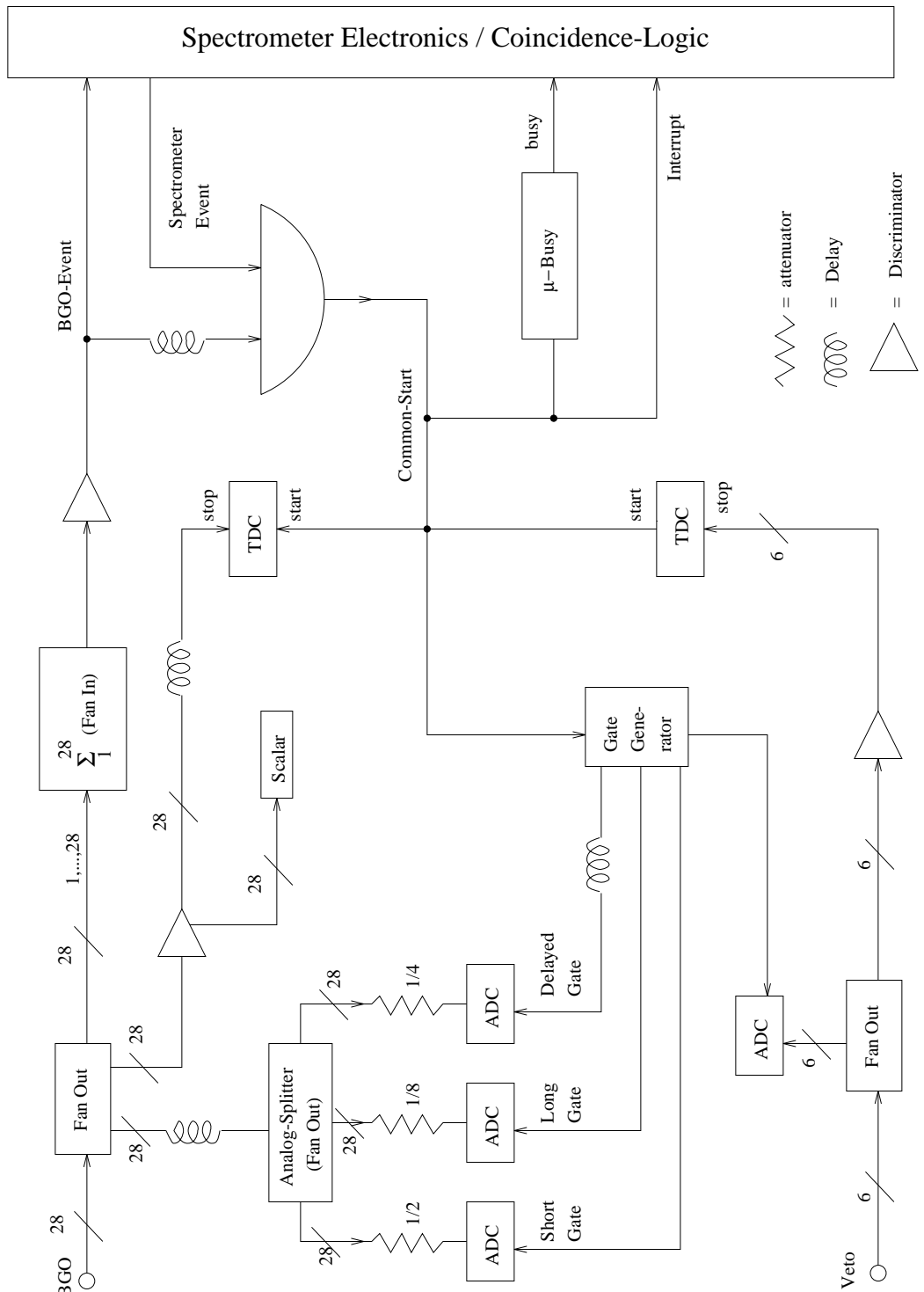
Figure 3.1: Electronics showing the BGO, Veto and trigger

Chapter 4

Data Analysis

Before the cross-sections can be obtained, we had to determine the "unfolding" constants and calibrate each BGO detector for particle identification. TDC and Čherenkov cuts were also determined to remove background events.

The software "MECDAS", which was used to monitor the detectors on-line and record the raw data, could also have been used for off-line analysis. Instead we decided to use our own programs to analyze because MECDAS was a fairly large program to export, written in C++ language and used graphical packages developed at MAMI which would require dependency on Mainz personnel.

The spectrometer code which was already incorporated in MECDAS was obtained in a FORTRAN version from E. A. J. M. Offermann. This code evaluates the position and momentum of the particle from the wire hits in VDC's of the spectrometer. This spectrometer code was throughly tested before running the experiment.

The data were collected in ten single density exabyte tapes which consisted of about 400 data files (or runs). The entire data set was rewritten by the program "decode" which converted these data to a stream of two column numbers corresponding to the addresses and measured value of each channel. The columns of addresses and numbers were interrupted by blank lines which separated the events. A subset of the addresses (which also were in the structure* variables of the data acquisition program) which were utilized for the off-line analysis is shown in the Table 4.1 with some comments. The entire data set was compressed and written in this form on a single double-density exabyte tape.

---

*A structure is a collection of one or more variables grouped together under a single name for better organization of complicated data. They are defined in C and Fortran. In Pascal they are called records.

address name	comments
bgo93.a.det.sync_info	
bgo93.a.det.trigger.cerenkov.energy[0] ⋮ ⋮ bgo93.a.det.trigger.cerenkov.energy[11]	ADCs from Čherenkov counters
bgo93.a.det.vdc.x1[0] ⋮ ⋮ bgo93.a.det.vdc.x1[400] bgo93.a.det.vdc.x2[0] ⋮ ⋮ bgo93.a.det.vdc.x2[416] bgo93.a.det.vdc.s1[0] ⋮ ⋮ bgo93.a.det.vdc.s1[320] bgo93.a.det.vdc.s2[0] ⋮ ⋮ bgo93.a.det.vdc.s2[336]	TDC from VDC of first x-plane TDC from VDC of second x-plane TDC from first s-plane (oblique) TDC from second s-plane
bgo93.bgo.sgate[0] ⋮ ⋮ bgo93.bgo.sgate[29] bgo93.bgo.lgate[0] ⋮ ⋮ bgo93.bgo.lgate[29]	ADCs of the BGO detector in Short-Gate ADCs of the BGO detector in Long-Gate
bgo93.bgo.tdc[0] ⋮ ⋮ bgo93.bgo.tdc[29]	TDCs of the BGO detector

Table 4.1: Important variables of structure used in the off-line analysis

The analysis program was developed and updated sequentially by adding the code for incorporating the spectrometer program, removing the backgrounds from the Čherenkov detector, determination of "unfolding" constants, calibration of all BGO detectors, polygon cuts for the particle identification, TDC cuts, and veto TDC cuts for good event selection.

All of the analysis was done by making "ntuples" from the main analysis program. The ntuples were visualized by PAW software (a CERN Program Library Q121) and the parameters such as unfolding constants, calibration constants, particle identification cuts, and TDC cuts were evaluated for each good run. These parameters were stored in "database" files which were read by the updated main-analysis program. Finally we prepared ntuples with quantities used for the final analysis. Ntuples are a type of reduced-data-set which could be combined with other ntuples, visualized, and analyzed by PAW software. The PAW software could read "kumac" files where commands were listed sequentially and Fortran subroutines could be written which easily read ntuples to create presentable histograms.

The sequence in this chapter basically follows the order of the analysis that was done.

4.1   About the Spectrometer Program

The spectrometer code is a complex program and therefore was developed before the experiment. The program utilizes the particle-transport optics to construct the tracks and calculate the momentum and the angular position of the scattered particles.

Some test experiments were carried out to evaluate the "transfer coefficients" which are used by the spectrometer code. The test experiment included runs with the collimator being covered by sieve-like solid-angle defining slits. In these runs, the electrons are elastically scattered by a hydrogen target so that the energy of the scattered electron is known from the kinematics. Using these test runs, the spectrometer code is refined using a χ^2 minimization procedure that compares the evaluated quantities with the known solid-angle and momentum of the particle.

The resolution of the spectrometer is greatly improved by using these transfer co-
efficients. These coefficients can be used for subsequent experiments to determine the
momentum and scattering angle of the scattered particles. A good introduction can be
found in Reference [31], and further details about the spectrometer design can be found
in [32].

4.2   Background Reduction from Čherenkov Detector

In this experiment, the major source of background comes from cosmic rays and misiden-
tification of pions as electrons. Both backgrounds can be removed by the Čherenkov
counters with $\sim 100\%$ efficiency. In a typical run, the good event rate was a few/sec
compared to a cosmic ray rate of $\sim 80\,\mathrm{Hz}$. The cosmic rays barely produce any signals
in the counter because the reflecting mirrors in the Čherenkov detectors were specifi-
cally oriented to see the Čherenkov light cone from the charged particle traveling in an
upward direction (the direction for the scattered electrons). To remove the pions the
density of the gas in the Čherenkov detector is adjusted so that the speed of pions is
less than c/n, the condition for producing no Čherenkov light.

The background was removed by summing all 12 ADC's from Čherenkov counter
and placing a cut as shown in Figure 4.1. Some initial runs did not have any pedestal
and therefore pedestals had to be determined and subtracted from each event. The
pedestal corrected spectrum of the Čherenkov radiation was stable for the all runs and
therefore one cut was sufficient to remove the background.

4.3   Analysis of Calibration Runs

The calibration runs were performed to determine the "unfolding" constants and most
importantly, the energy calibration of the BGO detectors. The elastic scattering reac-
tion ${}^1\mathrm{H}(e,e'p)$ was ideally suited for the calibration as it provided protons with known
energy. This was done by having the electron beam, E_e, of energy $705\,\mathrm{MeV}$ incident
on a $2\,\mathrm{mm}$ thick CH_2 target (see Figure 4.2). The choice of angle of scattered electron,
$\theta_{e'}$ detected by spectrometer A, defines all other kinematic variables. For instance, the
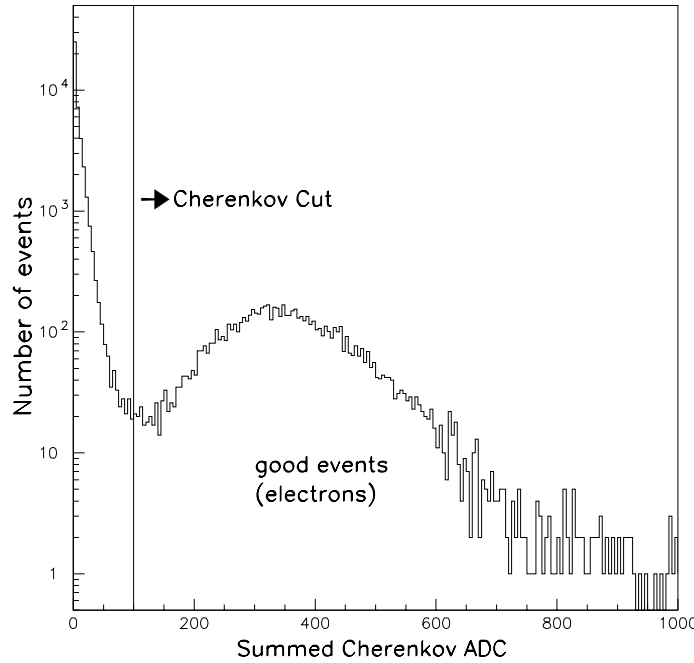
Figure 4.1: Cherenkov cut from a data sample in Delta region

kinetic energy of the protons T_p and the angle of scattered proton θ_p are related to E_e and $\theta_{e'}$ as follows:

$$T_p = E_e^2 \left/ \left[\frac{m_p}{2\sin^2\frac{\theta_e'}{2}} + E_e \right] \right.$$

$$\cos\theta_p = \frac{T_p\left(1 + \frac{m_p}{E_e}\right)}{\left[T_p^2 - 2T_pM_p\right]^{\frac{1}{2}}}$$
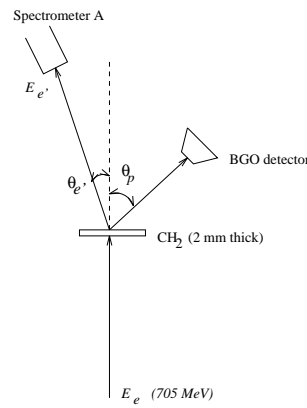
Figure 4.2: Schematic Experimental Setup For Calibration Run

There were two sets of calibration runs, each with different angles for Spectrometer

A and the BGO detector as shown in Table 4.2. In the first set of calibration runs

Calibration Run from elastic reaction ^{1}H$(e, e'p)$		
Target used	2 mm thick or 226 mg/cm^2 CH$_2$	
Incident electron Beam Energy	705 MeV	
Calibration Set Up	**I**	**II**
Angle of Spectrometer A	28°	58°
scattered electron momentum	626.6 MeV/c	496.2 MeV/c
scattered electron momentum range	563.9–689.2 MeV/c	446.6–545.8 MeV/c
Angle of BGO detector	66.4°	47°
scattered proton energy	15.8–141.1 MeV	159.2–258.4 MeV

Table 4.2: Setup parameters for the calibration run

spectrometer A was placed at an angle of 28° and the BGO detector at 66.4°. The BGO ball was dismantled so that single BGO detectors could be conveniently placed at the required angle. For each single calibration run a different BGO detector was used. The first set of calibration runs was carried out for all BGO detectors used in the BGO ball. The array of magnets was also included to give a realistic estimate of the background to be expected in the normal run.

Calibration for all the BGO detectors was essentially done by the first setup in which the energy of the protons was in the range 15.8–141.1 MeV. However, for the sake of completeness, we also calibrated a selected few BGO detectors with higher energy protons. These selected BGO detectors were positioned at smaller scattering angles and therefore these detectors were expected to have higher count rates, including the background rates. We observed in earlier tests that the energy gain shifted due to change in the background rates and therefore having calibrations for two different background rates could help our understanding of the calibration of BGO detectors. The second set of calibration had the angle of the spectrometer A and the BGO detector at 58° and 47°, respectively, so that protons between the energy range 159.2–258.4 MeV were detected in coincidence with the scattered electron.

4.3.1 "Unfolding" Procedure

This procedure is essentially a transformation of points in a plot of the Short Gate ADC vs. Long Gate ADC to a frame where neutral particles are along the x-axis and the charged particles stopped in the scintillator are along the y-axis.

As discussed earlier in Section 2.4.2, the Short Gate ADC and Long Gate ADC contain a mixture of signals from the scintillator and the BGO crystal in the BGO detector (see Figure 2.7). A charged particle stopped in the scintillator gives a signal from the scintillator only, whereas a neutral particle such as a γ or neutron usually generates no signal in the scintillator but gives a signal in the BGO crystal.

A high energy γ ray interacts with material primarily via pair production and on an average the γ ray will convert into a pair after one radiation length. The 3 mm scintillator is only 0.0068 radiation length, therefore it is extremely unlikely that a high energy photon will produce any signal. However, the photon will almost certainly be detected in the 5.6 cm BGO crystal which is 6.3 radiation lengths.

The neutrons are detected by the BGO detector primarily via the $np \to pn$ reaction. The efficiency of the BGO crystal to detect neutrons is estimated to be at most 20% for $T_n > 100$ MeV and decreasing rapidly [33] with decreasing energy. Because of the small thickness of the scintillator, less than 1% of neutron will interact with the scintillator.

The upper plot of Figure 4.3 shows a dark curved line from protons. The two faint but distinct lines enclosing the protons are due to events with only a scintillator signal (charged particle stopped in the scintillator) or only a BGO crystal signal (the neutral particles). These two lines are transformed into the x and y axis of another frame as shown in the lower plot of the same figure.

In data analysis the two lines were defined by choosing two points along these lines which defined the line of transformation. The derivation of the transformation is given in Appendix A.

Using this transformation, or "unfolding", procedure we have separated the signals from the scintillator and BGO crystal. This transformation procedure is done for each BGO detector used in BGO ball. After the "unfolding" constants are determined for all
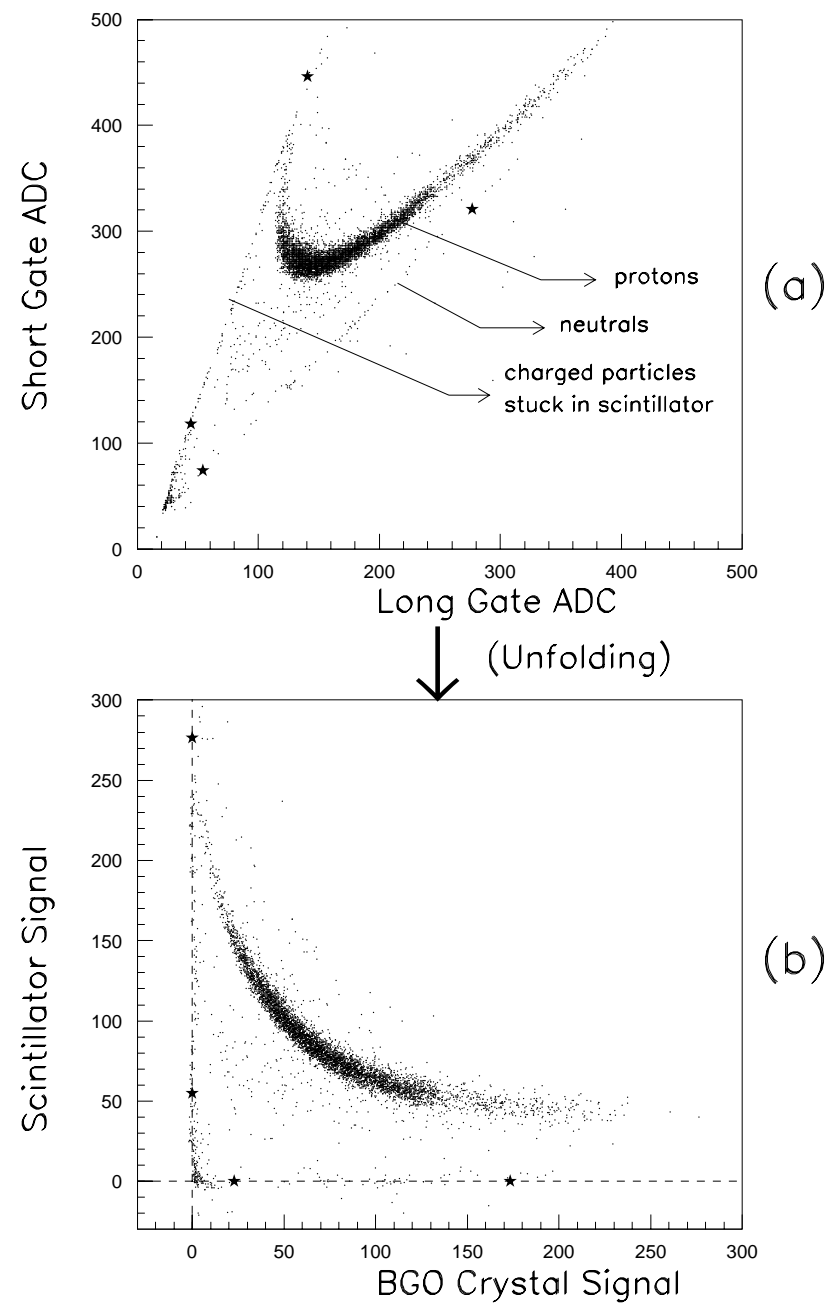
Figure 4.3: Upper plot shows the raw data and the bottom shows the transformed plot

the BGO detectors, we were ready to calibrate signals from the scintillator and BGO crystal to determine the energy deposited in the respective components of the BGO detector.

4.3.2   Energy Calibration

In the calibration run, the scattered protons pass through 2 mm of aluminium (the thickness of beam pipe) to the BGO detector. The proton looses energy, primarily due to ionization in the aluminium beam pipe, scintillator, and BGO crystal. For the setup **I**, the energy of protons does not exceed 185 MeV and therefore the protons fall along one curve as shown in the 2-D plot of Figure 4.3 (b).

Protons passing through a material interact with atomic electrons, and to lesser extent the nuclei, which leads to ionization. The electrons eventually produce low energy photons by de-excitation. In the case of BGO crystal the electrons de-excite by going from the conduction band to the valance band, whereas in the case of the scintillator a the molecular de-excitation emits the photons. The signal produced from the photons is proportional to the energy lost by the protons. The "unfolding" procedure discussed in the previous section isolates the scintillator signal and BGO crystal signal from the mixture. To calibrate, we plotted the scintillator signal vs. BGO crystal signal for the proton of known energy. We then compared this with the expected energy deposited in the scintillator and BGO crystal by the proton in a similar energy range. We calculated the average energy deposited in the scintillator and the BGO crystal from protons within a narrow energy range by a simple GEANT program.

In the GEANT program, we generated protons which were passed through 2 mm of aluminium to the BGO detector—just like the calibration run. We chose protons in four different energy ranges to get a better estimate of the calibration constants. Table 4.3 shows the values of those energy ranges along with the average energy deposited in the scintillator and BGO crystal from the GEANT calculation. Experimentally, the energy range of proton is determined by the choice of the cuts in the scattered electron's energy spectrum. From the elastic scattering of ^{1}H$(e, e'p)$, the energy of proton, $T_p = (E_e - E'_e)$. The calibration is done by evaluating the two constants which convert the signals to

the corresponding energy, summarized as follows:

$$\text{Energy deposited in scintillator} \quad = \quad \text{Constant}_1 . \text{ scintillator signal}$$

$$\text{Energy deposited in BGO crystal} \quad = \quad \text{Constant}_2 . \text{ BGO crystal signal}$$

where the signals are obtained by:

$$\left.\begin{array}{l}\text{scintillator signal}\\[2mm]\text{BGO Crystal signal}\end{array}\right\} \longleftarrow \text{ ``unfolding'' procedure} \longleftarrow \left\{\begin{array}{l}\text{Short Gate ADC}\\[2mm]\text{Long Gate ADC}\end{array}\right.$$

The constants$_{1,2}$ are adjusted in such a way that the proton events in one energy range lie on the corresponding rhombus point as shown in the Figure 4.4. The last two plots in the same figure show protons to have a comet-like appearance. The nucleus of the comet lies nicely on the required point. The tail of the comet is due to low energy protons scattered from the carbon nucleus. The tail sweeps across the other rhombus points, thus verifying the calibration constants. The first two plots have a wider band of protons which is smeared with the tail of low energy protons and therefore these plots are not as convincing as the other two plots. Nevertheless, an overall check of the proton curve for each of the four energy ranges helped to better determine the calibration constants.

This procedure to determine the calibration constants was done for all the BGO detectors used in BGO ball. In a few cases, we had to redetermine the unfolding constants to get better calibration constants so that the protons lay on the expected points and had the low energy tail along the other expected points.

Energy range of scattered electron,E'_e. (MeV)	Energy range of Protons. (MeV) ($T_p = 705 - E'_e$)	Energy deposited in scintillator. (MeV)	Energy deposited in BGO Crystal. (MeV)
657-660	45-48	5.20	32.02
650-655	50-55	4.48	39.90
640-645	60-65	3.73	51.48
620-630	75-85	2.86	70.95

Table 4.3: The calibration energy ranges
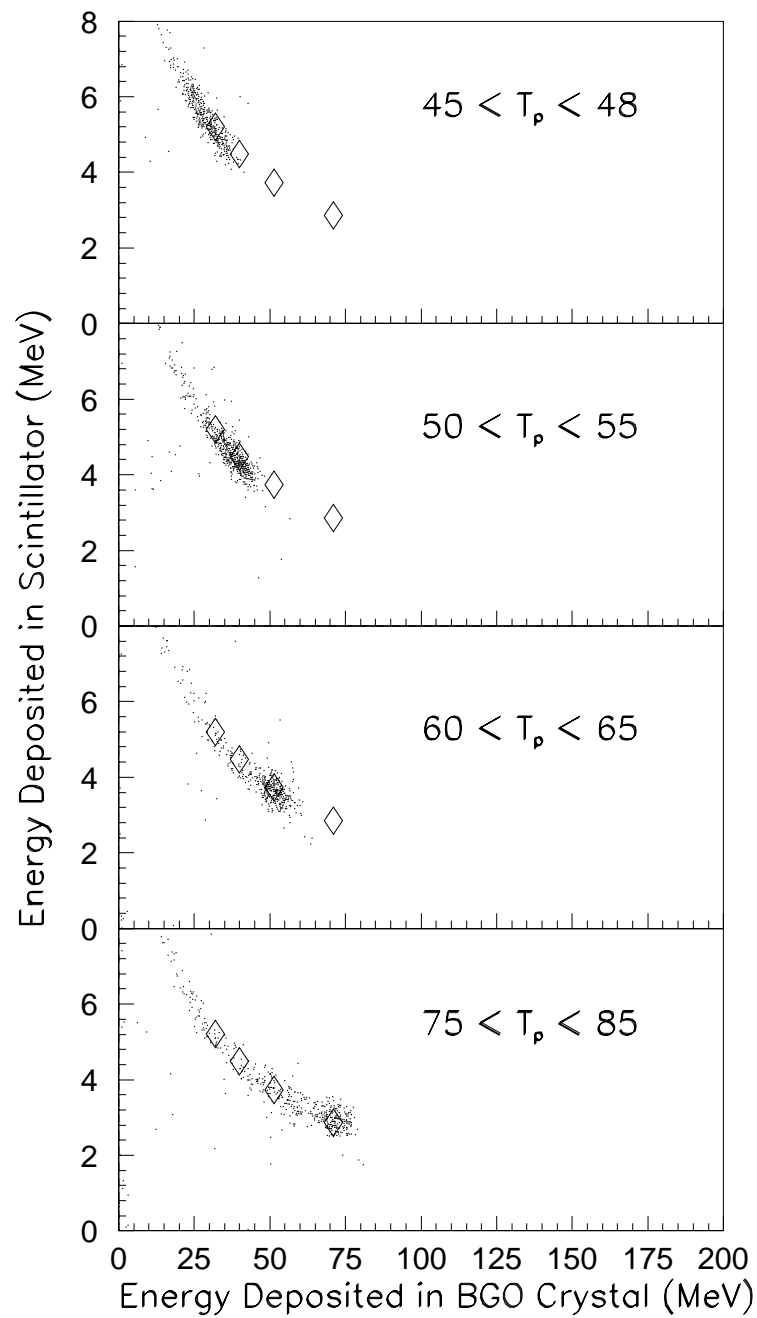
Figure 4.4: Calibration with protons with different kinetic energies, T_p (MeV)

4.3.3 Particle Identification in BGO Detector

After the "unfolding" procedure, the particles can be easily identified in a 2-D plot of the signal from scintillator vs. that from the BGO crystal as protons, particles stopped in the scintillator, neutrals (photons and neutrons), pions, and deuterons. However, we needed to define the particle identification cuts in a systematic way for the analysis program.

After the calibration was done, we defined one set of polygon cuts for identification of particles in the 2-D plot. Figure 4.5 and 4.6 and shows polygon cuts as dashed line
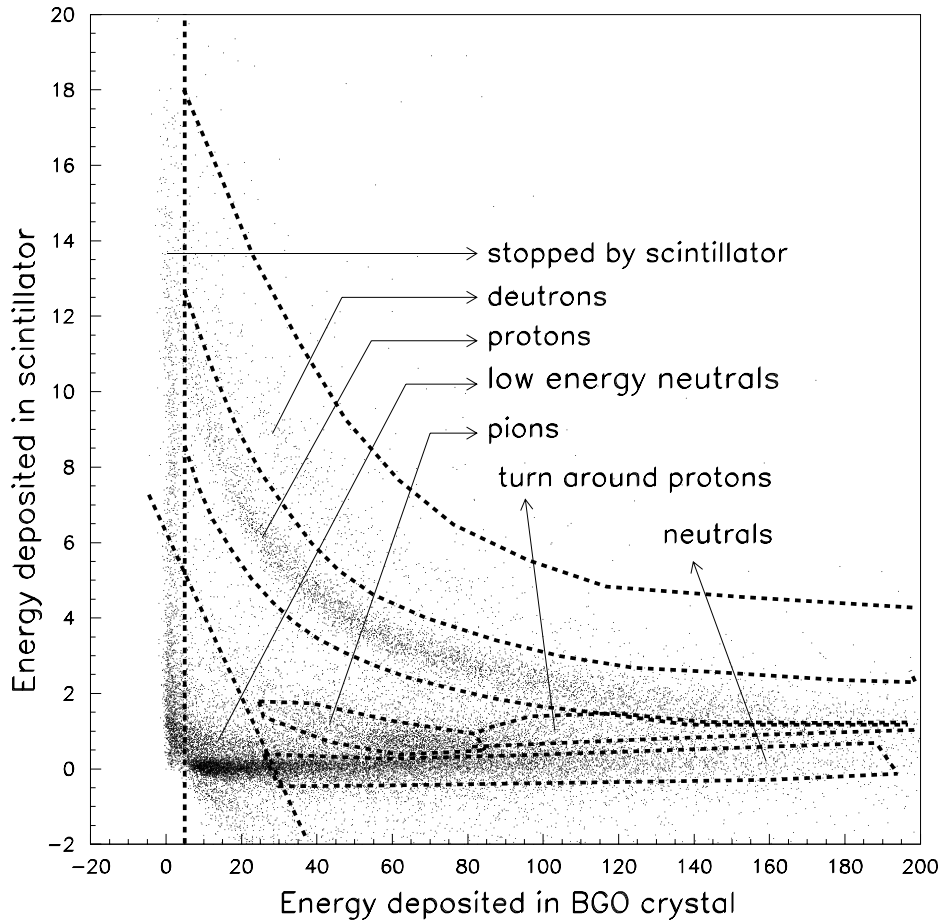
Figure 4.5: Dashed lines represents the separation boundary used for the particle identification for all BGO detectors and for all the runs. The events are taken from the Δ region.

superimposed on a small sample of events in the Δ-region. Only one set of cuts was needed because all of the 2-D plots for all the BGO detectors and all of the runs were
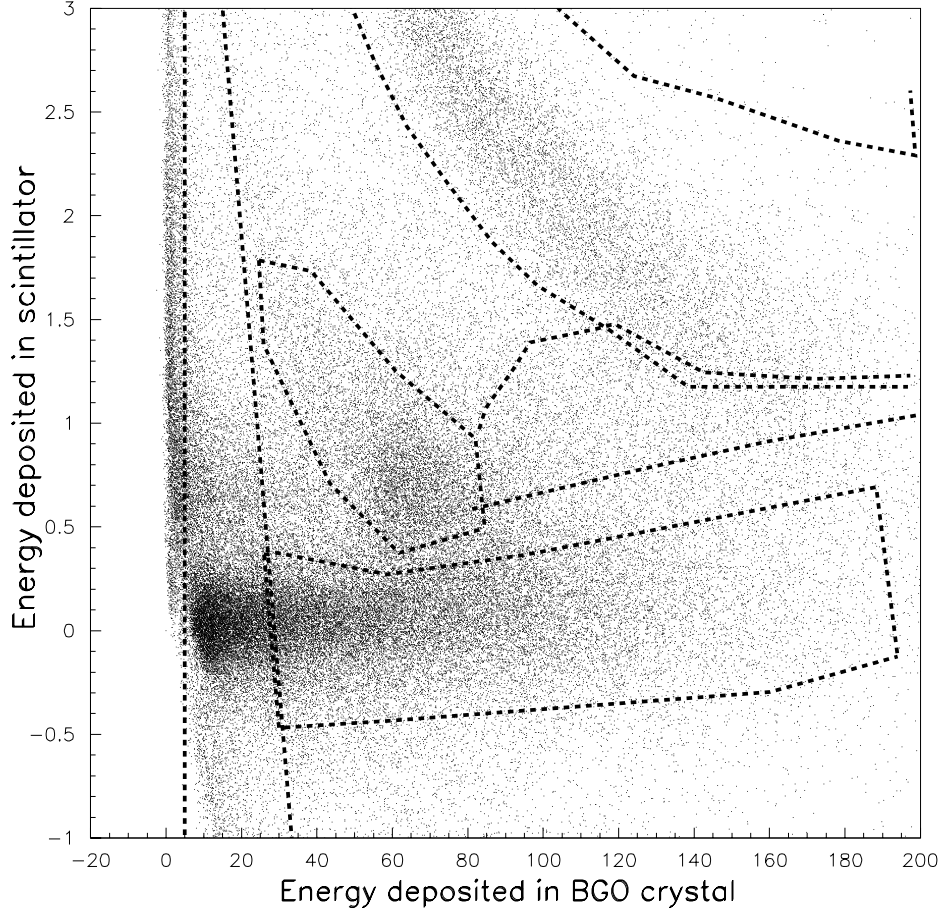
Figure 4.6: This figure is similar to Figure 4.5 but shows the events of neutrals, pions and turn around protons in greater detail.

standardized by "unfolding" and the calibration procedure. Nevertheless, the polygon cuts were checked to insure that they were good for the runs and for all the BGO detectors.

There were two polygon cuts for the protons. The first cut was for the protons with energy less than 185 MeV, where the energy resolution is 2–3% [33]. This proton line is a curve which falls from left to right, as seen in the Figure 4.5, with increasing energy (the deuteron line is similar). The other cut is for protons which had an energy greater than 185 MeV. Those protons are not stopped in the BGO crystal and therefore deposited less of their kinetic energy with increasing incident energy, and are referred to as "turn-around" protons. We used the values listed in Table 4.4 to estimate the true energy for the turn-around protons from the energy deposited in BGO detector.

Energy deposited	95	100	105	110	115	120	125	130	135
Actual energy	313	293	275	260	248	238	230	222	216
Energy deposited	140	145	150	155	160	165	170	175	180
Actual energy	211	207	203	200	198	195	194	192	191

Table 4.4: Table for converting the energy deposited in the BGO detector to the energy of turn-around protons

The energy resolution for turn-around protons is 10-15% [33]. Some more details for identification of protons in LAMPF BGO ball are given in [34].

The separation between the protons and turn-around protons for the energy range 110–185 MeV in the BGO material was not very good and potentially a source of systematic error due to misidentification. In making the particle identification cuts, much care was taken in this region to seperate the protons with energies less than 185 MeV and the turn-around protons. The turn-around protons with energies above about 300 MeV are close to the pion cut, which could also give rise to a systematic error due to misidentification (see Figure 4.5).

The neutrals are events with no energy deposited in the scintillator. They are separated into two groups: low energy neutrals, which deposit less than 25 MeV, and those which deposit more than 25 MeV. For energies less than 25 MeV the signal is primarily due to Møller electrons. The large statistical variation in their signal sizes makes clean seperation from neutrals impossible. At energies > 25 MeV, Møller electrons will not be misidentified as neutrals, but these should be mainly high energy photons from $\pi^0 \to 2\gamma$ or neutrons.

In our analysis we used both protons and turn-around protons for the evaluation of the ω spectrum for $(e, e'p)$ and $(e, e'2p)$ reactions, as the protons could be identified efficiently. However, in investigating the processes involved in the $(e, e'p)$ reaction, we avoided turn-around protons.

4.3.4 TDC Cuts for BGO Detector and Veto Magnets

After the energy calibration, TDC cuts were made for all BGO detectors in each run. Typical TDC plots for a small sample of the data for four BGO detectors are shown in Figure 4.7. Not many accidentals were seen, as the TDC cuts were fairly narrow and enclosed most of the events. The accidental coincidence rates for BGO detector # 4 was expected to be higher than others because it was along the direction of $\vec{q}$.

The TDC cuts of veto magnets were similarly determined for all six magnets in each run. The TDC's were fairly clean. However the TDC's were not recorded from runs in the quasi-elastic region and the TDC for BGO detector #1 was never recorded due to hardware problems.
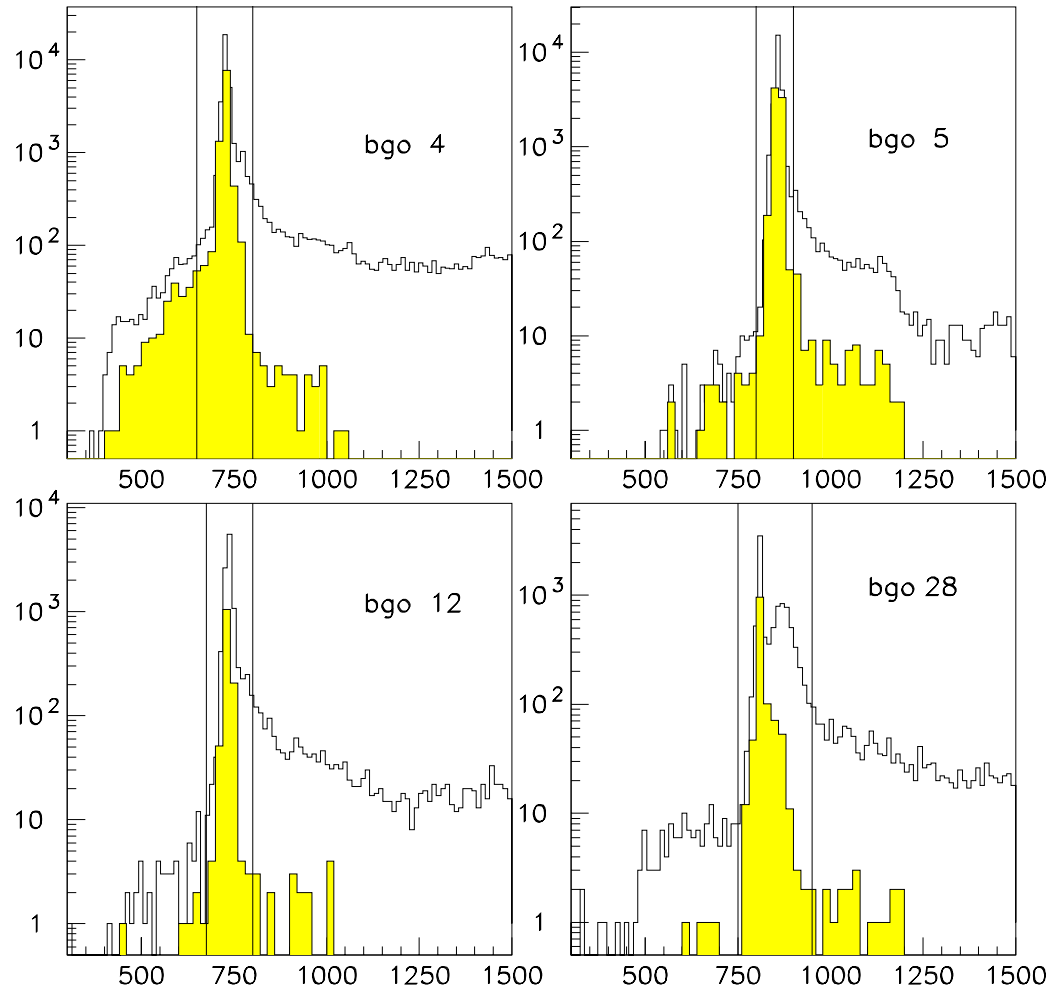
Figure 4.7: The TDCs of four BGO detectors are shown for the any particles detected by the detector in coincidence with electrons detected in the spectrometer (events which passed the Čherenkov cuts). The lines enclosing the peaks are the TDC cuts. The events in grey are from protons only.

Chapter 5

Details of Simulation Programs

The data of our experiment are significantly biased in the determination of total proton yields due to the limited phase space of the BGO ball detector. The acceptance is reduced due to the permanent magnets, removal of two BGO detectors, and displacing the three forward angle BGO detectors as shown in the Figure 5.1. Therefore, to correctly interpret the data, we simulated the geometry of BGO ball detectors including the magnets and beam pipe. Simple physical models were chosen to generate the events. The simulation program helped in understanding the bias due to the geometry and limited energy acceptance of the BGO ball detectors.

The simulation program consisted of two parts: (i) building geometry of the detectors and (ii) event generators to simulate events based on some physical processes. In the following sections, we describe the GEANT program in some detail which incorporated the geometry of the detectors. Some of my experiences with GEANT program is given in Appendix D which may help a novice to understand some structure behind the complex program. Later we describe the event generators which were used.

5.1 The GEANT Program

The program GEANT, written at CERN, is a powerful simulation tool for studying the response of the detector system to various particles. The software can incorporate complex detectors and complex physical processes. The other CERN libraries are integrated with GEANT so that the information on the geometry of the detectors, tracks of the simulated particles, or the simulated events can be stored in the form of ntuples which can be "visualized" by the same package used for analyzing the data.
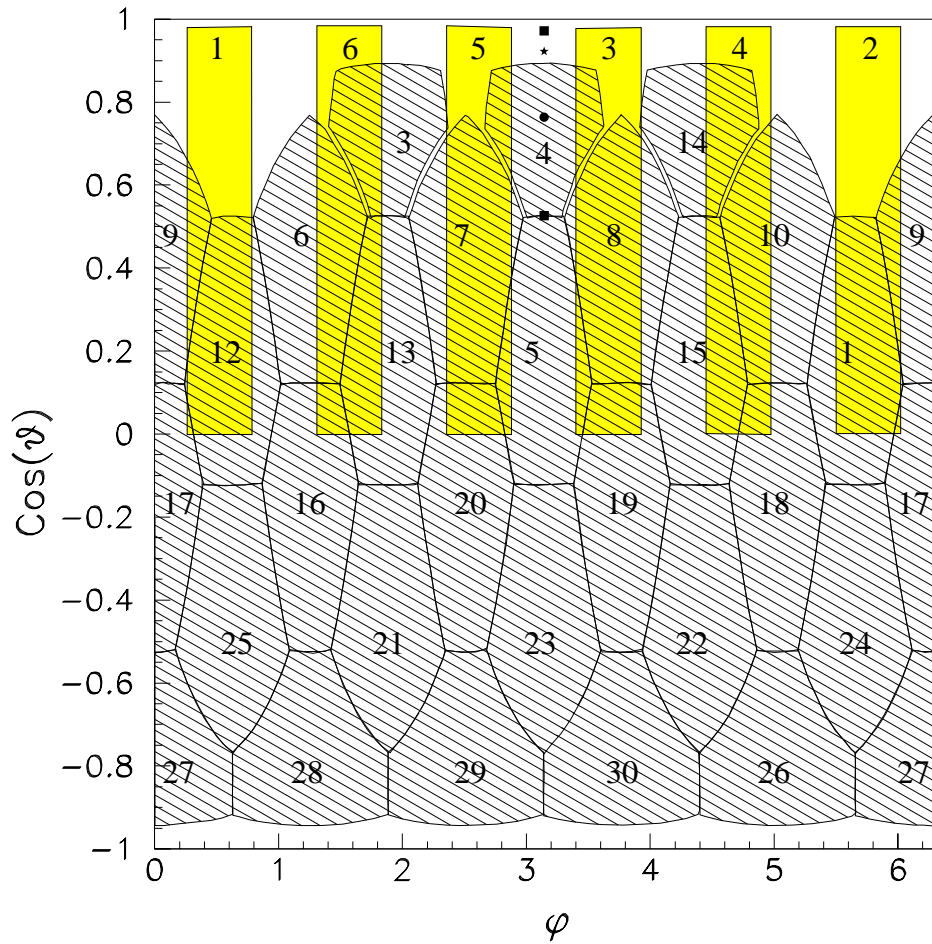
Figure 5.1: The figure shows the phase space of the BGO ball detectors with magnets. The BGO detectors are shaded obliquely. The long rectangular shaded area on the upper part of the figure is due to the magnets. The figure also shows the direction of $\vec{q}$ for various regions: (i) The quasi-elastic region is shown with a black circle at the boundary of two BGO detectors (ii) The dip region by the black square in the BGO detector (iii) The delta region by the Black star, and (iv) The highest energy as the black square above the star. The numbers in the plot are the identification labels of the BGO detectors and the magnets.

After much effort, we set up the correct geometry of the BGO ball with the array of permanent magnets correctly placed on the beam pipe. Figure 2.9 and 2.10 illustrate the complete geometry of our experiment which includes the BGO detectors, permanent magnets on the beam pipe, and rectangular collimator of the spectrometer, shown as a grey rectangle. The two forward BGO detectors are removed for scattered electrons to be detected by the spectrometer. Also visible are the three forward angle BGO detectors displaced slightly to reduce the background rates in those detectors.

In interactive GEANT mode the geometry of the detectors could be moved or rotated to check obvious inconsistencies in the geometry of BGO ball. To make a definite verification of the correct placement of BGO detectors, we make a simulation in GEANT in which protons were produced randomly into the full solid angle. We then plotted the events in $\cos(\theta)$ vs. ϕ for each BGO detector and the magnets and later checked if the events of each BGO detector was placed correctly with respect to the others. In fact Figure 5.1 shows the boundaries for each BGO detector and magnets which were obtained by enclosing the events belonging to each detector or magnet.

For a typical simulation, the GEANT program used the events from a file created by the event generator to create ntuple files. These ntuples contained all the relavent information of the kinematics and detector response which were used for later analysis. The variables in the ntuples are shown in the Table 5.1.

To make the simulation more similar to the data analysis, we plotted the same variables as used in the data analysis, i.e., energy deposited in the scintillator vs. BGO crystal, and imposed a cut in a manner similar to what was used for identification of protons in the data. Figure 5.2 shows the cut enclosing the simulated events which were identified as protons.

In this way, we accounted for protons which were lost because they did not fall in the polygon cuts. The protons which were lost were primarily of two kinds: (i) Some protons which deposited too little energy in the BGO crystal (see Figure 5.2, for instance) by multiple scattering, and fell out of proton cut misses the identification as a proton. (ii) Some protons at higher energy merge with the turn-around protons (protons with energy $> 185 MeV$) and therefore lost due to misidentification by the

For electron	
variables	**comments**
ex,ey,ez	momentum of electron
ee	energy of electron
For first proton	
variables	**comments**
px,py,px	momentum of proton
ke1	kinetic energy of proton
epip1	energy deposited in beam pipe
emag1	energy deposited in magnet
esc1	energy deposited in the scintillator
ebgo1	energy deposited in the BGO crystal
bid1	identification of the BGO detector hit
mid1	identification of magnet hit

Table 5.1: Variables of ntuples containing the information of electron and proton kinematics, and the detector response of protons. These ntuples were created in the typical run by GEANT program. For reactions with two protons, we added similar variables for second proton.

polygon cuts.

Nevertheless, a systematic error may persist because the scintillator and BGO signals had to be seperated for the data but not for the simulations using GEANT. Incorrect separation could displace the position of proton from the proton curve and lead to systematic misidentification.

After taking care of the details of the simulation program, the next step was to augment the information from the event-generator to simulate the events related to the physical processes. The event-generator, ENIGMA was a complex program in itself and could not be directly incorporated into the GEANT program. Therefore large files were generated from the event-generator which contained the momentum and particle identification of the events. The events could be read by GEANT program and ntuples were generated. In the ntuples, we recorded the initial energy and momentum of electrons and protons, energy deposited by the protons in various elements of the detector, such as the beam pipe, magnets, scintillator, and BGO detectors. The information from the ntuples can then be compared to the data in the final analysis.
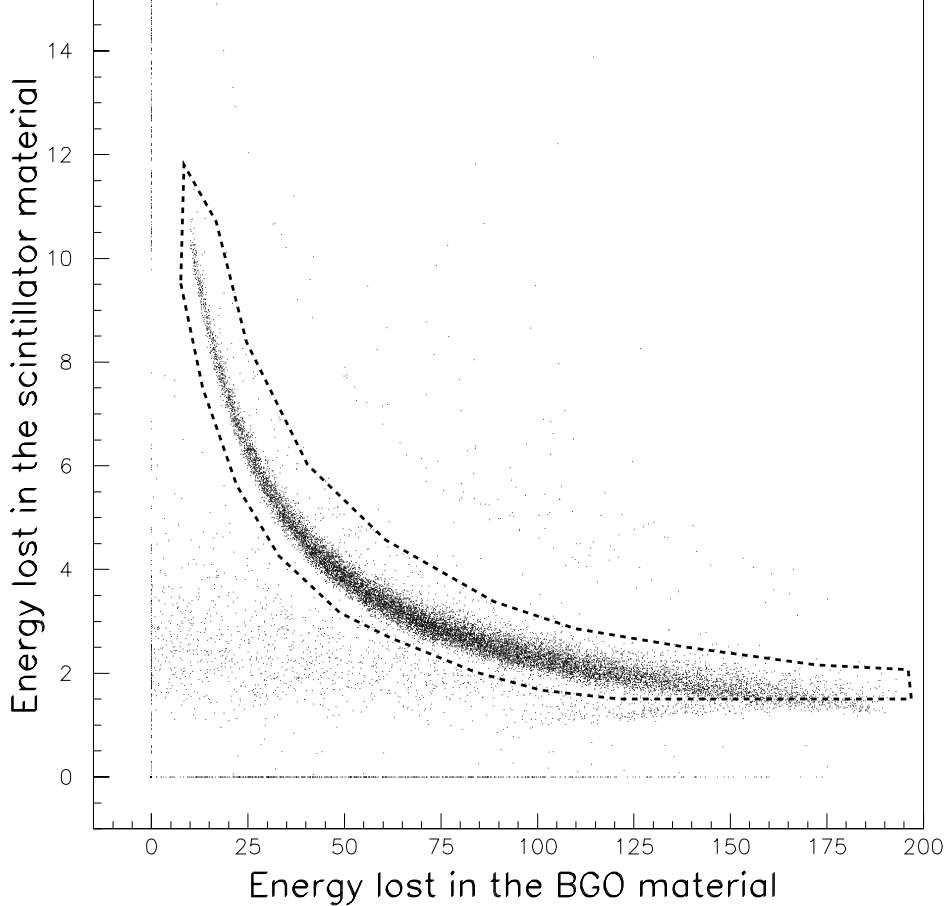
Figure 5.2: All the events in the figure are from protons, the dashed line enclosed the events which were identified as protons.

5.2 Descriptions of the Reaction Mechanisms in ENIGMA

The ENIGMA program, created by Jan Visschers, is an event generator for various electro-magnetic and pion absorption reactions on nuclei. For our experiment, only four reactions were used. They were $(e, e'p)$, $(e, e'pN)$, $(e, e'pNN)$, and $(e, e'p\pi^0)$. We generated events with an electron scattered at about $34.4°$ within the acceptance of the collimator of the electron spectrometer. The protons, neutrons, and pions from the reactions were allowed in any direction. Further details of ENIGMA, including the possible reactions, specification of detectors, and running of the program are given in the Appendix B.

Of the above mentioned reactions, $(e, e'p)$, $(e, e'pN)$, and $(e, e'\ pnn)$ are treated as quasi-elastic reactions. The nucleus with atomic number A is considered to be a pair of

clusters of nucleons such as $(^1\text{H}, \text{A}-1)$, $(^2\text{H}, \text{A}-2)$, and $(^3\text{H}, \text{A}-3)$. The virtual photon from the electron strikes one of the ^1H, ^2H, or ^3H clusters which results in dissociation to give $(e, e'pN)$, $(e, e'pN)$, or $(e, e'\,pnn)$ respectively. The residual nucleus cluster carries the Fermi-momentum prior to collision but otherwise acts as a spectator. The reaction $(e, e'\,p\pi^0)$ is considered as an excitation of a one proton "cluster" into a Δ particle, with absorption of the virtual photon followed by the decay of the Δ to $p\pi^0$.

(a) Quasi Elastic

(b) two-nucleon photo-absorption

(c) three-nucleon photo-absorption

(d) delta excitation
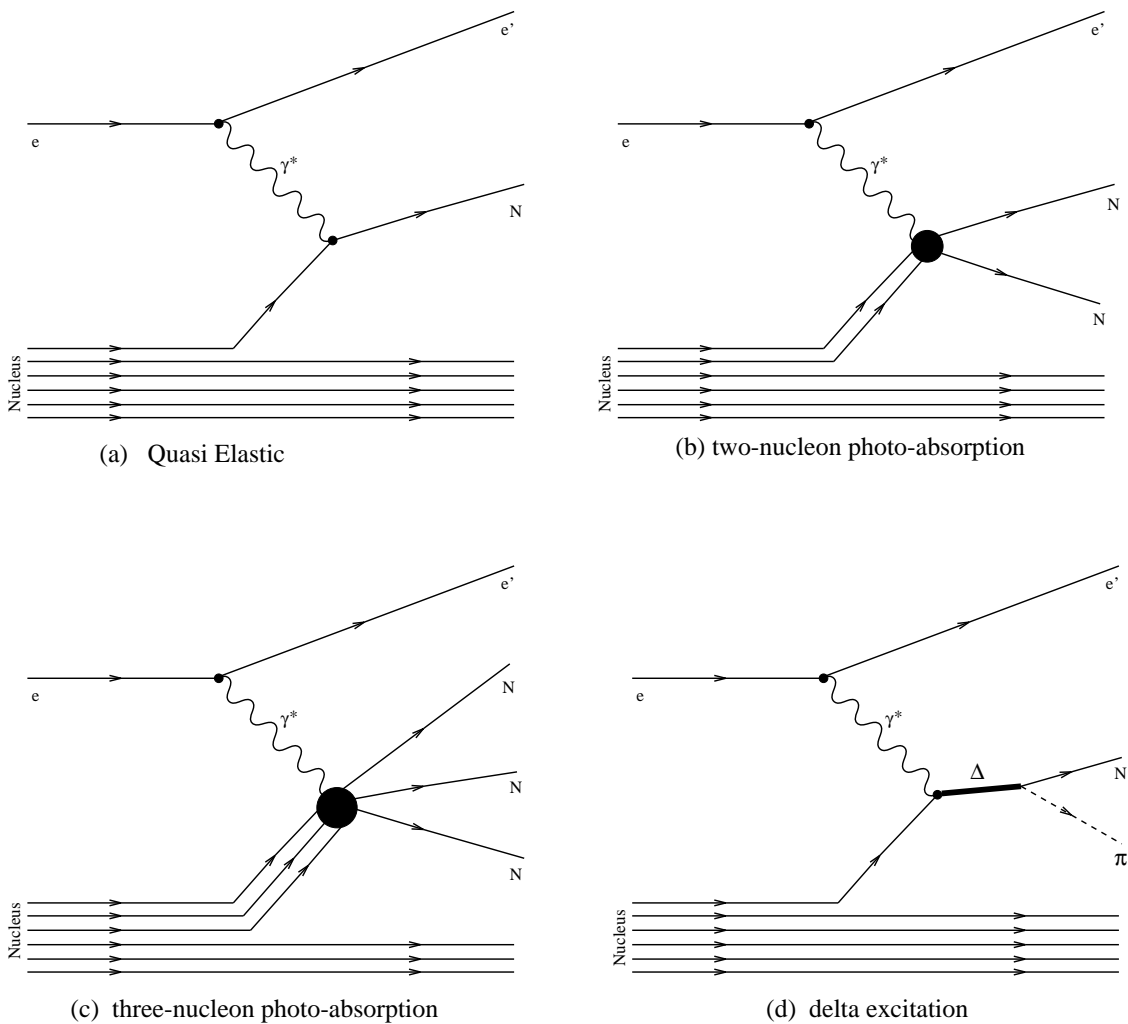
Figure 5.3: Process simulated by ENIGMA

The ^nH cluster with n nucleons is assigned the Fermi momentum based on the single

nucleon harmonic oscillator wave-function as[*] :

$$N(k) = \frac{4\pi k^2 Z}{k_F \sqrt{2\pi}} exp(-nk^2/2k_F^2)$$

Where k is the momentum of the ^{n}H cluster and k_F is the Fermi momentum of a single nucleon which is taken to be $110\,\text{MeV}/\text{c}$ for a medium sized nucleus such as ^{12}C.

---

[*]Since the distribution of single nucleon is Gaussian, the vector sum of n nucleons is also Gaussian with width broadened by a factor of $\sqrt{n}$

Chapter 6

Results

In this chapter we present the results of the $(e, e'p)$ inclusive reaction on a carbon target in the Quasi-Elastic region and Δ region. We shall also compare with some simple models to find the processes which dominate the $(e, e'p)$ reaction. In addition we also present the ω spectra for various process.

I will first discuss the simulation of various reactions and make estimations for proton detection efficiency for the simulated reactions due to the geometry of BGO ball and presence of the magnets. This will help in understanding the results.

The results of this analysis is described in various sections as follows:

- The ω spectra for various reactions are presented in Section 6.4.

- Section 6.5 describes the QE region with fits to kinetic energy of proton with a combination of simulated $(e, e'\ p)$ and $(e, e'\ pn)$ reactions.

- We present the highlight of this thesis in Section 6.6 which gives a detailed analysis of the $(e, e'\ p)$ inclusive reaction in the Δ region and we compare the kinetic energy and angular distributions of the proton with various simulated reactions.

- Section 6.9 describes a similar analysis done in the Δ region, described above, except that analysis is done for energy losses above and below the peak of Δ resonance.

We do not make radiative corrections for any of the data plots, i.e., in the ω spectrum, angular distributions of the proton, or kinetic energy of the proton. It was better to consider the simulated reactions which included the bremsstrahlung effects and therefore our conclusions were not distorted by the radiative effects.

6.1   Brief Outline of Simulations

In the simulation programs, we used the ENIGMA program as an event generator to simulate various reactions. These reactions were $(e, e'p)$, $(e, e'pn)$, $(e, e'pnn)$, $(e, e'p\pi^0)$, $(e, e'ppn)$ and $(e, e'ppnn)$. We chose ENIGMA because of the simplicity and flexibility of the program and the help provided by J. Visschers, the author of the program. Since we do not make radiative corrections in the data, we used ENIGMA with an option which includes bremsstrahlung. Details of ENIGMA and bremsstrahlung are described in Section 5.2, and Appendices B and C. The events generated were used by the GEANT simulation program which takes into account the geometry of the detector and calculates the energy deposited by the proton in various detector elements as it passes through the detectors. The details of the GEANT program are given in Section 5.1 and Appendix D.

We ran the GEANT program and made ntuples that were analyzed later. The variables of the ntuples created by the GEANT program are shown in Table 5.1. The ntuples were created for each of the simulated reactions. These ntuples were then analyzed and various histograms of interest were made for each of the relevant simulated reactions.

In order to study the ω spectrum of the $(e, e'p)$ and $(e, e'pp)$ reactions, we evaluated the efficiency of detecting protons of the simulated reactions to interpret the ω spectra. The details of the proton efficiency determination are given in the next section. For determining the contribution of various processes in the $(e, e'p)$ data, we combined similar histograms of various simulated reactions and matched with the data. The required weight of each of simulated reaction gave the strength of the corresponding reaction.

6.2   Study of Proton Detection Efficiency for Simulated Reactions

The ω-spectra presented in this thesis are not corrected for the acceptance of the geometry and magnets. It is not an easy task to correct for the acceptance as the correction

is strongly model dependent. We do not know the contribution of each modeled process and moreover our models were very simple – essentially phase space distributions. A better way is to study the efficiency of detecting protons due to the geometry and magnets for various simulated reactions. We can then hope that the efficiency study will help understand some aspects of the data.

The protons reaching the BGO detector after passing through the magnets have to pass through about 2.4 cm of iron. The magnets can stop protons with energies of 125–160 MeV, as shown in Figure 6.1, depending on the angle.
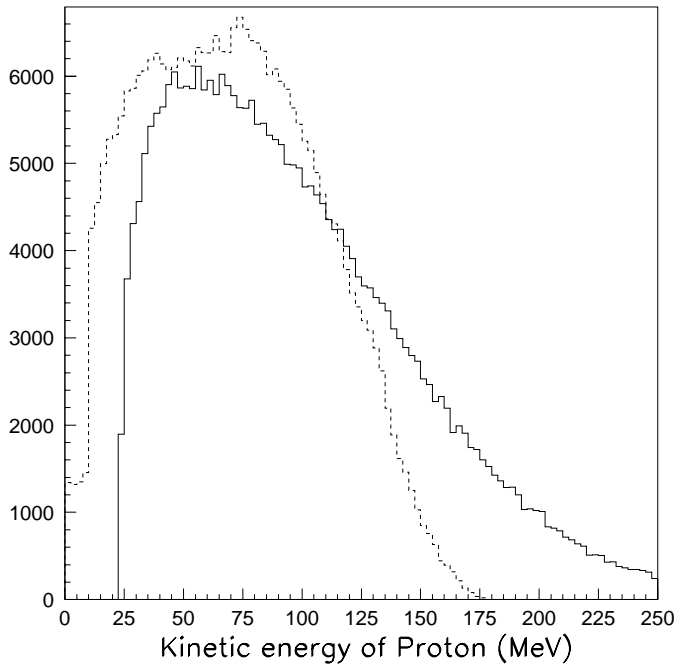
Figure 6.1: The solid line histogram represents the actual kinetic energy distribution of the protons in one simulation. The dashed line shows the energy of those protons lost in the magnets.

One of the main goal of the simulation program was to estimate the acceptance of the BGO ball for the simulated reactions. We define efficiency as,

$$\eta = \frac{\text{number of protons detected in BGO ball}}{\text{number of events in simulation}}$$

The efficiency calculation does not include reaction losses or losses due to the support cans enclosing the BGO detector. These factors are not expected to have strong energy dependence.

This can be applied for two cases: η_{nomag}, where only protons which did not pass through the magnets are counted which is, obtained by removing all events which had veto scintillator signals present, and η_{mag} which includes the protons which passed through the magnets. However, the energy of protons lost in the magnets due to ionization is taken into account. Figures 6.2 and 6.3 show these two detection efficiencies for various simulated reactions.

A detailed look at Figure 6.2 (a) shows that for the $(e, e'\, p)$ reaction the efficiency stays constant for $0 < \omega < 180\,\text{MeV}$ and then starts to decrease. Although $\vec{q}$ is directed into the BGO detector in the QE and dip regions, the efficiency is only 0.54 for $0 < \omega < 180\,\text{MeV}$, indicating that a large fraction of the protons hit the magnets due to the angular spreading from Fermi motion . As ω increases, $\vec{q}$ points closer to the beam direction and finally outside the BGO detectors. The outgoing protons escape detection as the protons are at too small an angle forward angles and the efficiency of detection decreases steadily. A similar steady decrease in efficiency can be seen for the $(e, e'\, p\pi^0)$ reaction at higher ω shown in Figure 6.2 (d). Here also, the proton carries most of the momentum about the direction of $\vec{q}$ owing to the low mass of the pion compared to the proton. The figure indicates that the maximum detection efficiency for the $(e, e'\, p\pi^0)$ is about half that of the $(e, e'\, p)$ reaction because of pion production which causes the protons to be less focussed along $\vec{q}$ and more likely to hit the magnets.

Figure 6.3 is similar to Figure 6.2 except that the protons are allowed to hit the magnets and be detected by BGO ball. The efficiency in both the figures is the same for $0 < \omega < 160\,\text{MeV}$ because the protons do not have sufficient energy to penetrate the magnets and be detected. For $\omega > 160$, Figure 6.3(a) shows an initial sharp rise because the protons can pass through the magnet, but with increasing ω the direction of $\vec{q}$ becomes a larger factor resulting in a steady decline in efficiency.

Another interesting observation is that for the $(e, e'pn)$ and $(e, e'pnn)$ processes, shown in Figure 6.2(b)-(c) and 6.3(b)-(c), the detection efficiency does not decrease for higher ω, unlike for the (e, e') or $(e, e'p\pi^0)$ reactions, but stays fairly constant for $\omega > 300\,\text{MeV}$. It indicates that for two or three nucleon photo-absorption, the distribution of protons is fairly randomized and is not greatly affected by the change in the direction
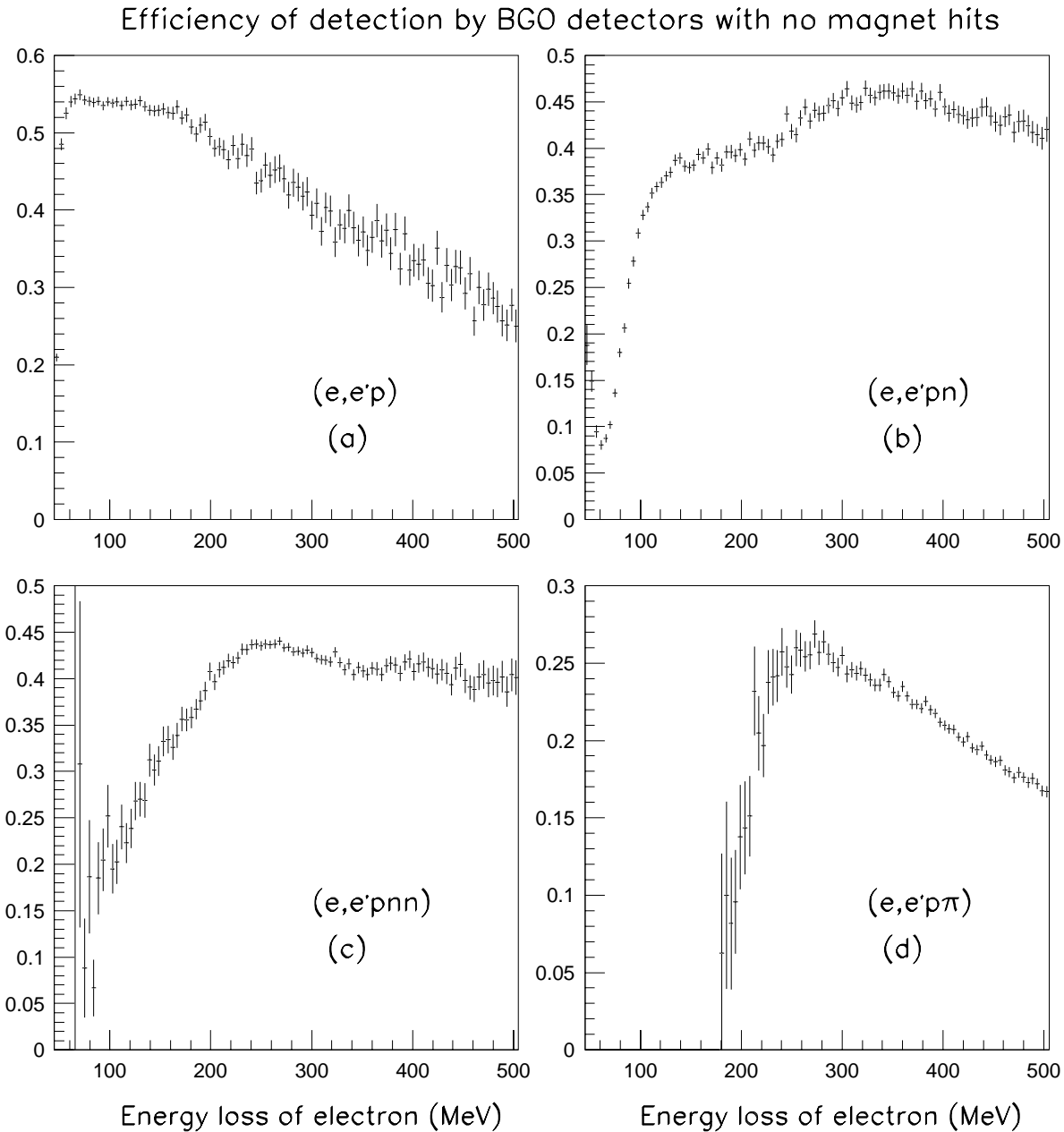
Figure 6.2: Efficiency ($\eta_{\text{no mag}}$) for the detection of protons is plotted as a function of ω for various simulated reactions. A proton is detected if it deposits more than 15 MeV without hitting the magnets.
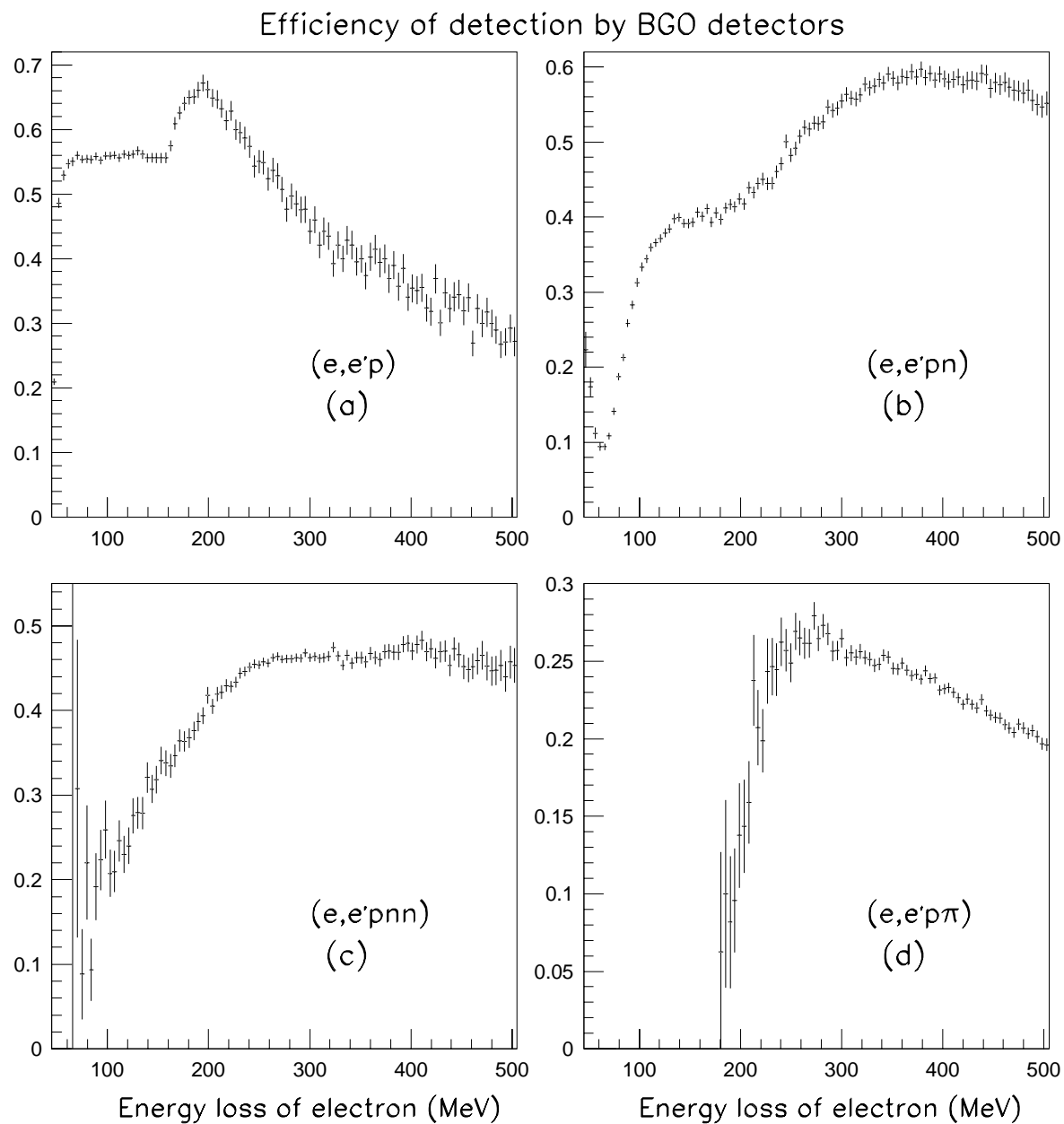
Figure 6.3: These plots differ from Figure 6.2 in that the protons may pass through the magnets (η_{mag}), thereby losing energy, but may be subsequently detected if the protons deposit more than 15 MeV in a BGO detector.
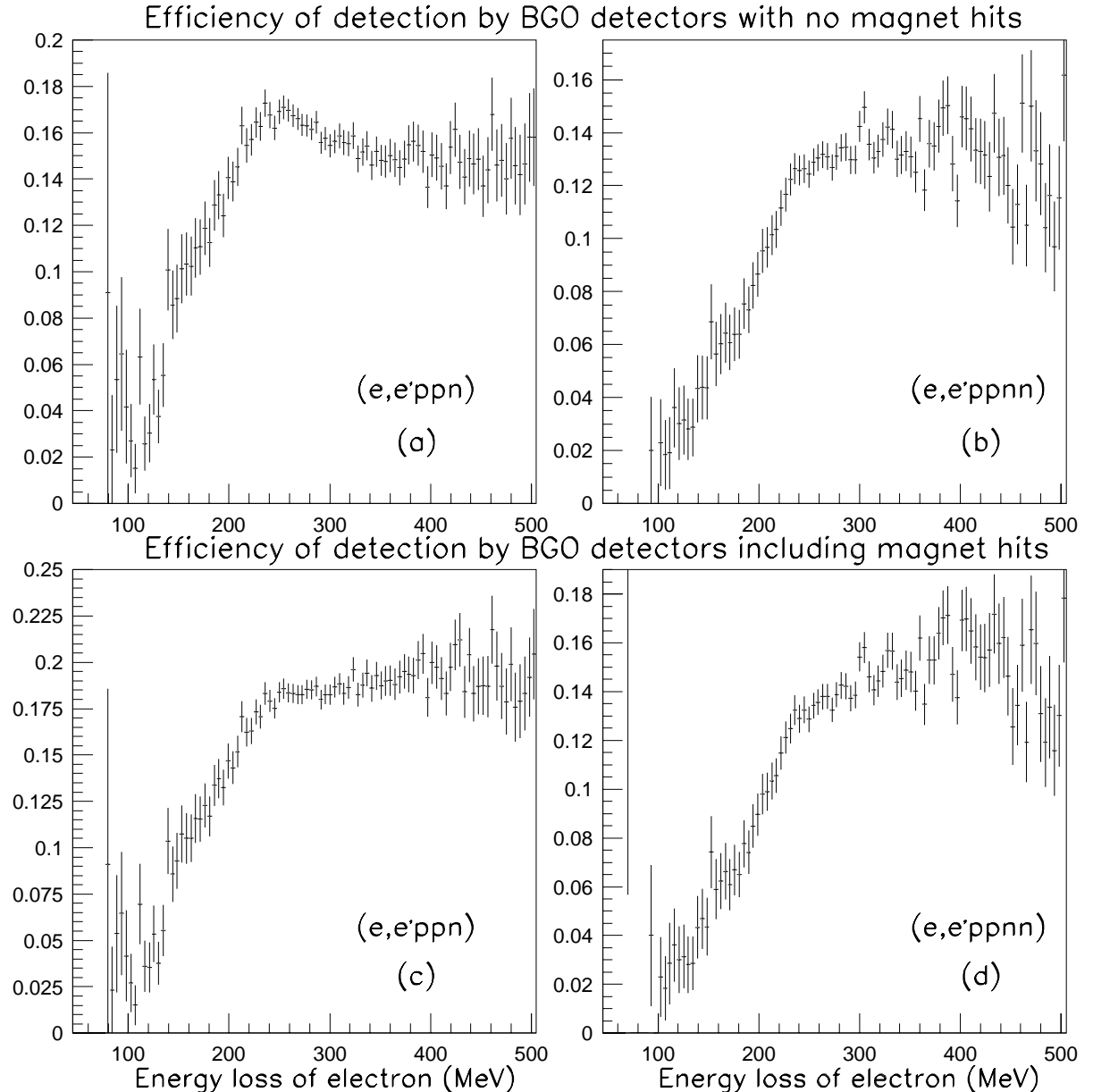
Figure 6.4: The plot of efficiency as a function of ω, of the detection of two protons from the $(e, e'ppn)$ and $(e, e'ppnn)$ reactions. The upper two plots are for the case where no proton hits the magnet. For the lower two plots the protons are allowed to hit the magnets and may be subsequently detected if a proton deposits more than 15 MeV in a BGO detector.

of $\vec{q}$ with increasing ω.

For understanding the $(e, e'pp)$ data, we shall make use of $(e, e'ppn)$ and $(e, e'ppnn)$ simulated reactions. Figure 6.4 also shows that for $\omega > 300\,\text{MeV}$ the efficiency for both reactions is fairly constant.

6.3   Definition of the Regions

Our experiment was done for six different momentum acceptances of the spectrometer. The beam energy was fixed at $705\,\text{MeV}$ and the spectrometer had an angle of $34.4°$ with respect to beam. Since the beam energy and the angle of the spectrometer were unchanged for the entire experiment, the values of ω and $\vec{q}$ are determined only by the momentum acceptance chosen for the spectrometer.

The six settings of the momentum acceptance ranged from the QE to the Δ resonance region. The momentum acceptance along with the other interesting variables for each region are in Table 6.1.

region	QE	dip	LoD	ToD	RoD	VRoD
$P_{e'}$	660–540	519.2–424.8	433.84–354.96	356.4–291.6	297–243	246.4–201.6
$\langle P_{e'} \rangle$	600	472	394.4	324	270	224
ω	45–165	185.8–280.2	271.16–350.04	348.6–413.4	408–462	458.6–503.4
$\langle \omega \rangle$	105	233	310.6	381	435	481
$\langle \vec{q} \rangle$	398.72	413.13	440.15	474.40	505.77	535.35
$\theta_{\langle q \rangle}$	58.23	40.20	30.41	22.70	17.55	13.67
ϵ	0.829	0.781	0.724	0.6494	0.576	0.501
$\hbar/|\langle \vec{q} \rangle|$	.495	.478	.448	.416	.390	.369

Table 6.1: Some interesting variables for the six momentum acceptance settings of the spectrometer. QE, LoD, ToD, RoD, and VROD are the abbreviations of Quasi-Elastic, Left of Δ, Top of Δ, Right of Δ, and Very Right of Δ respectively. The symbols $P_{e'}$, $\langle P_{e'} \rangle$, ω, $\langle \omega \rangle$, $\langle \vec{q} \rangle$, $\theta_{\langle q \rangle}$, ϵ, and $\hbar/|\langle \vec{q} \rangle|$ represent the momentum of scattered electron in the given region, average momentum of the scattered electron, energy loss of electron, average energy loss of the electron, average momentum transfer, angle of the average momentum transfer vector with respect to the beam, longitudinal polarization of the virtual photon, and de Broglie wavelength in the units of MeV/c, MeV, degrees and Fermi respectively.

6.4 Omega Spectrum of Various Cross-Sections

In this section we present some observed cross-sections. These plots will give a qualitative behavior of the strength as a function of ω for various inclusive reactions.

We first show the spectra for various coincidences as a function of the energy loss of the electron, ($E_e - E'_e$ or ω). The beam energy was fixed to $705\,\mathrm{MeV}$, therefore the ω plot needed only the energy of the scattered electron and identification of the particles in the BGO ball in coincidence with scattered electron.

The normalizations were done using the constants provided by Edelhoff [35]. The constants are given in the Table E.1 and the procedure for normalization of the ω plots is described in Appendix E.1.

The upper curve in Figure 6.5 shows the (e, e') inclusive cross-section and the lower curve shows the observed cross-section of $(e, e'X)$, i.e., (e, e') in coincidence with the BGO ball. The upper curve is obtained from events that were triggered only by electrons detected in spectrometer. These events were prescaled by 1:10 except for a few runs where they were not prescaled. The events in $(e, e'X)$ were not prescaled.

The upper curve gives inclusive (e, e') cross-section which is close to the prediction from O'Connell's QFS program shown in Figure C.2 and Figure [?]. The observed $(e, e'X)$ cross-section is only about one-third of the (e, e') cross-section in the QE region. The absolute normalization is slightly higher than O'Connell's curve.

Because of the relatively low ratio of $(e, e'p)/(e, e')$, we were concerned that there was some problem with the coincidence trigger. One way to check this is to compare the accidental coincidence rate with that expected from the singles rate. Most of the coincidence triggers are between cosmic rays and low energy electrons in the BGO scintillator. One expects a coincidence rate of $R_s R_{bgo} \tau$ where R_s is the singles rate in the spectrometer, R_{bgo} the singles rate in the BGO, and τ the coincidence time. The coincidence gate was rather broad, about 70 ns, and the rates could be checked for times for which no true coincidences were expected. The rate was within 10% of the expected value. The raw time spectra also showed a peak in the center of the coincidence time corresponding to the true coincidences. We concluded that there was no indication of
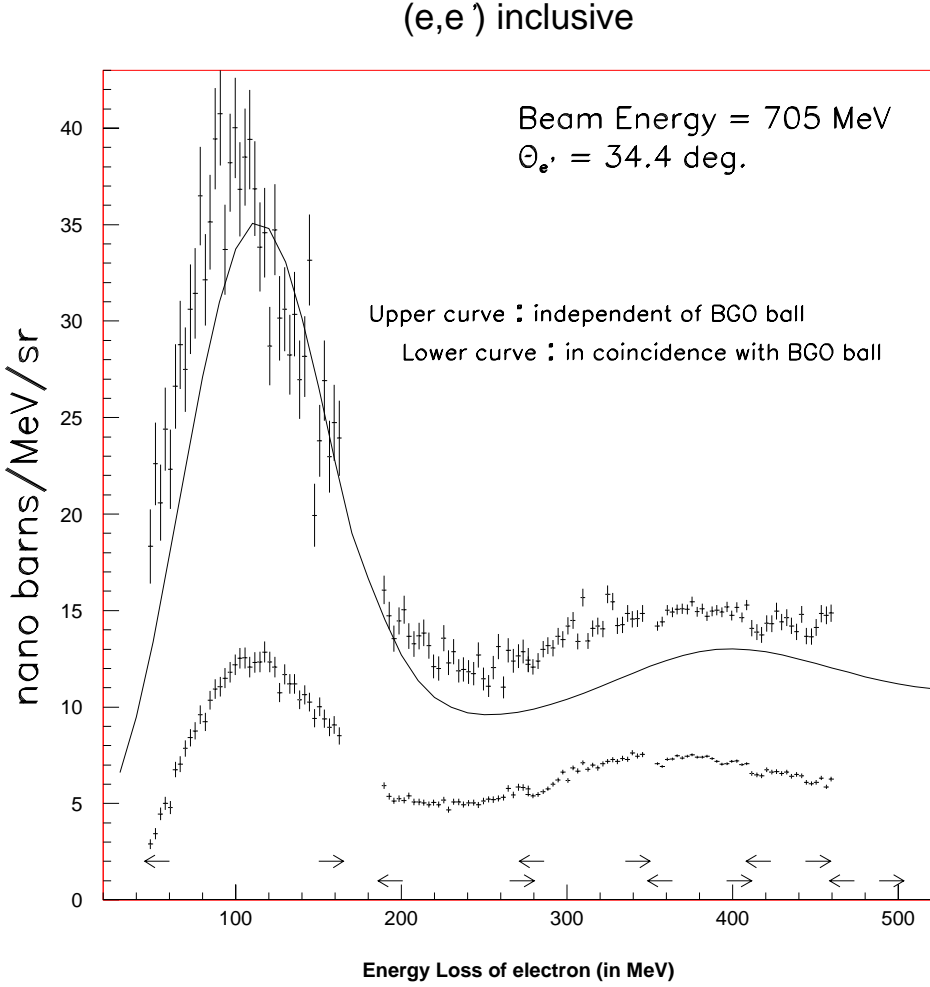
Figure 6.5: (e, e') and $(e, e'X)$ inclusive cross sections from the QE to above the Δ region. The six pairs of $\leftarrow \rightarrow$ arrows show the span of each setting on the spectrometer defining the regions, which are called the QE, dip, LoD, ToD, RoD, and VRoD (also see Table 6.1). The curve is from O'Connell's QFS program.

any significant trigger inefficiency.

Once the off-line particle identification cuts, shown in Figure 4.5, were defined, we obtained yields of various process. The $(e, e'p)$ and $(e, e'pp)$ semi-inclusive observed cross-sections are shown in Figure 6.6 and Figure 6.7.

In determining these yields, we included turn-around protons (see Figure 4.5). This means that protons with energies from 15 to 400 MeV were included. Also included are protons which were able to reach the BGO detectors after passing through the magnets. However the observed cross-sections are not corrected for the geometry. We did not correct for geometry because the efficiency as suggested by Figure 6.3 is very

model dependent for the choice of the simulated reactions. Therefore, the observed cross-sections can be fully interpreted only by considering the efficiency plots described in Section 6.2.

ω Spectrum For $(e, e'p)$
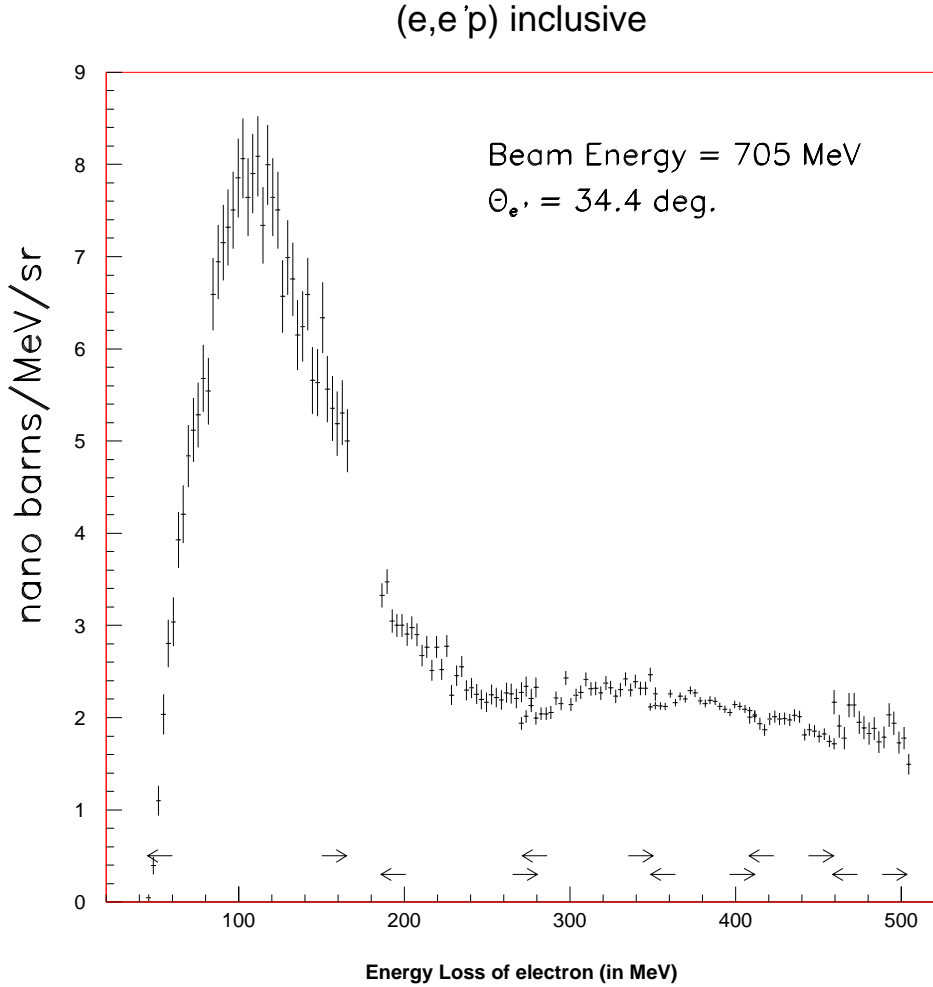
Figure 6.6: $(e, e'p)$ semi-inclusive cross-section

In the $(e, e'p)$ omega spectrum shown in Figure 6.6, we were interested in looking for the shift of peak in Δ region. Unfortunately, the Δ resonant is not very prominent and the normalization constants were not good enough to make that determination. The data in the ω spectrum between the six different regions are not smooth. The spectrum shows small discontinuities between the regions as determined by the boundary of the different momentum acceptance setting of the spectrometer. The discontinuities are

due to the systematic errors from inaccurate determination of beam currents which leads to imprecise evaluation of the normalization constants. The detectors measuring the beam currents were not sensitive to the low beam currents of $\sim 30\,\text{nA}$ which we used.

ω Spectrum For $(e, e'pp)$
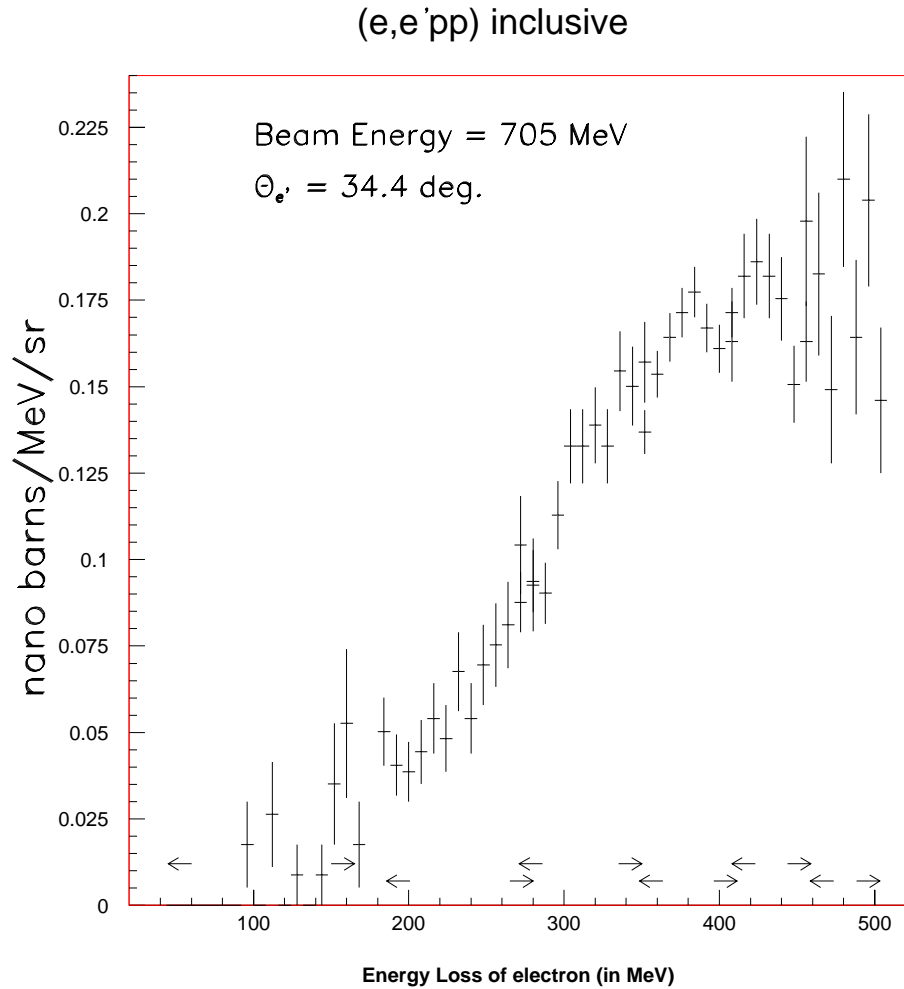
Figure 6.7: $(e, e'2p)$ semi-inclusive cross-section

The $(e, e'pp)$ reaction shown in Figure 6.7 is interesting as it exhibits a non-resonant behavior. The plot shows a steady rise in yields up to the Δ region and then roughly stays constant, although above the Δ resonance the statistical errors are large.

In order to check if the shape of the spectrum is biased due to the detectors or magnets, we determined the reaction which fits best to the kinetic energy spectra of

the protons, as shown in Figure 6.8.

$$349 < \omega < 413 \text{ MeV}$$
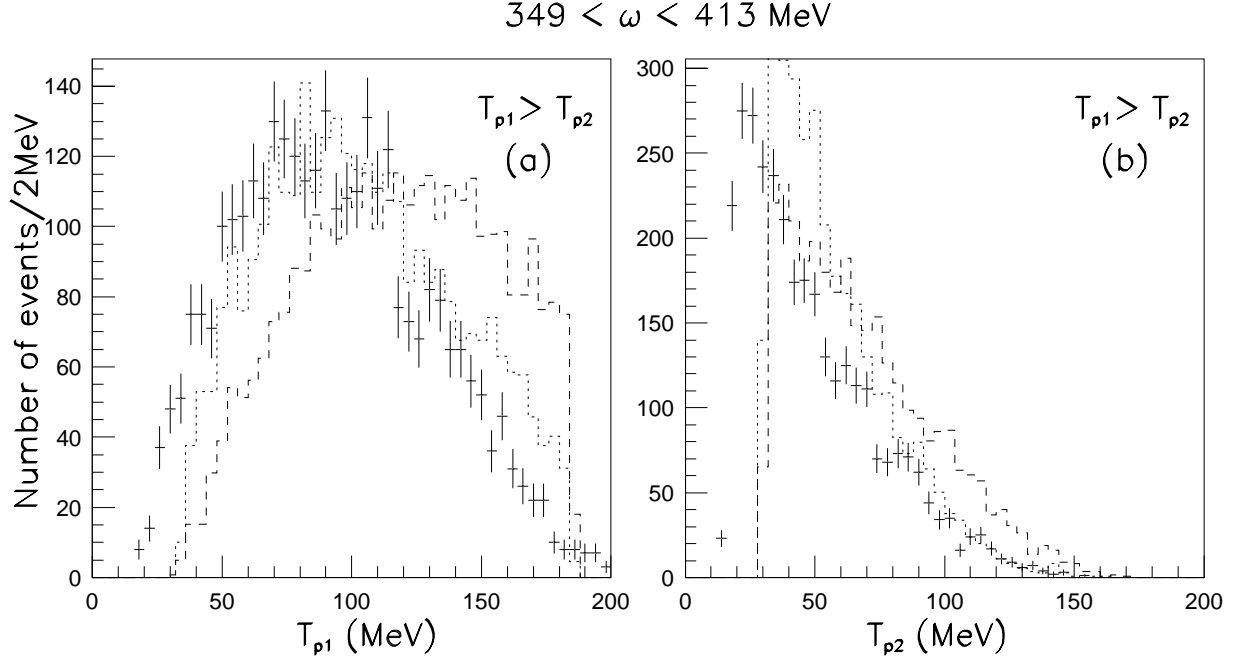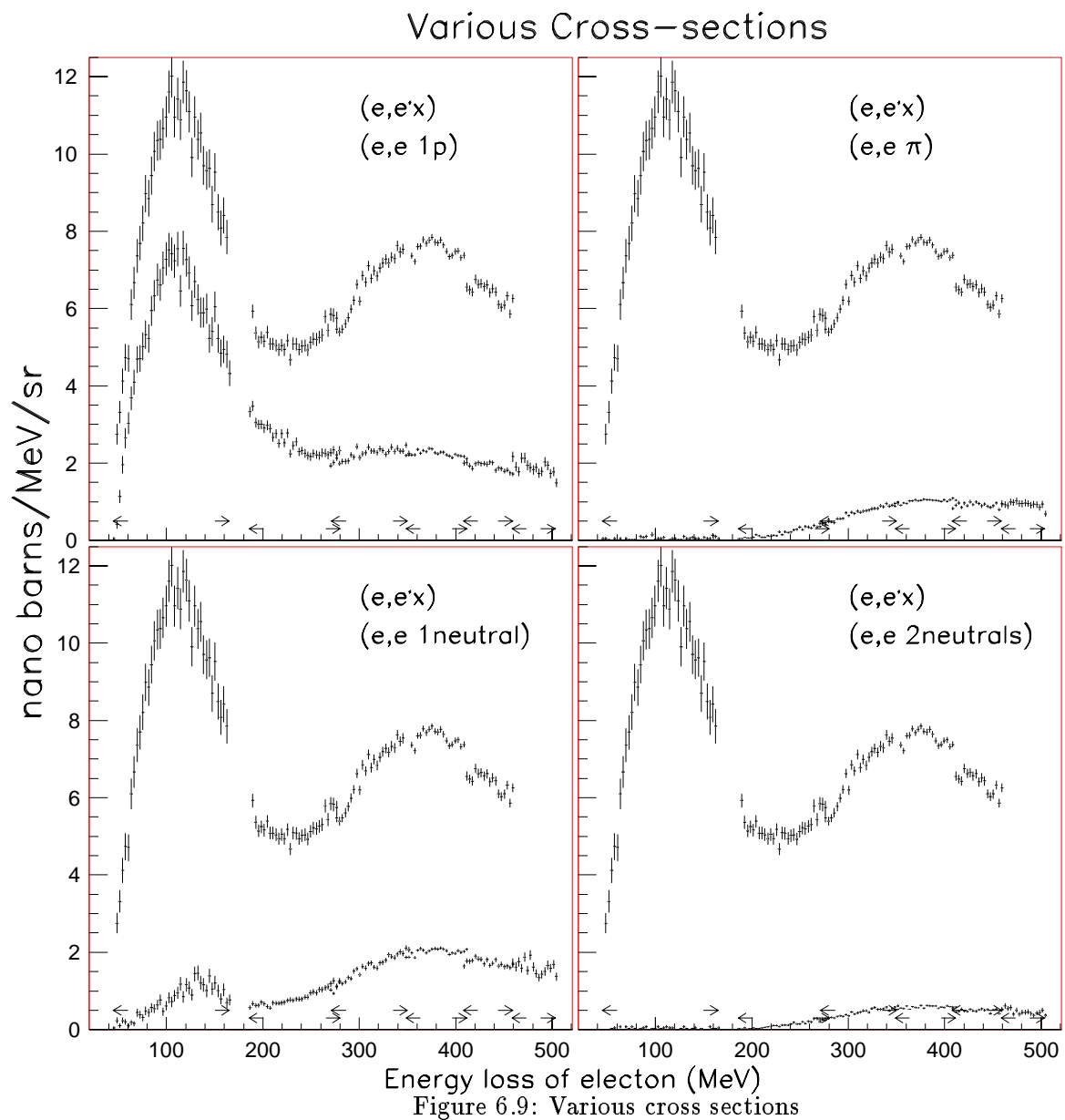
Figure 6.8: The kinetic energy of higher and lower energy protons are shown in (a) and (b) respectively. Each spectrum is fitted with the $(e, e'ppn)$ and $(e, e'ppnn)$ reactions shown respectively as dashed and dotted line.

The figure shows the energy spectra for the higher and the lower energy proton. Among the simulated reactions which were available, the kinetic energy spectrum is best fit by the $(e, e'ppnn)$ reaction. We now refer to the efficiency plots for detecting two protons, assuming that only the reactions $(e, e'ppn)$ and $(e, e'ppnn)$ contribute to the cross-section. Figure 6.4 shows that the efficiency for both reactions stays roughly the same for $\omega > 300 \text{ MeV}$. Therefore, the overall shape of the cross-section should not change in the Δ region, as expected because in three or four nucleon emission the protons have a wide angular spread and therefore the ω spectrum is insensitive to the placement of the magnets or the geometry. We find no evidence of direct two-nucleon decay without FSI which would give higher energy protons. The energy distribution is best determined by $(e, e'ppnn)$.

Figure 6.9: Various cross sections

ω Spectrum For Other Reactions

Lastly, we show in Figure 6.9 the ω specta for various coincidences. The plots are shown with the spectrum for $(e, e'\text{X})$. The lower curve in each plot shows the observed cross-sections of the semi-inclusive $(e, e'p)$, $(e, e'\pi^{\pm})$, $(e, e'1\,\text{neutral})$, and $(e, e'2\,\text{neutrals})$ reactions.

The $(e, e'p)$ reaction was discussed above. For the ω spectrum of $(e, e'1\,\text{neutral})$, the neutrals could be from the high energy photons or neutrons. While the BGO detector is nearly 100% efficient in detecting gamma rays, the neutrons can be detected only with a maximum of about 20% efficiency.

In the reaction $(e, e'2\,\text{neutrals})$, the two neutrals are likely to be from $\pi^0 \rightarrow 2\gamma$ because of detection efficiencies of high energy photons is much greater than that for neutrons.

6.5   Quasi-Elastic Region

In this region 97% of the protons were detected in BGO detectors #4 and #5. It is not surprising because we expect the scattered proton to be roughly along the direction of $\vec{q}$, which lies in between those two detectors (see Figure 5.1). Since only 3% of the protons are detected in the other 26 BGO detectors, the θ_{pq} spectrum will not provide much information. Therefore, we shall use only the T_p spectrum to estimate the strength of various processes contributing to the spectrum.

For inclusive $(e, e'p)$ data in Quasi-Elastic region, we expect the main contribution to be from $(e, e'\,p)$ and $(e, e'\,pn)$ reactions. Therefore, it will be illuminating to compare the exclusive $(e, e'\,p)$ and $(e, e'\,pn)$ reaction with the data. Figure 6.10 a-b shows the simulation of $(e, e'\,p)$ and $(e, e'\,pn)$ individually superimposed with the data. We normalized the plots by imposing the condition that the area of the simulated events is equal to the data between 25 and 140 MeV.

The Figure 6.10 shows that the data can largely be explained by the $(e, e'\,p)$ exclusive reaction. However, the exclusive $(e, e'\,p)$ reaction has less strength at the lower end of T_p spectrum and overestimates the number of protons at higher energies.
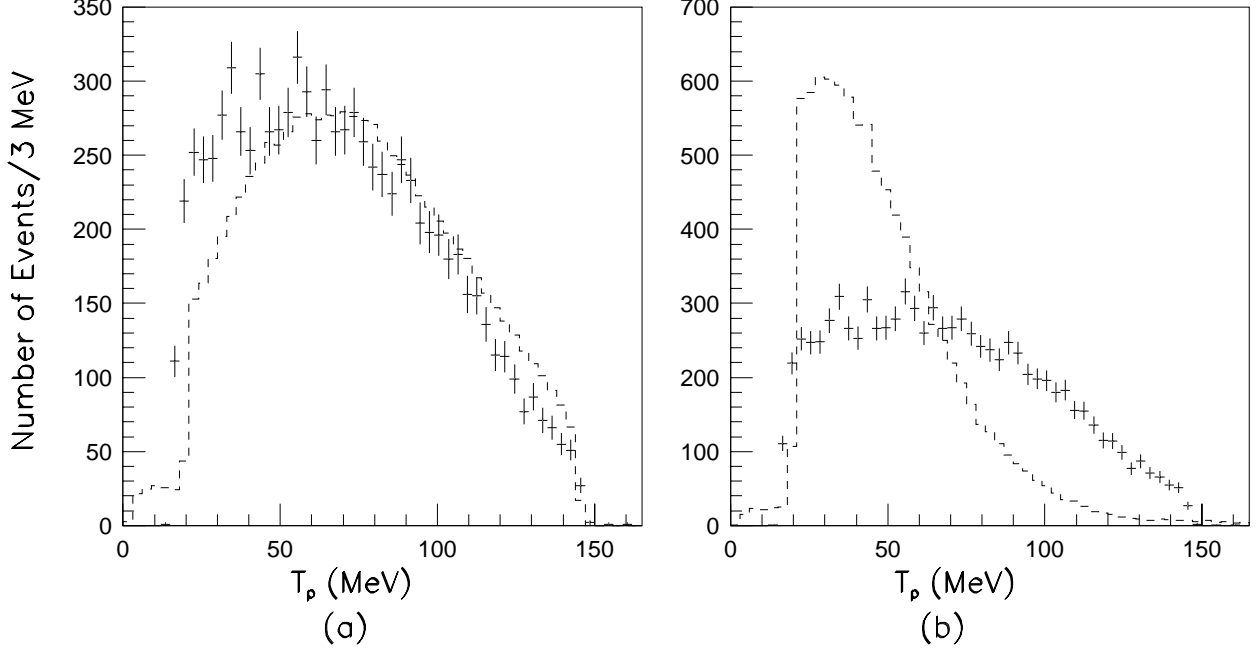
Figure 6.10: The kinetic energy of protons, T_p in QE region is plotted and the dashed line is from the simulation of $(e, e'\, p)$ and $(e, e'\, pn)$ processes in (a) and (b) respectively

On the contrary, the exclusive $(e, e'\, pn)$ reaction has opposite features – more protons in the lower energy and few protons at higher energy. It is therefore reasonable to try the combination of $(e, e'\, p)$ and $(e, e'\, pn)$ to fit the T_p spectrum. As shown in Figure 6.11, We find that 80% of $(e, e'\, p)$ and 20% of $(e, e'\, pn)$ gives a good fit with minimum chi-square of 206 with 36 degrees of freedom in the the T_p spectrum between 25 and 140 MeV. Here $(e, e'\, pn)$ reaction is only the two-body absorption and we did not consider two nucleon emission due to the FSI. Another process $(e, e'\, p\pi^0)$, is not considered because it is energetically not possible to create pions in QE region ($\omega <$ m_{π^0}). We also do not involve the $(e, e'\, pnn)$ process because dissociating three nucleons requires more energy and is less likely compared to the reactions we did considered. Moreover, the $(e, e'\, p)$ and $(e, e'\, pn)$ process are sufficient to explain the data.

6.6   Delta Region

In this region, we expect that the angular and energy distribution of protons in the
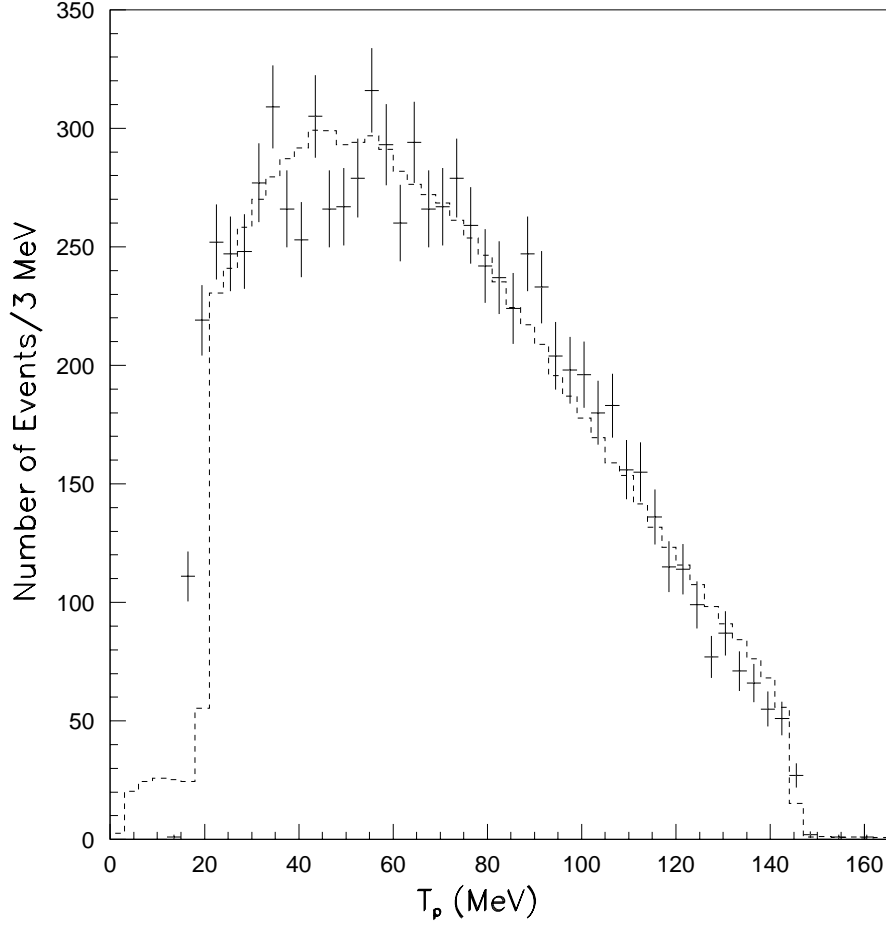
Figure 6.11: The spectrum of kinetic energy of protons, T_p is fit with $(e, e'\ p)$ and $(e, e'\ pn)$ process in QE region by the dashed line

inclusive $(e, e'\ p)$ reaction to be primarily due to the $(e, e'p\pi)$, $(e, e'pn)$, and $(e, e'pnn)$ processes. We neglect the exclusive $(e, e'\ p)$ reaction because in the delta region enough energy is available to excite the protons to a Δ^+ which decays to $p\pi^0$ (or neutrons to $\Delta^0 \rightarrow p\pi^-$. In fact, the $(e, e'\ p\pi^0)$ reaction is actually a photo-production of pion from quasi-free proton via delta excitation. The other reactions we mentioned are the two- and three- body absorption which may come from the Δ decay to a $p\pi^0$ followed by pion absorption by other nucleons or the Δ decaying through $\Delta N \rightarrow NN$ or via some more complicated process. Other reactions like $(e, e'p\pi N)$ or $(e, e'p\pi\pi)$ or four nucleon dissociation can also contribute. However, their contribution should not be significant as many-hadron interactions tend to be less favorable. It will be our objective to determine the strengths of various processes contributing in the delta

region by studying the scattered protons and comparing with simulated processes.

In our experiment, we observed a significant amount of high energy protons in the BGO detectors at large angles with respect to $\vec{q}$. It is an interesting observation as it indicates that reactions other than $(e, e'p\pi)$ are present. Since pions are much lighter than protons, we expect the proton to carry much of the momentum in the pion production process and therefore expect the outgoing protons to have a smaller θ_{pq}. This fact is illustrated in Figure 6.12 where the angular distributions of simulated high energy protons from various processes are plotted. The plots in θ_{pq} are shown for the protons having kinetic energy between 80 and 110 MeV and are integrated over ϕ_{pq}. The plots show that for $\theta_{pq} > 60°$, there is not much contribution from the $(e, e'\, p\pi^0)$ process. Another interesting observation for $80 < T_p < 110$ MeV is that even in the $(e, e'\, pn)$ and $(e, e'\, pnn)$ processes the θ_{pq} distribution is markedly different. The peak for $(e, e'\, pnn)$ process lies at about $\theta_{pq} \sim 55 - 60°$ whereas $(e, e'\, pn)$ peaks at about $90°$. We can use these differences for isolating these reactions. The observations for $80 < T_p < 110$ MeV and $\theta_{pq} > 60°$ can be stated as follows:

- There is negligible contribution from $(e, e'\, p\pi^0)$ process. Therefore two- and three-body process are the process to be considered in this region.

- The $(e, e'\, pnn)$ still has about 54% of the strength, however the strength decreases with increasing θ_{pq}.

- The $(e, e'\, pn)$ reaction has 83% of the strength in this region, with the peak strength at about $90°$.

The substantial strength for large θ_{pq} in two-body process can be partly understood by the fact that in the ENIGMA program the two-nucleon cluster dissociates with an angle of $180°$ between two-nucleons in the center-of-mass frame of the virtual photon and two-body cluster. The Lorentz transformation back to the reference frame of the laboratory still gives a large angle.

6.6.1 T_p Plot for $\theta_{pq} > 60°$

It is therefore reasonable, as a first step, to study the special case when $\theta_{pq} > 60°$ and model the data based on only two- and three-body mechanisms and ignore the pion photoproduction process as it is kinematically suppressed for $\theta_{pq} > 60°$.

Among the plots giving the angular distribution and kinetic energy of protons, we firstly attempt to fit the plot of kinetic energy of proton (T_p) by combination of two- and three-body process. Figure 6.13 shows the kinetic energy spectra of protons in the range of 20–180 MeV. The data (vertical bars) are fit by pure $(e, e'\ pn)$ (long-dashed) and $(e, e'\ pnn)$ (short-dashed) lines with a similar condition imposed on the simulated events. It is surprising to see that only the three-body process alone is sufficient to give a good fit to the data between 60–180 MeV, which contains 80% of the events shown in the plot. A two-body process clearly fails to fit within that range of the energy spectrum.

The large domination of the three-body absorption is in itself an unexpected result. Therefore, to progress our analysis further, it is reasonable to assume that only the $(e, e'pnn)$ reaction is involved for outgoing protons in the energy range 60–180 MeV for $\theta_{pq} > 60°$. The three-body absorption, however, fails to fit for $T_p < 60$ MeV, which may indicate that other reactions like four-body absorption, final state interactions, or $(e, e'p\pi N)$ contributing to the low energy spectrum of the outgoing protons.

6.6.2 θ_{pq} Plot for $80 < T_p < 110$ Mev

We now plot the angular distribution of the proton as shown in Figure 6.14 for $\theta_{pq} > 60°$ with the energy range $80 < T_p < 110$ MeV. We choose this range with the expectation that it will distinguish between the two- and three-body processes, as explained earlier in association with Figure 6.12. In the plot the data points are shown as bullets ($\bullet$), the hollow squares and hollow circles ($\circ$) are from the simulation of $(e, e'\ pn)$ and $(e, e'\ pnn)$ respectively. Each data point represents the events registered by single BGO detector. In some cases there are two data points and simulation points at same θ_{pq} because there are two BGO detectors with different ϕ_{pq} but with same θ_{pq}.

The asymmetry in the data points for same θ_{pq} with different ϕ_{pq} may be present because the virtual photon exchanged is polarized as indicated by equation 1.5. However the non smooth ϕ_{pq} dependence is most likely due to a systematic error in rejection of the protons passing through the magnets.

Beside the two data points between 100–105°, indicated by two arrows near the data points, we get a reasonable fit with the three-body process. The two-body process fits just as well for $\theta_{pq} > 90°$ but clearly separates for lower θ_{pq}. This gives additional confirmation that only three-body process are involved for high energy protons (80–110 MeV) which are scattered at large angles ($\theta_{pq} > 60°$). The two erroneous data points are likely due to the failure to veto protons passing through the magnets. It will be further discussed in Section 6.7.

The θ_{pq} plot is very interesting for several reasons. Unlike the T_p spectrum, it has no bias from geometrical acceptance of our experiment. The plot is therefore presented in terms of cross-section, which can be modeled in the future or used as a reference without the consideration of our experimental setup. The details of the calculation for conversion of events/bin plot to cross-section is shown in Appendix E. It provides additional confirmation of our assumption that the three-body photo-absorption process is dominant. The plot helps in understanding some of the systematic errors of our experiment which are explained in Section 6.7.

6.6.3 Fitting the T_p and θ_{pq} Plots From All BGO Detectors

So far we have concluded that it is not necessary to consider a two-body process to explain the data in the Δ-region. Hence, we take only the reactions $(e, e'\, pnn)$ and $(e, e'\, p\pi^0)$ into consideration to explain the T_p and θ_{pq} spectra detected by all BGO detectors (at all angles).

We proceed in a manner similar to the case for $\theta_{pq} > 60°$, where we first attempted to fit the T_p spectrum and then check for consistency with the θ_{pq} plot. We fit the T_p spectrum from all BGO detectors using the following prescription.

- We have seen earlier that a pure $(e, e'\, pnn)$ reaction gives a good fit to the

T_p spectrum for $\theta_{pq} > 60°$ (see Figure 6.13). We use this fit to estimate the strength of $(e, e'\ pnn)$ in T_p spectrum from all BGO detectors by assuming that the kinetic energy of protons from the three-body process can be extrapolated for $\theta_{pq} < 60°$. The long-dashed curve in Figure 6.15 shows this estimated strength from three-body process contributing to T_p spectrum from all BGO detectors.

- The rest of the missing T_p spectrum is filled by $(e, e'p\pi)$ as we have discounted other processes like $(e, e'\ pn)$ and $(e, e'p)$. This filling is done by imposing the condition that the total number of events from pion-production and three-body process equals the data events for the energy range $60 < T_p < 180\ \text{MeV}$.

The added spectrum of $(e, e'\ pnn)$ and $(e, e'\ p\pi^0)$ gives a fairly good fit for $T_p > 60\ \text{MeV}$. The fit, consisted of 28% $(e, e'\ p\pi^0)$ and 72% of $(e, e'\ pnn)$ reaction. For the same mixture we plot the angular distribution in Figure 6.16 for the protons within the energy range 60–140 MeV. The fit is reasonably good for $\theta_{pq} > 60°$ but fair for the lower angles.

6.7   Discussion of Possible Systematic Errors in This Experiment

1. In the Quasi-Elastic region, the data points in the lower energy part of the T_p spectrum (see Figure 6.11) do not smoothly vary which affects the confidence in estimating the strength of $(e, e'\ pn)$ reaction. This is because the $(e, e'\ pn)$ reaction primarily fits the lower end of the T_p spectrum.

2. The θ_{pq} plots are in general not very smooth. This indicates some possible errors which could have contributed in our experiment. One of the largest contributions to the systematic error is the inefficient rejection of protons passing through the magnets. In fact, the efficiencies of the veto scintillators were not determined. Also, the veto scintillator # 1 was not working.

   The inefficiencies of veto scintillators causes an overestimation of the cross-section in the θ_{pq} plots as the cross-section calculation depends inversely on the effective solid angle of the BGO detector. We considered the effective solid angle as the

solid angle of the BGO detector not covered by the magnets. In Figure 6.14 the data points near the two arrows shown are most likely due to the inefficiency of the veto scintillator. In that figure the two BGO detectors giving those two erroneous points had a coverage of 63% by the magnets – largest of all the data points in that plot.

3. For the θ_{pq} plots containing the full range of angles, the data points for $\theta_{pq} < 60°$ may have greater systematic errors. This is again due to inefficiencies of the veto scintillators as discussed in the previous paragraph. The veto magnets covered the forward angle BGO detectors (with low θ_{pq}), hence the inefficiencies of the veto scintillator gives higher systematic uncertainity for the data points with $\theta_{pq} < 60°$

4. There could also be a systematic error from the misidentification of large energy protons. The protons with energies $> 110\,\mathrm{MeV}$ and the turn around protons are very close together in the 2-D plot from which the particle identification is made. An imperfect "unfolding" or calibration can result in greater loss of protons due to misidentification for some BGO detectors. As a result, some points could underestimate the cross-section in the θ_{pq} plots.

6.8   Why no $(e, e'pn)$?

Our analysis is based on the study of the overall distribution of protons in kinetic energy and angle. While we can explain our data from $(e, e'\,pnn)$ and $(e, e'\,p\pi^0)$ reactions, some contribution from $(e, e'\,pn)$ cannot be ruled out.

To check if our BGO detectors were insensitive to the $(e, e'\,pn)$ reaction, we look at the 2-D plot of angular distribution vs. kinetic energy of proton for various reactions as shown in the Figure 6.19. The small rectanglular boundary encloses protons for $80 < T_p < 110\,\mathrm{MeV}$ and $\theta_{pq} > 60°$. These events were plotted in Figure 6.14 which gave confidence that three-body absorption was much greater than two-body absorption.

In the three plots, we can see that rectangular boundary does not enclose much of $(e, e'p\pi)$. For large θ_{pq} as expected, for the $(e, e'\,pnn)$ reaction the rectangle encloses a significant area of the phase space. For the $(e, e'\,pn)$ reaction, the events enclosed

are moderately well represented but only for smaller kinetic energies. In the $(e, e'\, pn)$ reaction, the proton energy is much higher for smaller θ_{pq} and in our data analysis we considered only the protons with energy less than $185\,\mathrm{MeV}$. Therefore we were not sensitive to the high energy protons. Instead, we detected the lower energy protons which came at large θ_{pq}. The low energy protons have greater probability for undergoing FSI compared to the higher energy protons further masking the two-nucleon effects.

We now give the most conservative estimate for the contribution of two-body process which can contribute to our data. In Figure 6.18(a), we fit the T_p spectrum for $\theta_{pq} > 60°$ entirely by the two-body process. We see that it fits only near the higher end of the T_p spectrum. Here contribution is about 30% of the T_p spectrum. Figure 6.18(b) shows the T_p spectrum from all the BGO detectors. The strength of the two-body reaction is determined from Figure 6.18(a) and assumes that the extrapolation for the angular distribution of the protons is valid. The contribution of the $(e, e'\, pn)$ process in the plot (b) is about 20% for protons with $20 < T_p < 185\,\mathrm{MeV}$. This does not take into account two-body absorption followed by FSI.

6.9 ω region higher and lower than the Δ peak

Our study so far shows that the $(e, e'\, p)$ spectrum in the QE region can be explained by $(e, e'\, p)$ and $(e, e'\, pn)$ reactions, whereas the Δ region can be explained by $(e, e'\, pnn)$ and $(e, e'\, p\pi^0)$ reactions. It will be therefore interesting to know the strength of these reactions contributing to ω away from the the Δ peak.

We proceed in the manner similar to the analysis done for the Δ region. We make four plots: (i) The kinetic energy of protons for $\theta_{pq} > 60°$, where the contribution from $p\pi$ channel is minimum (ii) θ_{pq} plots for protons with $80 < T_p < 110\,\mathrm{MeV}$ to give consistency with T_p spectrum (iii) T_p plots for all BGO detectors to also include the $(e, e'\, p\pi^0)$ reaction and (iv) θ_{pq} plots for protons with $60 < T_p < 180\,\mathrm{MeV}$ to check for consistency.

The four plots are shown for above and below the Δ peak in Figures 6.20 and 6.21 respectively. The plots have a larger statistical error compared to plots in delta region

due to smaller amount of data.

The procedure for analysis is similar to analysis done in Δ region, hence we will just mention the highlights of the results and avoid the unnecessary details of analysis procedure.

The T_p spectrum of the protons above the Δ region can be fit well with the $(e, e'\, pnn)$ and $(e, e'p\pi)$ reactions. As seen in Figure 6.20(c), the three-body absorption contributes about 83% of the cross section for protons with $60 < T_p < 180\,\mathrm{MeV}$. The contribution is higher by 11% from the delta region. The rest is about 11%, which is from the $(e, e'p\pi)$ reaction.

The region below the delta region differs in that a combination of $(e, e'\, pnn)$ and $(e, e'\, p\pi^0)$ do not give a good fit for the T_p spectrum shown in Figure 6.21(c) as compared to similar plot in the Δ and above the Δ region. Nevertheless, the $(e, e'\, pnn)$ reaction fits well for $T_p > 60$ and $\theta_{pq} > 60°$ in the T_p spectrum shown in Figure 6.21(a) which contributes about 67% in Figure 6.21(c) for $60 < T_p < 180\,\mathrm{MeV}$. This is 5% less than the Δ region.
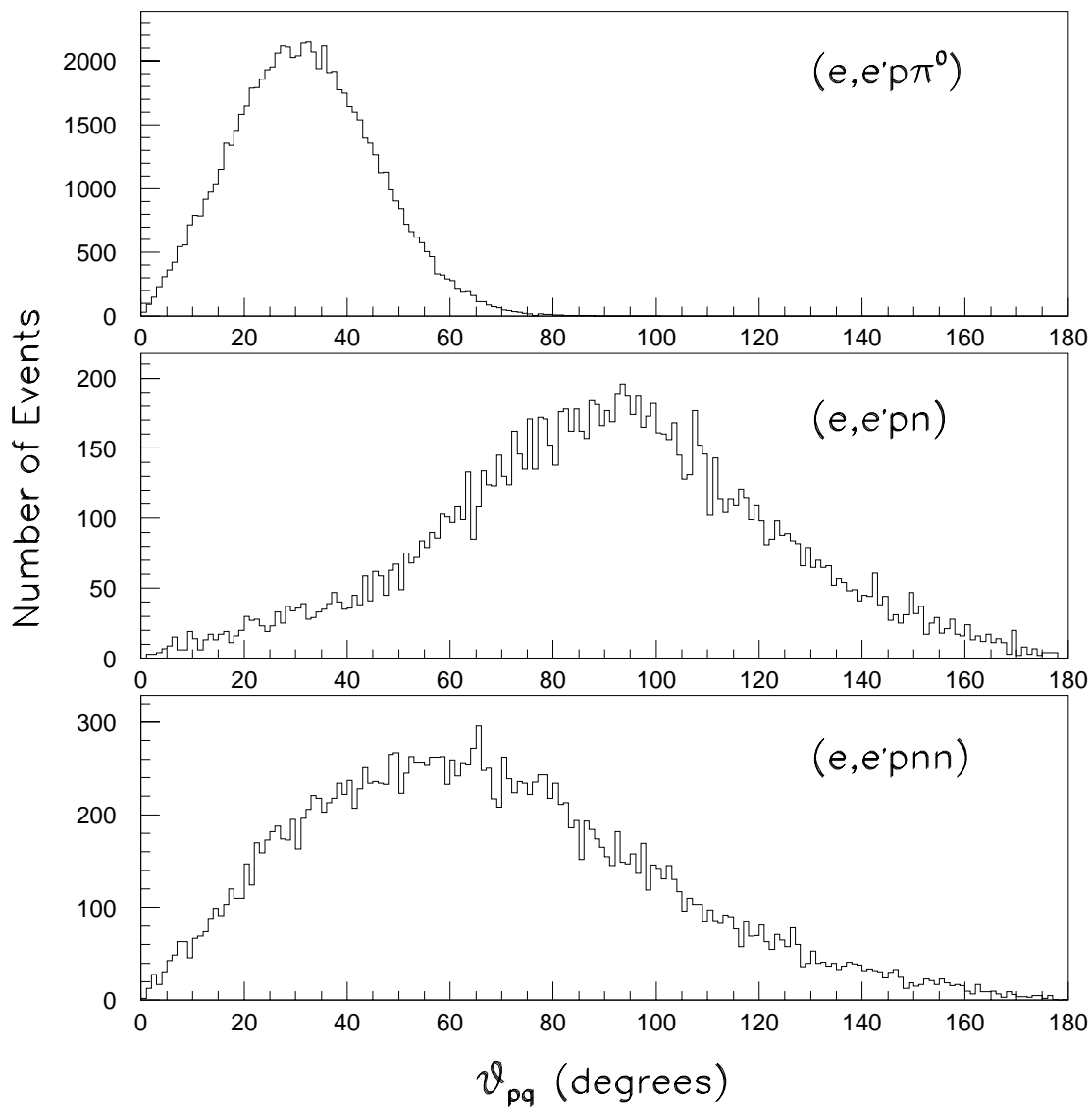
Figure 6.12: Plots with respect to θ_{pq} for various process from the ENIGMA simulation with energy of protons between 80 and 110 MeV. It indicates a possibility for isolating the processes when $\theta_{pq} > 60°$
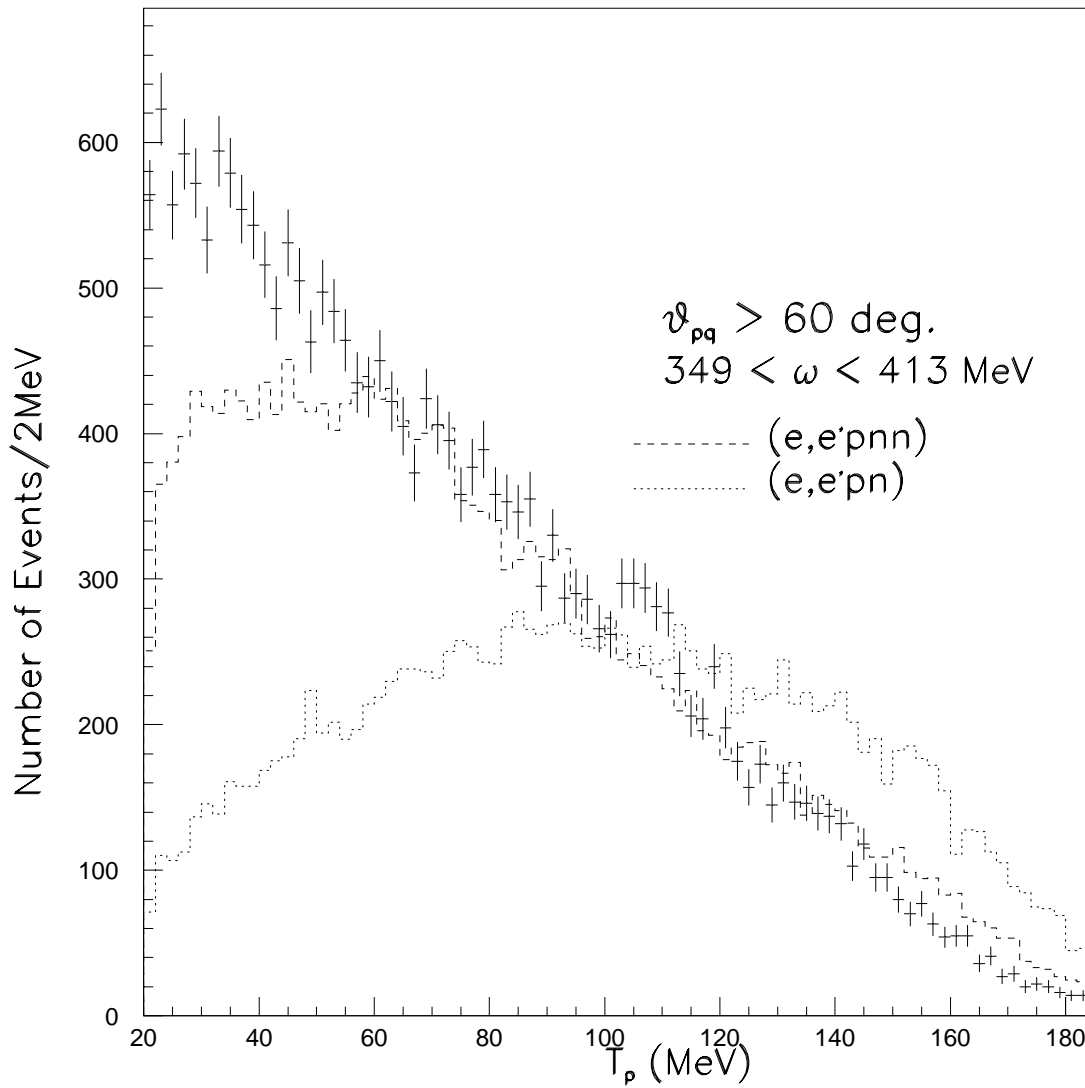
Figure 6.13: Protons scattered at large angles with respect to $\vec{q}$ ($\theta_{pq} > 60°$) are shown in the figure. The dashed line and the dotted line are from the simulated $(e, e'\ pnn)$ and $(e, e'\ pn)$ reactions respectively.
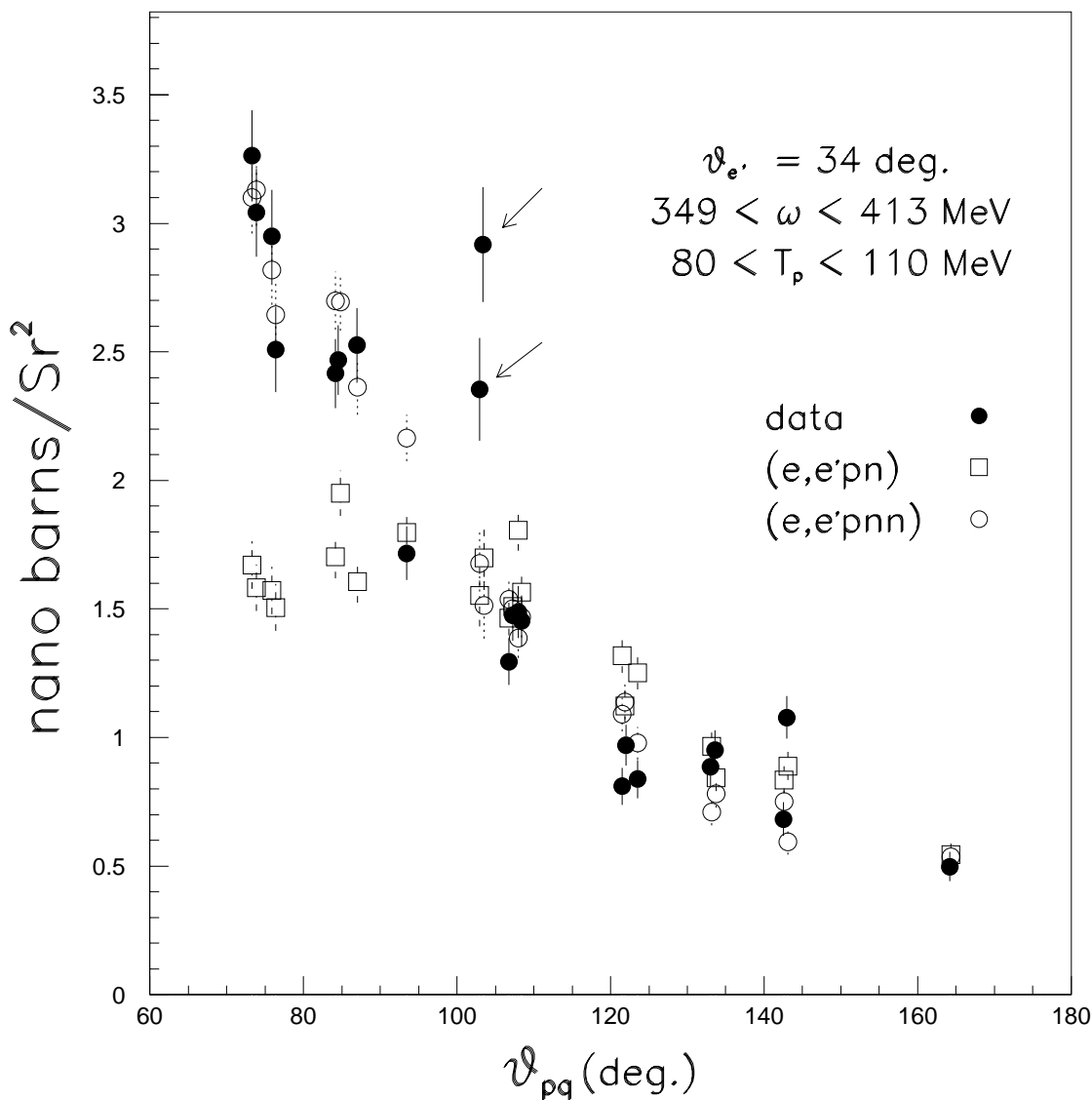
Figure 6.14: Angular distribution for protons scattered at large angles with kinetic energy between 80 to 110 MeV. The data is represented by bullets and the $(e, e'\ pnn)$ and $(e, e'\ pn)$ simulated reactions are given by hollow circles and hollow squares respectively.
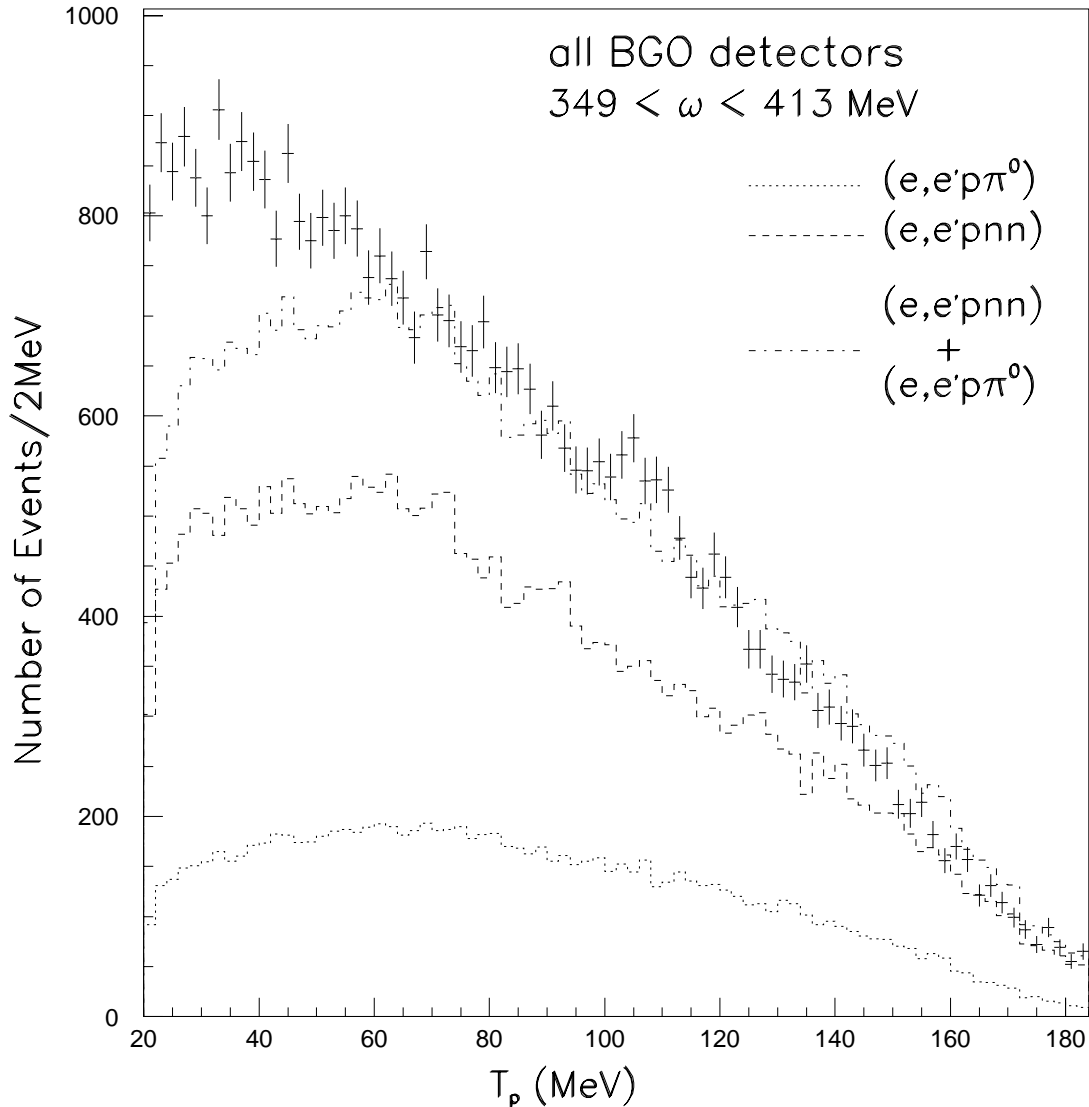
Figure 6.15: Protons from all BGO detectors are plotted. The data is fit by using the previously determined strength of the $(e, e'\ pnn)$ reaction (dashed line) and the $(e, e'\ p\pi^0)$ reaction (dotted line) so that the sum (dotted-dashed line) gives good fit for $T_p > 60\,\text{MeV}$. For $T_p < 60\,\text{MeV}$, the curve from the simulated events explains only 80% of the data.
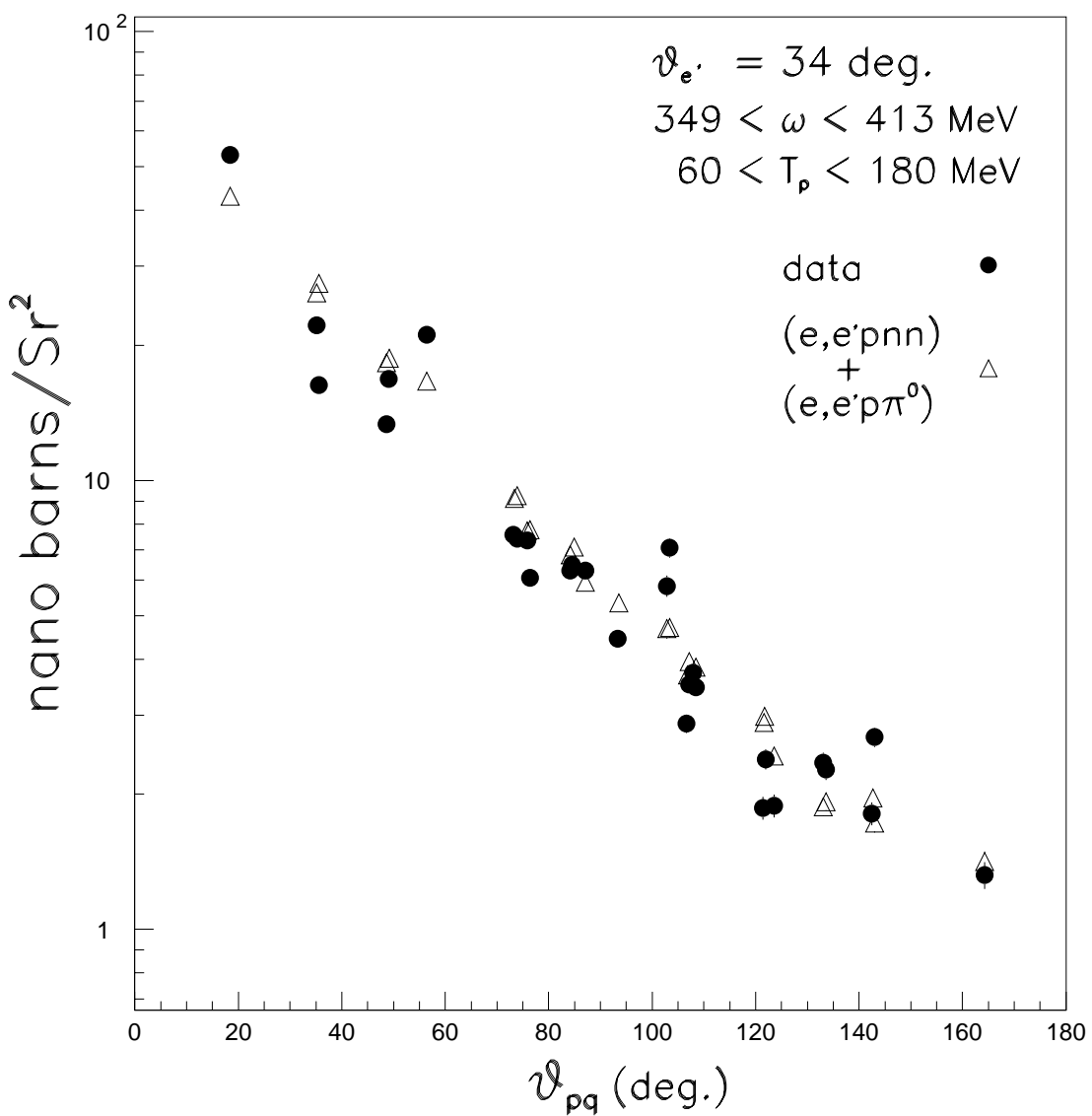
Figure 6.16: Angular distribution of all protons detected is compared with the sum of $(e, e'\, pnn)$ and $(e, e'\, p\pi^0)$ process whose strength was determined by the Figure 6.15.
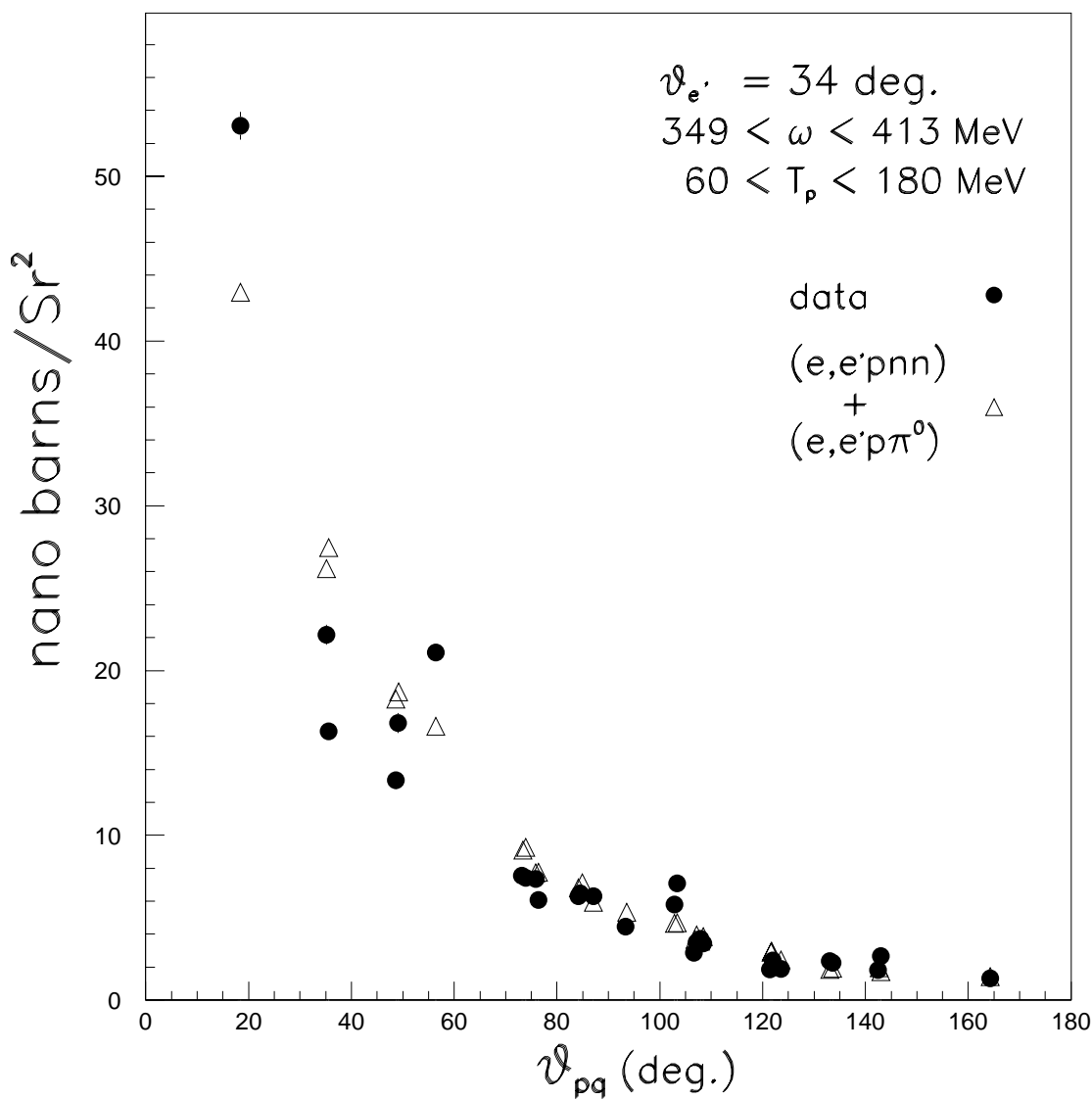
Figure 6.17: Same as Figure 6.16 with a linear scale
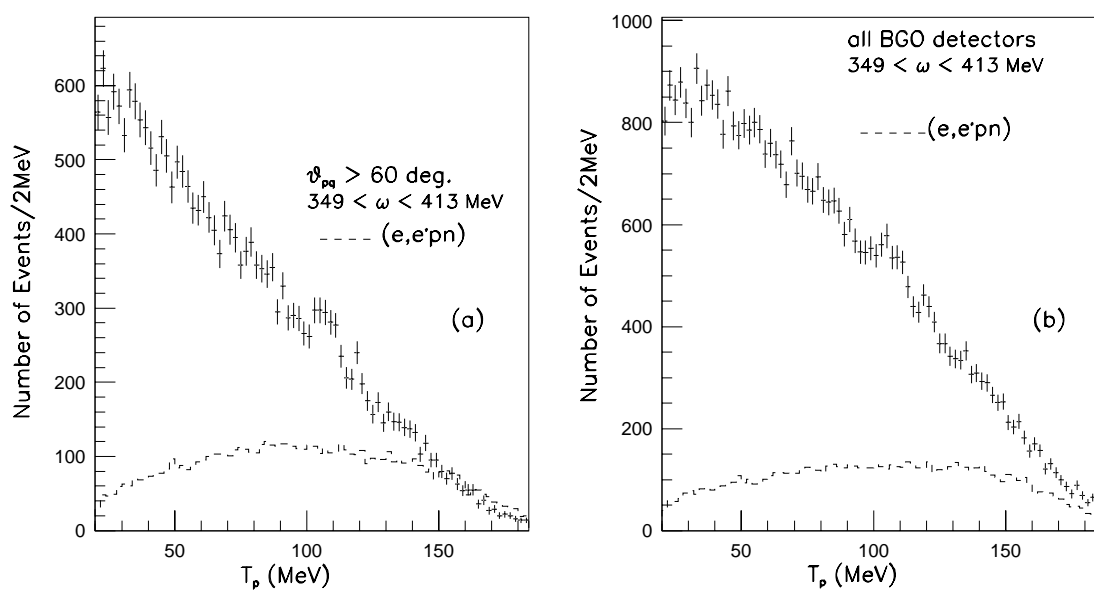
Figure 6.18: Maximal contribution from $(e, e'\, pn)$ reaction: Left figure has 30% of $(e, e'\, pn)$ reaction which contributes to 20% of total reaction on the right
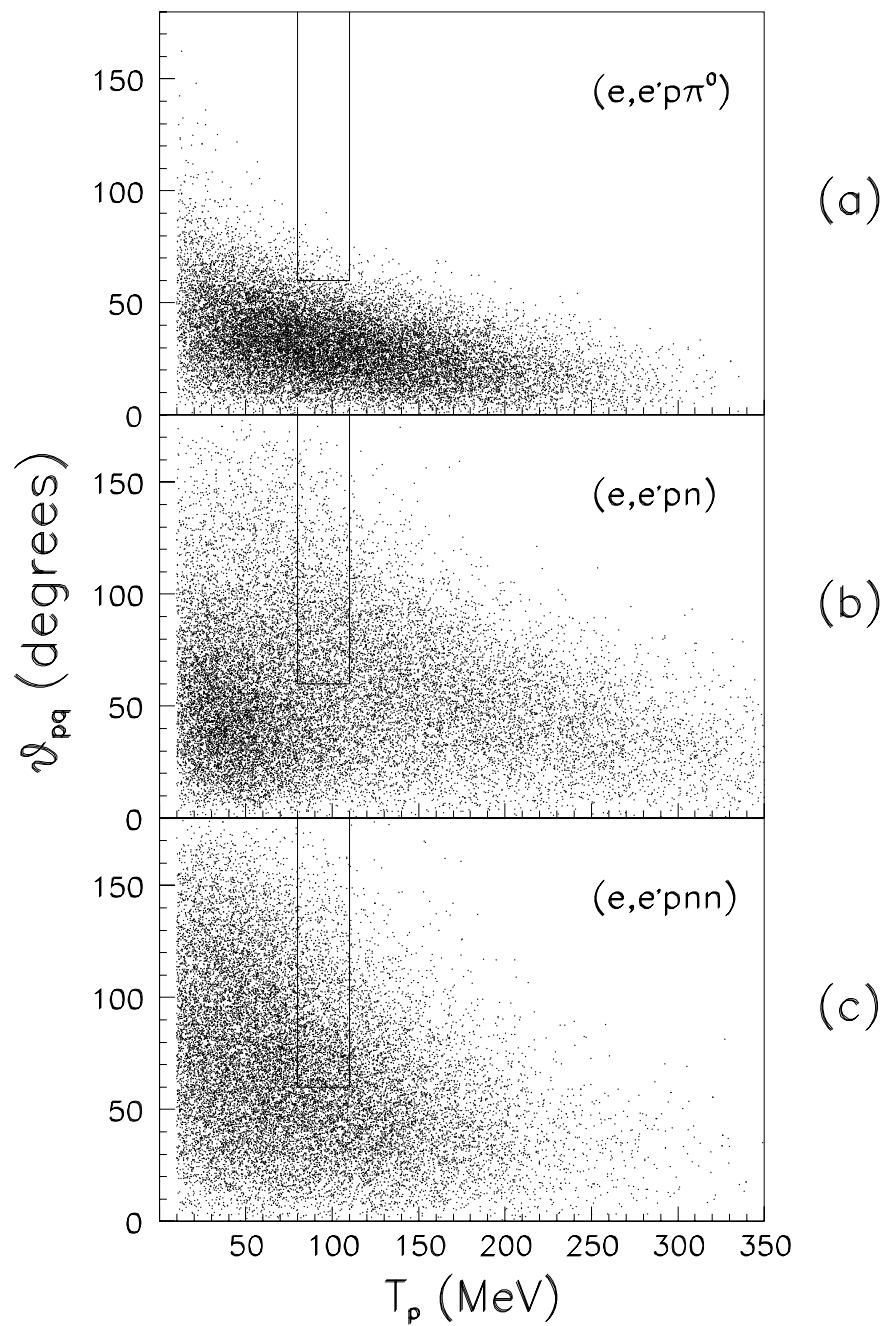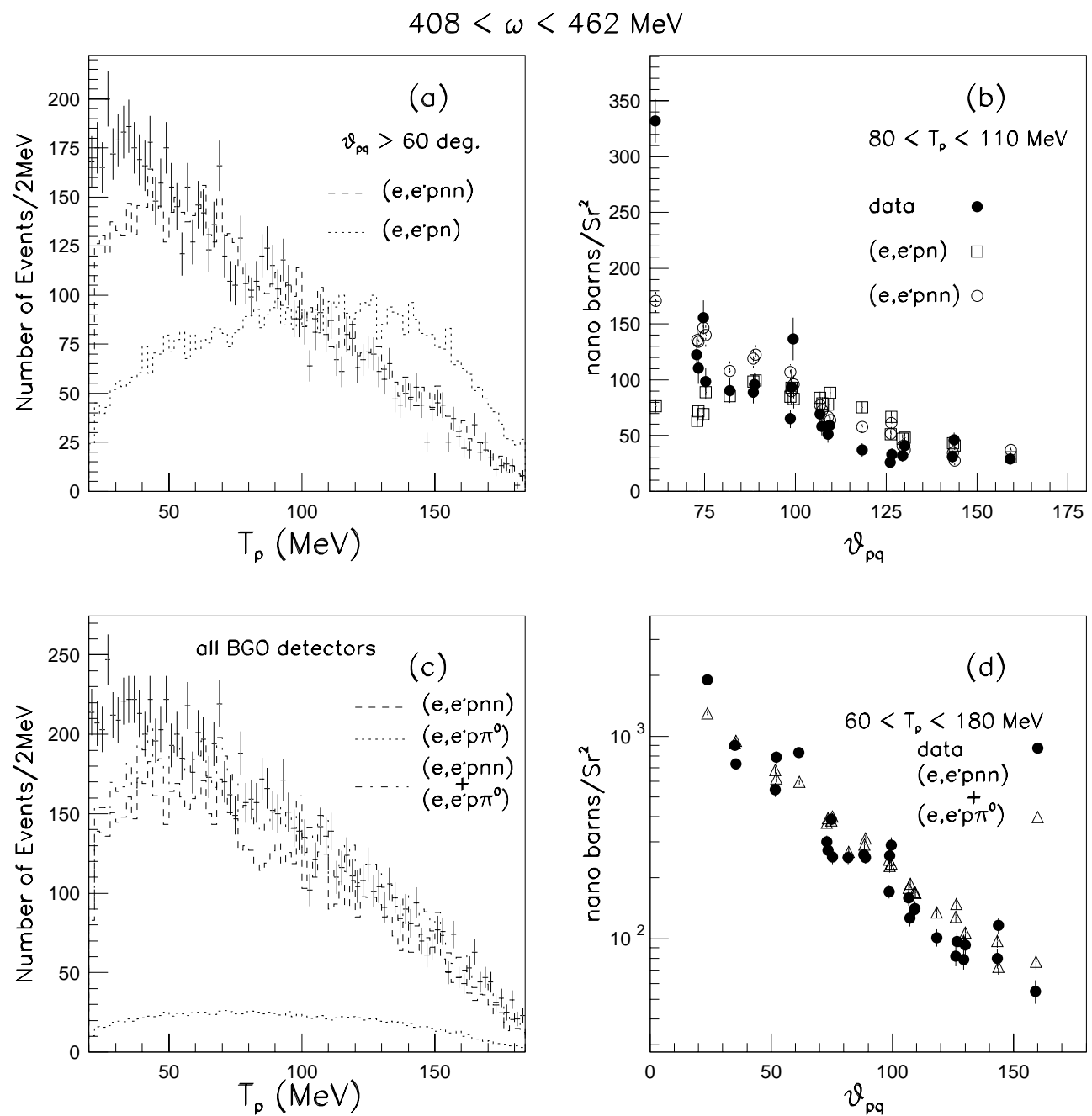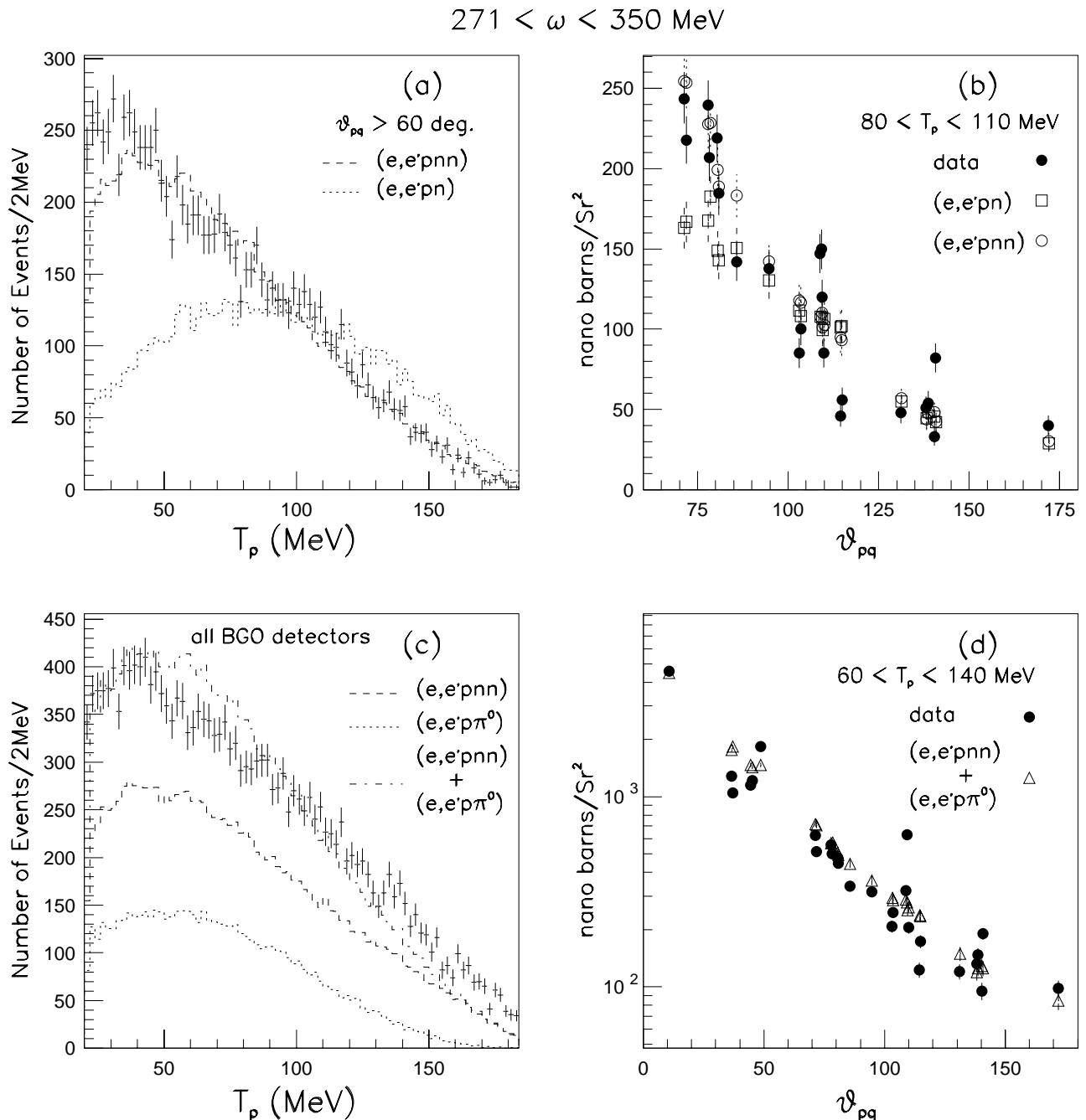
Figure 6.19: Fitting the $(e, e'\ pn)$ reaction into the data spectrum.

Figure 6.20: Right of Δ

$$271 < \omega < 350 \text{ MeV}$$

Figure 6.21: Left of Δ

Chapter 7

Summary and Discussions

In the BGO ball experiment done at MAMI in Mainz, we studied the $^{12}C(e, e'x)$ reaction with a beam energy of 705 MeV and the scattered electrons detected at $34.4°$. The other particles were detected in BGO ball with large angular acceptance in coincidence with the scattered electron. The experiment was carried out for the energy losses from the QE to the Δ region. In this thesis we present the results of the analysis in QE and Δ region. The dip region was investigated independently and some interesting results in $2p$ correlations in $(e, e'pp)$ were obtained by Edelhoff [35] at Mainz.

Most of the results of our analysis are expressed in the form of plots as a function of energy loss of the electron ($E_e - E_{e'}$, or ω), the kinetic energy spectrum (T_p) of the protons, and the angular distribution with respect to $\vec{q}$ (θ_{pq}). None of the plots are corrected for radiative effects. Instead, the results are compared with Monte-Carlo programs which included radiative effects.

7.1 $(e, e'p)$ in Δ region

The highlight of the thesis is the study of $(e, e'p)$ reaction in the Δ region which can be visualized as (γ^*, p) reaction in one photon exchange approximation, where the γ^* is the virtual photon exchanged between the electron and the nucleus. Therefore, comparing the scattered proton kinematically with the virtual photon can give some insight into the nuclear interactions. In this experiment, 28 BGO detectors surrounded the target and each detector was capable of detecting protons in a wide range of energy. The information of the scattered proton can be summarized by the plot of kinetic energy T_p and the angular distribution with respect to $\vec{q}$, θ_{pq}. For interpreting the plots we compared with similar plots obtained from simple models for the $(e, e'pn)$, $(e, e'pnn)$,

and $(e, e'p\pi)$ reactions. These three reactions give a reasonably good fit to the data.

From the study we found that at large angle with respect to $\vec{q}$, there is negligible contribution from $(e, e'p\pi)$ reaction as suggested by Figure 6.12. For $\theta_{pq} > 60°$, the data is fit only by $(e, e'\ pnn)$ and $(e, e'\ pn)$ reactions. It was surprising to see that three-body absorption was sufficient to fit the data for $T_p > 60°$ and $\theta_{pq} > 60°$ (see Figure 6.13).

The procedure for measuring the outgoing proton in coincidence with the scattered electron may not be sensitive to a small contribution of a genuine $(e, e'\ pn)$ reaction. In our experiment we could not study back to back scattering as there was no BGO detectors lying along the direction of $\vec{q}$. Moreover, the BGO detector had low neutron detection efficiency and poor energy measurements.

Since the three-body absorption gives a good fit, it was reasonable to assume that for $\theta_{pq} > 60°$ and $T_p > 60\,\mathrm{MeV}$, the three nucleon absorption contributed entirely to the data. This fit also fixed the strength of the three-body reaction which was useful in later analysis. We further assumed that the extrapolation to all other angles in the simulated three-body events are valid for events with $T_p > 60\,\mathrm{MeV}$. The data for all angles were fit by the previously determined strength of three-nucleon absorption and the rest by $(e, e'p\pi)$ reaction. We found that the data can be explained by 72% $(e, e'\ pnn)$ and 28% $(e, e'p\pi)$ for $T_p > 60\,MeV$.

The dominance of three-body absorption looks similar to a study of the proton distribution in the (π, p) reaction as investigated by McKeown [15] and Ransome [37, 38], where the proton distribution indicates that pions are absorbed in carbon nuclei by about three nucleons. However there is some basic difference in the kinematical aspects of pion absorption and virtual photon absorption reactions.

A pion cannot be absorbed by single nucleon, but only be absorbed by two more nucleons as shown in the Figure 1.3. But a virtual photon can be absorbed by a single nucleon creating Δ which decays to π and N. The outgoing real pion can only be absorbed by two or more nucleons as shown in the Figure 1.3-c. Some theorists call a genuine three-body absorption are where the pions exchanged are virtual as shown in Figure 1.3-c. If the Δ decays and emits a real pion which is again absorbed by two

nucleons, the process is called a FSI.

At this point, it will be interesting to present the opinions of two theorists who hold a different view of photo-absorption on the nuclei. Christillin [36] point out the fact that the photo-absorption per nucleon is much lower for the deuteron compared to lead in and above the dip region suggesting that three-body absorption may play a large part in the medium to heavy sized nuclei. Secondly, he observes that if quasi-deuteron absorption is the dominant mode of photo-absorption, one would naively expect pp and pn pair emission to be comparable because of the fact that M1 $\gamma p \rightarrow p\pi^0$ and E1+M1 $\gamma p \rightarrow n\pi^+$ are comparable, where a pion is re-absorbed on second nucleon. The correct isospin coefficients gives pp and np pairs to be comparable. However the pp channel is experimentally seen to be greatly supressed, indicating that the quasi-deuteron photo-absorption does not explain photo-absorption. In contrast, Oset and his group in Valencia [20] investigated the reaction microscopically and found that around the delta region the $\sigma_{3N}/\sigma_{2N} \sim 1.5$ which suggests the large contribution from two-body absorption.

A recent ^{12}C(γ, p) experiment at NIKHEF also provides an interesting perspective to the two-body and three-body absorptions. The study of proton distributions in ^{12}C(γ, p) was made by Cross [21]. Figures 4–5 in that reference present the photon energy spectrum for various E_γ and various angles of the proton θ_p. The data was compared with a calculation from $2N$, $3N$, $(\gamma, \pi NN)$ and $(\gamma, \pi N)$ process. The full calculation using the Valencia and Gent models from all these processes consistently overestimates the data. The overestimation was largest where the $2N$ contribution was large. That fact seems to indicate that the data could be better explained if $2N$ reactions were significantly suppressed.

In light of the above mentioned theoretical and experimental evidence, our experiment favours a significant suppression of two-body reaction and dominance of the three-body reaction. A back to back scattering experiment could better determine if the two-body reactions are suppressed. The CLAS detectors in Hall B at TJANF seems to be in best position to make such a study with the detection of two or more nucleons with large angular and kinetic energy acceptance detectors. On theoretical side, it will

be interesting to investigate the ways by which the FSI strength could be enhanced. Since real pions are absorbed by at least two nucleons, enhancing the absorption of the real outgoing pion from Δ decay may explain why three-body absorption appears to be larger than two body absorption.

Above and below the Δ region, the results are similar to the Δ region. The data can be explained by $(e, e'\, pnn)$ and $(e, e'\, p\pi^0)$. However it is interesting to see the amount of $(e, e'\, pnn)$ with increasing ω. For higher ω, i.e., where more energy is available, the three-body contribution is 83% — an 11% increase from the Δ region. For lower ω, the $(e, e'\, pnn)$ contribution is 5% lower that the Δ region. This indicates that the disintegration due to three-body process increases with available energy. A similar effect was found for pion absorption.

7.2 $(e, e'p)$ in QE region

In QE region 97% of the outgoing protons were detected in the two BGO detectors which lay in the direction of $\vec{q}$. Hence, we do not have the advantage of studying the angular distribution as in the Δ region. Therefore, we matched only the T_p spectrum with two reactions $(e, e'p)$ and $(e, e'pn)$ which are the most likely candidates and determined their corresponding strength.

As seen in the Figure 6.11, the T_p spectrum gives a good fit with 80% of $(e, e'\, p)$ and 20% $(e, e'\, pn)$ in the range $20 < T_p < 140\,\mathrm{MeV}$.

Our experiment can be compared to other coincidence reaction by MIT-Bates experiment studied by Weinstein [22]. The MIT-Bates experiment had the advantage of measuring the proton energy with high-resolution spectrometer and the data was compared with DWIA calculation. Nevertheless, the protons were detected in a small solid angle. The large extrapolation from small solid angle to 4π could easily be inaccurate if small errors in the model dependence of the fit are present. In our experiment, although the resolution were not as good and the data were compared with a relatively crude model, we had a greater angular acceptance which compensated for the disadvantages to some extent and made our determination of $(e, e'\, p)$ and $(e, e'\, pn)$ strength

relatively accurate.

Since the kinematics of both experiments are different, we cannot make definite comparisons. We observe that one- and two-body processes can sufficiently explain the data and we did not need to invoke three body process. The data do not support 50% two-body absorption in the QE region.

7.3 Position of the Δ peak in coincidence with various final states

As discussed in section 1.5.1, for various hadron reactions the position and width of the Δ peak changes depending on the coincident particle. One explanation of this is the presence of correlations in the longitudinal channel. Because (e, e') is transverse, these correlations should not be present.

As seen in Figure 6.9, most of the coincident reactions do not show a very pronounced peak in the Δ region, and exact determination of the position of the peak, especially without application of radiative corrections, is not possible. However, the maximum cross section of each ofthe $(e, e'\pi)$, $(e, e'$ neutral$)$, and $(e, e'$ 2 neutrals$)$ is within about 20 MeV of the expected peak expected for quasi-free Δ production ($\omega = 360$ MeV), with perhaps a small shift to larger ω. The $(e, e'p)$ cross section does perhaps have a small shift toward smaller ω. However, there is a smooth transition through the dip region, with no clear peak due to the Δ present.

One coincident reaction, $(e, e'pp)$, does clearly shift toward larger ω, with the peak shifted at least 70 MeV, to about 420 MeV. Because of the poor statistics at higher ω the exact location of the peak, and indeed whether or not the cross section is decreasing by $\omega = 500$ MeV, cannot be determined. This is the opposite direction of the shift in hadron reactions.

We cannot conclude that this shift is an indication of a shift of the Δ for two reasons. First, as discussed in Section 6.4, the energy spectra of the protons in the $(e, e'pp)$ reaction are best fit by a four nucleon final state. We see little indication of a direct two nucleon decay. Secondly, the cross section for the reaction is rather small, only about 10% of the final states with a pion or single proton, making it uncertain

how closely tied this final state is to the Δ resonance.

To conclude, no coincidence with various hadrons shows the same large shift to smaller ω that was seen in hadron induced reactions, and the only significant shift, for the $(e, e'pp)$ final state, shifts in the other direction.

Appendix A

How "unfolding" is done

In reference to section 2.4.2, we show the method for isolating the scintillator signal and BGO signal produced in any single BGO detector from the mixture of signals contained in the Short-Gated and Long-Gated ADCs.
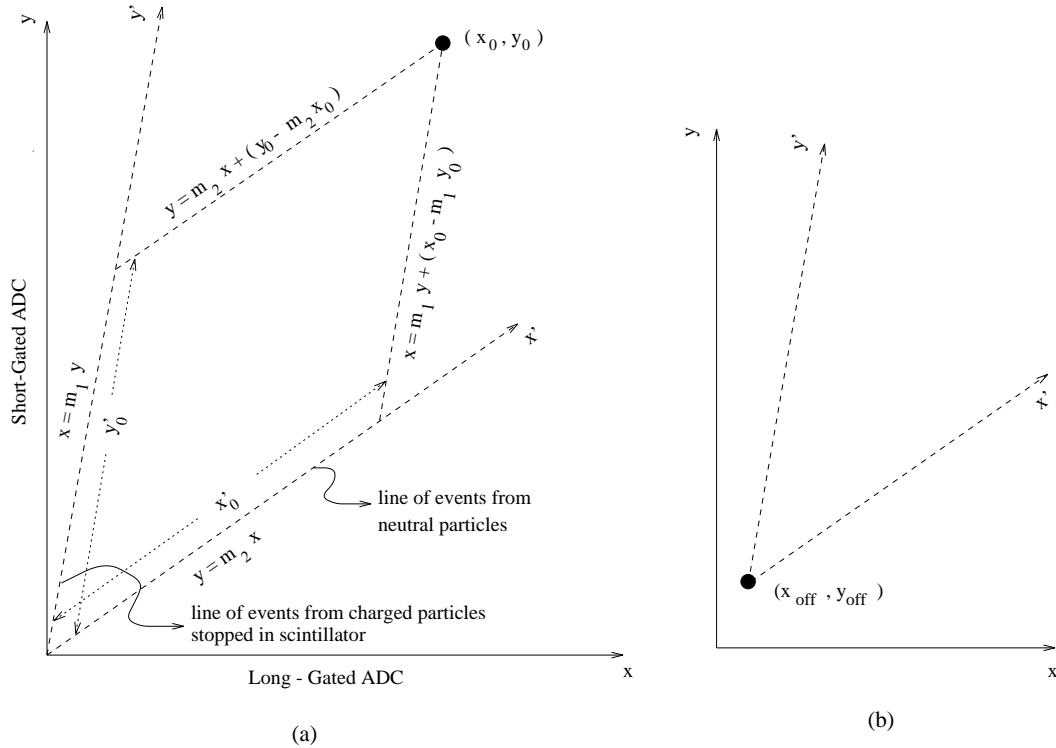
Figure A.1: Outline of MAMI accelerator with various halls

A typical two-dimensional plot of the Short-Gated and Long-Gated ADCs is shown in Figure 2.8. The figure shows most of the events within a bent $\vee$ shaped boundary line. The line close to vertical is due to low energy charged particles which are stopped in scintillator, thus giving only a pure scintillator signal. The other line closer to the horizontal axis is due to neutral particles which produce no signal in the scintillator

and therefore give a pure BGO crystal signal.

We shall use these two lines to isolate the signals. This is done by the transformation of a point, say (x_0, y_0) as shown in Figure A.1(a) in the (x, y) frame with the axes being the Short-Gate ADCs and Long-Gate ADCs to another frame,(x', y'),where the axes are the scintillator signal and the BGO signal.

The ordinate and abscissa of the (x', y') frame passing through (x_0, y_0) are shown in the Figure A.1(a). We wish to find (x'_0, y'_0) which represents the transformation of (x_0, y_0) in the (x', y') frame.

The intersection of the two lines given by:

$$x = m_1 y + (x_0 - m_1 y_0)$$

$$y = m_2 x$$

gives the point from which x'_0 can be evaluated. The point of intersection,

$$\{x_{int}, y_{int}\} = \{1, m_2\} \cdot \frac{(x_0 - m_1 y_0)}{(1 - m_1 m_2)}$$

and,

$$x'_0 = \sqrt{x_{int}^2 + y_{int}^2}$$

$$= (x_0 - m_1 y_0) \cdot \frac{\sqrt{1 + m_2^2}}{(1 - m_1 m_2)}$$

Similarly we find y'_0 from the intersection of the two lines:

$$x = m_1 y$$

$$y = m_2 x + (y_0 - m_2 x_0)$$

$$y'_0 = \sqrt{x_{int}^2 + y_{int}^2}$$

$$= (y_0 - m_2 x_0) \cdot \frac{\sqrt{1 + m_2^2}}{(1 - m_1 m_2)}$$

The factors, $(1 - m_1 m_2)$, $\sqrt{1 + m_2^2}$, $\sqrt{1 + m_1^2}$ involved in the calculation of x_0' or y_0' can be ignored as they are fixed constants for a particular BGO detector which has to be calibrated later for the energy.

If the line of the particle stopped in scintillator and line of neutrals do not intersect at zero and have an offset, $\{x_{\text{off}}, y_{\text{off}}\}$ as shown in Figure A.1(b), then the transformation is given by:

$$x_0 \quad \rightarrow \quad (x_0 - x_{\text{off}}) - m_1 (y_0 - y_{\text{off}})$$

$$y_0 \quad \rightarrow \quad (y_0 - y_{\text{off}}) - m_2 (x_0 - x_{\text{off}})$$

Appendix B

Details of ENIGMA

B.1 ENIGMA, the event generator for simulation program

The simulation program, ENIGMA (Electro-Nuclear Interaction Generator by Monte-Carlo Approach), created by J. Visschers is an event generator for electron-, photon- or pion-induced reactions on a nucleon or nuclei with beam energies between 500 MeV and 1.5 GeV. Table B.1 shows the reactions which can be simulated by ENIGMA.

In order to run the program, ENIGMA requires the information about the detectors. In our case we specified the description of electron-arm-spectrometer and BGO ball detectors in files: SPEC and BGO respectively. The contents of the two files are shown below:

FILE: SPEC

```
rectangular
34.4                spectrometer theta in degrees    [0<=theta<=180]
0.                  spectrometer fi in degrees       [0<=fi(360]
13.99 20.14 100     out,in-plane dim,distance from target
1                   efficiency               [0<=eta<=1]
200                 lower kinetic energy threshold   [MeV]
660                 higher kinetic energy threshold  [MeV]
0                   energy resolution only for histograms  [sigma, MeV]
0        1          (only electron) min and max mass thresholds [MeV/c^2]
-1       -1         minimal and maximal charge thresholds
1                   [-1: veto, 0: out-of-trigger, 1: in trigger]
3                   [0: no output, 1: histo, 2: events, 3:histo+events]
```

FILE: BGO

```
circular
90              theta in degrees (0<=theta<=180)
90              fi in degrees (0<=fi<360)
12.7            (4 Pi) solid angle  in sterradian (0<=omega<=12.7)
1               efficiency 0<=eta<=1
10               min kin energy in MeV
400             max kin energy in MeV
0               energy resolution
1        1000   minimal and maximal mass (avoid electrons)
-1       1      minimal and maximal charge
1               -1: veto, 0: out-of-trigger, 1: in trigger
3               0: no output, 1: histo, 2: list 3:histo+list
```

Reaction	Comments
$A(\gamma, p\pi^-)A - 1$	pion photo-production
$A(\gamma, p\pi^0)A - 1$	" "
$A(\gamma, n\pi^0)A - 1$	" "
$A(\gamma, n\pi^+)A - 1$	" "
$A(\gamma, pn)A - 2$	[Quasi-]deuteron photo dissociation
$A(e, e'p)A - 1$	Quasi Free proton knockout
$A(e.e'n)A - 1$	Quasi Free neutron knockout
$A(e, e'pn)A - 2$	Quasi ^{2}H electro-dissociation
$A(e, e'pnn)A - 3$	Quasi ^{3}H disintegration
$A(e, e'ppn)A - 3$	Quasi ^{3}He disintegration
$A(e, e'ppnn)A - 4$	Quasi ^{4}He disintegration
$d(e, e'pn)$	(Arenhoevels ^{2}H-formalism) (in preparation)
$A(e, e'p\pi^-)A - 1$	QF pion electro production
$A(e, e'p\pi^0)A - 1$	" "
$A(e, e'n\pi^0)A - 1$	" "
$A(e, e'n\pi^+)A - 1$	" "
$A(e, e'\pi^+)A(Z - 1)$	coherent π^+ production
$A(e, e'\pi^0)A$	coherent π^0 production
$A(e, e'\pi^-)A(Z + 1)$	coherent π^- production
$A(\pi^+, pp)A - 2$	[Quasi-]^{2}H absorption
$A(\pi^+, pd)A - 3$	[Quasi-]^{3}H absorption
$A(\pi^+, ppn)A - 3$	" "
$A(\pi^+, dd)A - 4$	[Quasi-]^{4}H absorption
$A(\pi^+, ppp)A - 3$	[Quasi-]^{3}He absorption
$A(\pi^+, ppd)A - 4$	[Quasi-]^{4}He absorption
$A(\pi^+, pppn)A - 4$	" "
$A(\pi^+, pppnn)A - 5$	[Quasi-]^{5}He absorption

Table B.1: Reactions which can be simulated by ENIGMA

The file SPEC places the electron-arm-spectrometer at an angle of $34.4°$ and defines a rectangular collimator with dimensions 13.99×20.14 cm^2 at a distance of 100 cm. These dimensions are chosen to give a solid angle of ~ 28 msr. We assume the spectrometer detects electrons of kinetic energy in a range of $200 - 660$ Mev with 100% efficiency. The range covers all the regions – Quasi-Elastic to beyond the Δ-region. We can select only the electrons to be scattered in the spectrometer by specifying the charge of the particle to be -1 e with the mass between $0 - 1$ MeV/c^2.

The BGO ball detector is defined in a simple manner as GEANT has the detailed geometric specification. It is specified as a circular collimator with a solid angle of

4π or 12.7 Sr. The specification of `theta` and `fi` is necessary to correctly orient the momentum of outgoing particles with respect to electron's momentum. We detect the particles in the range of kinetic energy $10 - 400$ Mev with 100% efficiency. The particles can be pions, neutrons, or protons as they have charge between $-1 and + 1$ e and the mass within $1 - 1000$ Mev/cm^2

The program is run by the following command in SUN/UNIX:

```
enigma \
-tables ~/enigma/tables \
-det1 SPEC \
-det2 BGO \
-process eepnn \
-target 12C \
-Tbeam 705 \
-lumin 1e32  \
-incmframe off \
-logfile log.txt \
-bremsstrahlung on \
-time 10000
```

It requires the information from the lookup table in the directory $\tilde{}$`/enigma/table` and the description of the detectors `det1` and `det2` described in the file `SPEC` and `BGO`. The above mentioned program simulates the process A(e,e'pnn)A-3 with a beam energy of 705 MeV on a ^{12}C target. The bremsstrahlung is included making it suitable for comparison with data which are not radiatively corrected.

The program generates an output which can be stored in a file. Many such runs can be performed and the output files of events summed to get a large number of events for better statistics. Two such events are shown below, where the first line shows the number of particles detected in the detectors followed by the particle and their momentum and energy. The events are spaced by an empty line.

OUTPUT FILE: (only two events are shown)

```
   4
e-      2.94393e+02  1.72820e+02 -9.13088e+00  2.38153e+02  SPEC
1H      9.85072e+02 -2.93631e+01  2.92669e+02 -5.91146e+01  BGO
1n      9.94983e+02 -7.33425e+01  2.61850e+02 -1.82382e+02  BGO
1n      1.17502e+03  4.83761e+02 -4.94216e+02  1.40079e+02  BGO

   4
e-      5.11648e+02  2.97818e+02 -3.30428e+01  4.14724e+02  SPEC
1H      9.90823e+02 -3.07574e+02  6.70000e+01  4.77988e+01  BGO
1n      1.02195e+03  3.05928e+02  5.49689e+00  2.60712e+02  BGO
1n      9.54859e+02  5.39623e+00  4.61086e+01  1.63757e+02  BGO
```

Appendix C

Bremsstrahlung

In electron scattering experiments, a significant fraction of electrons loose some of their energy in the presence of an electromagnetic field by emitting photons. This process is called bremsstrahlung and can be completely explained by QED. It is important to take into account as it is unrelated to the nuclear process of interest and only affects the electron probe. The Feynman diagrams which give the major contributions to the bremsstrahlung is shown in Figure C.1.
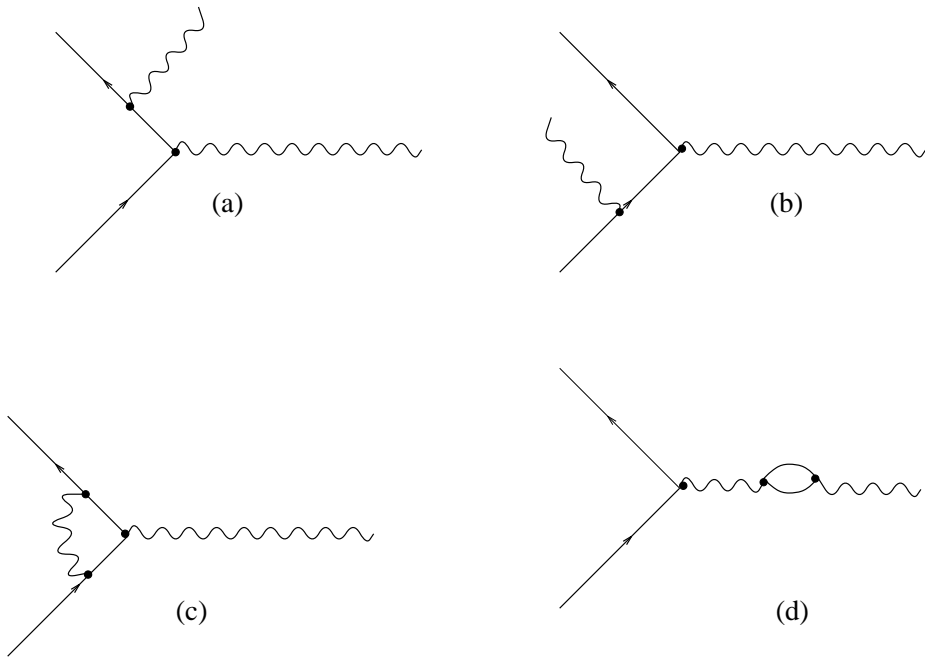
Figure C.1: Feynman diagrams giving major contributions to radiative process. Solid lines represents the electron and wavy lines represent the photons.

In our experiment, we compared the data with the models which included the bremsstrahlung process. In this way we avoided the complicated procedure of "unfolding" the data without affecting any of the conclusions. The details of the radiative

unfolding procedure can be seen in [41].
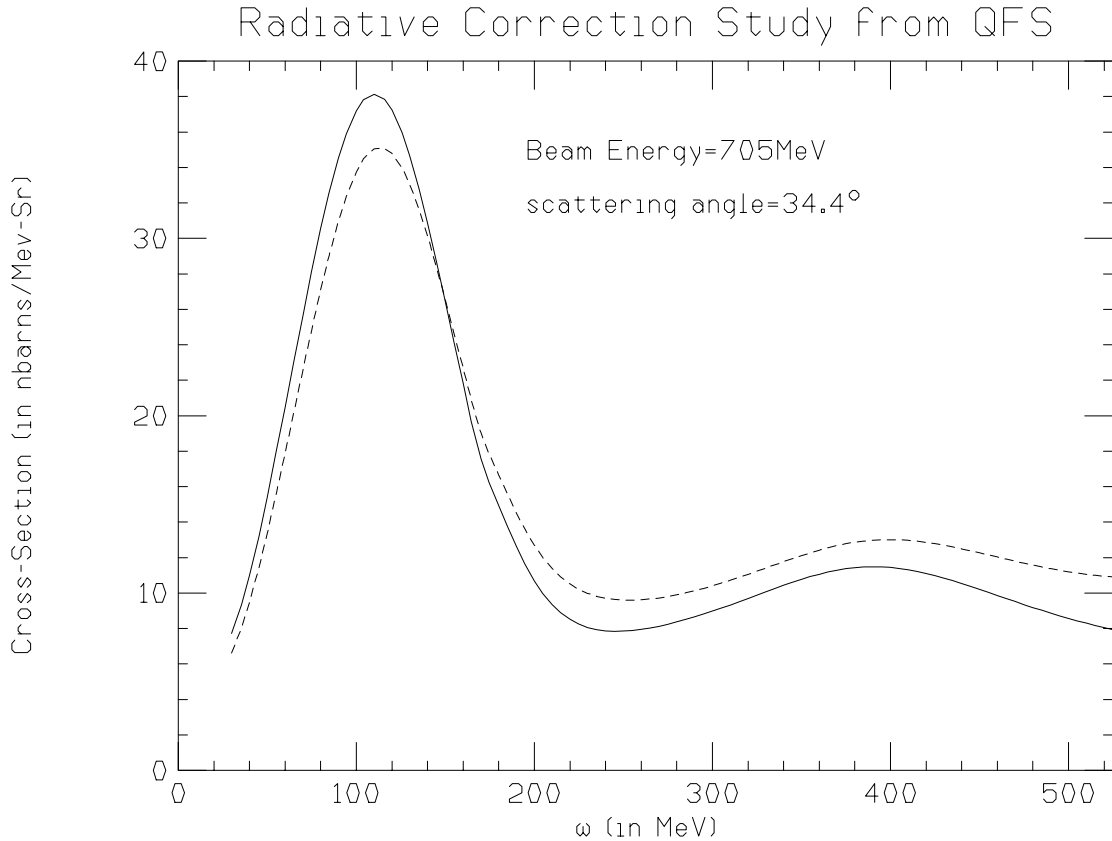
Figure C.2: Cross section of (e, e') predicted by QFS program. Dashed line represent the cross section which includes the bremsstrahlung process.

Figure C.2 shows the ω spectrum predicted by O'Connel's QFS program with and without bremsstrahlung process. The dashed curve which includes the radiative process can be compared with the data in the Figure 6.5 and is found to be in good agreement with the data. Similarly, we included the bremsstrahlung process in all the processes simulated by the ENIGMA event generator.

Appendix D

Making the basic GEANT program

The GEANT software, which is popular in the Intermediate/High Energy community as a simulation tool to optimize detectors or study the bias due to geometrical acceptance, can be daunting for the beginner. Therefore it is worthwhile to describe some of my learning experience. The GEANT software is fairly elaborate program and I describe the making of a GEANT program in relation to our experiment. I divide the learning process in the sections as follows:

D.1 Getting acquainted

I borrowed the template given in the GEANT manual BASE100-1[*] as a startup program. This consist of `common` statements and calling many `subroutines` in a proper sequence for the GEANT program to run smoothly. It also helps to have couple of different workable programs to learn and get confidence in running the program.

In the template program, the subroutines which are called or defined have a first or first-two letters based on the following convention:

1. All the subroutines beginning with letter "G" but is not followed by "U" are defined in the GEANT library. Thus it may just be called and defined by the user. For instance, subroutines `GINIT`, `GPART`, `GMATE`, `GRUN` and `GLAST` are called but not defined by the user.

2. The subroutines beginning with prefix "GU" may be defined by user but not called in the program as it is called in the subroutines in the library. For example, subroutine `GUKINE` has to be defined by the user where the kinematics of the

---

[*]All reference to GEANT manual is from Long Writeup W5013, March 1994 edition

events are created or read. However it should be called by the user as it is called by subroutine GRUN once when each event is processed. Therefore care must be taken to call the GEANT-defined subroutine which in turn calls the user-defined subroutine.

3. Other subroutines beginning with letter "H" are not related to GEANT but are defined in the HBOOK libraries.

We avoided the graphic subroutines, GDINIT and the ones beginning with "I" because Interactive GEANT gave a better control over the program for debugging with graphics. Moreover we did not need graphics when running the program non-interactively.

D.2   Defining the medium parameters of the detectors

Before we could define the geometry of detectors, we had to define the various media of the detectors. The information for standard materials such as aluminum are loaded by calling GMATE. The other materials like scintillator or BGO are mixture of various compounds which are not recognized by GEANT. Therefore, it had to be defined in the program and it was done by adding the following lines:

For BGO compound ($Bi_4Ge_3O_12$)

```
c        BGO compound parameters
         real ABGO(3),ZBGO(3),wBGO(3)
         data ABGO,ZBGO,wBGO/208.98,72.59,15.999,83.,32.,8.,4.,3.,12./
         call gsmixt(21,'bgo compound',ABGO,ZBGO,7.1,-3,wBGO) ! CONS110-1
```

For scintillator compound (CH)

```
c        scintillator parameters
         real Ascin(2),Zscin(2),wscin(2)
         data Ascin,Zscin,wscin/12.01,1.01,6.,1.,1.,1./
         call gsmixt(23,'scintillator',Ascin,Zscin,1.032,-2,wscin) ! CONS110-1
```

Once all the media are defined, GSTMED is called for each defined medium. Here the medium is labeled by tracking medium number, and name and sensitivity flag ISVOL is given. The flag indicates that if ISVOL > 0, the program will retain quantities like energy loss at each step as the particle passes through the medium. It is needed when the information is to be retrieved, as elaborated in Section D.5.

D.3 Setting up of Geometry

After defining the medium of each detector, we were ready to "build" the detectors with right geometry. This was, by far, the most formidable task of the programming, as the geometry of BGO ball is non-trivial. Firstly we defined a mother volume as a box which would include all the detectors and the trajectory of the particles. Then we "made" the beam pipe, magnets, single BGO detectors with the basic shapes which are understood by the GEANT software. Currently the software recognizes sixteen basic shapes (see GEOM050-1) and we made use of the shapes, such as box, tube, trapezoid, and polygon to construct all the geometry. The shapes and parameters of the single magnet, pentagonal BGO detector, and hexagonal BGO detector are shown in Figure D.1. The hexagonal detectors could not be accommodated by any of the GEANT recognizable shapes and therefore was made by combining two trapazoidal shapes as shown in Figure D.1.

Each basic shape is specified by calling subroutine GSVOLU where the name, parameters, and meduim for the shapes are given. The basic shape is then placed by calling subroutines GSROTM and GSPOS which rotates and translates the volume to the required position.

As the geometry was being constructed, it was helpful to see the three-dimensional geometry in the interactive geant mode and check for obvious inconsistencies.

D.4 Reading events

The information of simulated particles are fed through the subroutine gukine which is read by GEANT program once for each event processed. In this subroutine the simulated particles may be created or read from a file. We used the ENIGMA program to simulate various reactions and the output was stored in a file. In the subroutine GUKINE entire events are read which contain the momentum and identity of particles. The information of vertex, momentum and identity is fed to GEANT program by calling GSVERT and GSKINE in the subroutine GUKINE. The subroutine GSKINE was called once for each particle in the event. (GSVERT was called only once per event as the vertex of

all scattered particles was the same). GEANT keeps track of the particles by assigning a number for the track in variable, `ITRA`. For instance, if `GSKINE` was called three times by putting the momentum information for electron, proton, and pion, then `ITRA` will be assigned number 1,2 and 3 for electron, proton, and pions respectively for that event.

D.5 Retrieving relevant information

Defining of the geometry and feeding the kinematics of the particles are sufficient condition for the GEANT program to run smoothly. In fact, the detectors and the trajectory of the particles could be visualized through the graphics produced by interactive GEANT. This can serve as a powerful tool for debugging the geometry of the detectors and the simulation of the particles, but cannot be used for retrieving the information.

It is necessary to extract the relevant information such as energy deposited in various elements and the identification of those elements. All this information can be retrieved via hundreds of variables in the common blocks defined in the GEANT library. The entire list of common blocks is given in ZZZZ010-1 of the manual.

We stored the information in the form of ntuples which contained the momenta of the electron and proton before scattering; energy deposited by the proton in the magnets, scintillaotr, and BGO detector; the identity of the magnets, scintillators, and BGO crystal where the energy was deposited. The aforementioned information is stored for each event.

In order to create ntuples, the variables for the ntuples have to be defined (initialized), filled event by event, and ended in a graceful manner as demanded by HBOOK software. The HBOOK software is another package from CERN for making histograms and ntuples. We defined the HBOOK variables in subroutine, `UGINIT` (called only once), filled the ntuples in subtoutine, `GUOUT` (called after each each event is processed) and end HBOOK routines are put in subroutine `UGLAST` (called only once at the end of processing all the required events).

So far we have not mentioned an important user defined subroutine - `GUSTEP`. In this subroutine most of the relevant information is extracted by manipulating the information from the variables defined in the common blocks. The GEANT program calls

the subroutine after the particle has traveled a certain distance or "step". The step size is automatically decided by the GEANT program. The step size is also based on the values assigned to variables when calling GSTMED (see CONS200-1). For instance, when the fractional energy loss of particle exceeds the maximum fractional energy loss in one step or the particle cross the medium beyond the user defined precision, the GEANT calls the subroutine GUSTEP.

In the subroutine, GUSTEP we calculate the relevant information such as total energy lost in a detector element by summing the energy loss at each step until it cross the boundary of the detector. The relevant information is then passed through the common block to subroutine GUOUT to fill the relevant information.

| variable	common block	description
IEORUN	GCFLAG	flag to terminate run if non-zero
DESTEP	GCTRAK	energy lost in current step
IDTYPE	GCSETS	user defined detector type
ITRA	GCKINE	track number

Figure D.1: The magnets (MAG) and pentagonal BGO detector(PNTB) was created as a single piece shape recognized by the GEANT program. The hexagonal BGO detector was made up of two pieces (HX1B and HX2B) placed on the top of each other. The figure was created by the command DSPEC *name* in interactive GEANT mode.

Appendix E

Cross-section calculation

In the analysis we often obtain histograms given by number of events per bin and it is useful to convert into cross-section which serves as a standard for comparison with theory or other experiments. In the following sections, we give some explanation and formulas, specific to each cases, for converting the event plots into cross-sections.

Firstly we mention some numbers which will be utilized in evaluation of cross-section.

- TARGET: The target was specified as $10\,\mathrm{mg/cm^2}$ which is converted to convenient units as follows:

$$\text{target thickness in our experiment} = 10\,\tfrac{\mathrm{mg}}{\mathrm{cm^2}} \cdot \tfrac{6.022\times10^{23}}{12\,\mathrm{g\ of\ ^{12}C}} \cdot \tfrac{10^{-33}\,\mathrm{cm^2}}{1\,\mathrm{nbarn}}$$
$$= 5.0183 \times 10^{-13}/\,\mathrm{nbarn}$$

- The incident electrons from the beam in various region was complied by the Edelhoff [35] and is given in the Table E.1

Region	ω (in MeV)	incident electrons
QE	45 - 165	92.18×10^{13}
dip	185.8 - 280.2	460.98×10^{13}
LoD	271.16 - 350.04	1025.46×10^{13}
ToD	348.6 - 413.4	2839.24×10^{13}
RoD	408 - 462	1080.80×10^{13}
VRoD	458.6 - 503.4	292.46×10^{13}

Table E.1: The incident electrons in various region used for calculating cross sections

E.1 For ω plots of all reactions

In the one photon exchange approximation, ω represents the energy of the virtual photon exchanged between electron and nuclei. The other factors determining the cross-section are the beam energy E_e and the scattering angle $\theta_{e'}$, which a completely specifies the virtual photon by $\vec{q}$, ω and its polarization.

Cross-section is given by,

$$\sigma(E_e) = \frac{N_{scat}}{N_{inc} \cdot (\text{target thickness})} \tag{E.1}$$

Also,

$$
\begin{aligned}
\sigma(E_e) &= \int \frac{d^2\sigma(E_{e'}, \theta_{e'}, \omega)}{d\Omega_{e'} d\omega} \cdot d\theta_{e'} \cdot d\omega \\
&= \frac{d^2\sigma(E_{e'}, \theta_{e'}, \omega)}{d\Omega_{e'} d\omega} \cdot \int d\theta_{e'} \cdot \int d\omega \\
&= \frac{d^2\sigma(E_{e'}, \theta_{e'}, \omega)}{d\theta_{e'} d\omega} \cdot \Delta\theta_{e'} \cdot \Delta\omega
\end{aligned}
\tag{E.2}
$$

Where,

N_{scat} Number of scattered electrons in the collimator and in the single bin in ω plot.

N_{inc} Number of electrons from the beam on the target

$\Delta\Omega_{e'}$ The solid angle of the collimator where the scattered electron are detected

$\Delta\omega$ The size of the bin in omega spectrum

In the above steps the cross-section, $\frac{d^2\sigma(E_{e'}, \theta_{e'}, \omega)}{d\Omega_{e'} d\omega}$, is assumed to be a constant in the integrated region which is over the collimator, $\Delta\Omega_{e'}$ and over the histogram bin, $\Delta\omega$. The assumptions are reasonable because the solid angle of the collimator and the bin chosen in the ω spectrum are very small.

Equating E.1 and E.2 relations, we obtain:

$$\frac{d^2\sigma(E_{e'}, \theta_{e'}, \omega)}{d\Omega_{e'} d\omega} = \frac{N_{scat}}{N_{inc} \cdot (\text{target thickness}) \cdot \Delta\Omega_{e'} \cdot \Delta\omega} \tag{E.3}$$

$\Delta\omega$ is 8 MeV for $(e, e'pp)$ reaction and 3 MeV for all other reactions in ω spectra. $\Delta\Omega_{e'}$ is 28 msr. The above formula provides the conversion of N_{scat} to the cross-section.

E.2 For θ_{pq} plot for $(e, e'\ p)$ inclusive reaction

In the $(e, e'\ p)$ reaction, we have additional factors such as T_p and θ_{pq} compared to (e, e') which affect the cross-section. The cross-section for the inclusive reaction $(e, e'\ p)$ in relation to our experiment can be best expressed as $d^2\sigma/d\Omega_{e'}d\Omega_{pq}$. The cross-section for the given beam energy, and given range of ω and T_p can be evaluated as follows:

$$\text{cross-section} = \frac{N_{scat}}{N_{inc} \cdot (\text{target thicknesss})} \tag{E.4}$$

Also,

$$
\begin{aligned}
\text{cross-section} \quad &= \quad \int \frac{d^2\sigma_{(\theta_{e'}, \theta_{pq})}}{d\Omega_{e'} \cdot d\Omega_{pq}} \cdot d\Omega_{e'} \cdot d\Omega_{pq} \\
&= \quad \frac{d^2\sigma_{(\theta_{e'}, \theta_{pq})}}{d\Omega_{e'} \cdot d\Omega_{pq}} \cdot \int d\Omega_{e'} \cdot \int d\Omega_{pq} \\
&= \quad \frac{d^2\sigma_{(\theta_{e'}, \theta_{pq})}}{d\Omega_{e'} \cdot d\Omega_{pq}} \cdot \Delta\Omega_{e'} \cdot \Delta\Omega_{pq} \tag{E.5}
\end{aligned}
$$

In the above steps we have assumed that $\frac{d^2\sigma_{(\theta_e, \theta_{pq})}}{d\Omega_{e'} \cdot d\Omega_{pq}}$ to be constant in the integrated region over the collimator where the scattered electrons are detected and the single BGO detector which detects the protons. We have made the assumptions for the following reasons:

- The acceptance of the scattered electron has a small solid-angle (28msr) and we do not expect the cross-section to change within the solid angle.

- The acceptance of the scattered proton is not small (max $\sim 4\pi/32$ sr) and the cross-section may change within that solid angle. However, the cross section is a function of θ_{pq} and change in the cross-sections can be seen by adjacent data points.

From equations E.4 and E.5 we have the formula for conversion:

$$\frac{d^2\sigma_{(\theta_e, \theta_{pq})}}{d\Omega_{e'} \cdot d\Omega_{pq}} = \frac{N_{scat}}{N_{inc} \cdot (\text{target thickness}) \cdot \Delta\Omega_{e'} \cdot \Delta\Omega_{pq}} \tag{E.6}$$

A single BGO detector had a solid angle of $\sim 4\pi/32$ sr. However the array of permanent magnets reduced the active area of the BGO detector. We give the active

area of the BGO detector taking the magnets into consideration in Table E.2. In the

BGO #	1	2	3	4	5	6	7	8
% active (f)	37.47	-	57.19	69.74	85.63	58.13	28.77	28.54
BGO #	9	10	11	12	13	14	15	16
% active (f)	76.50	57.91	-	36.88	65.95	57.89	65.90	92.66
BGO #	17	18	19	20	21	22	23	24
% active (f)	98.93	92.95	85.76	86.16	100	100	100	100
BGO #	25	26	27	28	29	30	-	-
% active (f)	100	100	100	100	100	100	-	-

Table E.2: BGO detector number and the corresponding percentage of solid angle not covered by the magnets.

BGO #	4	3	14	7	8	5	13	15
$\theta_{pq}(deg.)$	18.52	35.21	35.63	48.65	49.16	56.44	73.31	73.87
BGO #	6	10	19	20	9	23	1	12
$\theta_{pq}(deg.)$	75.96	76.37	84.21	84.79	87.05	93.46	102.95	103.48
BGO #	21	22	16	18	29	30	17	24
$\theta_{pq}(deg.)$	106.76	107.26	107.95	108.46	121.53	121.83	123.57	133.13
BGO #	25	26	28	27	-	-	-	-
$\theta_{pq}(deg.)$	133.71	142.59	143.05	164.30	-	-	-	-

Table E.3: BGO detector number and corresponding θ_{pq} with respect to $\vec{q}$

θ_{pq} plots each data point was artificially separated so that each data point represents events from single BGO detector. The separation is not significant but it puts the data point in different bins of the histogram. The BGO number with increasing θ_{pq} for the ToD region is given in the Table E.3.

References

[1] J. W. Van Orden, T. W. Donnelly, Ann. Phys. **131**, 451 (1981).

[2] T. deForest, Jr., J. D. Walecka, Adv. Phys. **15**, 1 (1966).

[3] E.J. Moniz, *et al.*, Phys. Rev. Lett. **26**, 445 (1971).

[4] R. W. Lourie, Page 485, Relativistic Dynamics and Quark-Nuclear Physics, Edited by M.B. Johnson and A. Picklesimer, John Wiley & Sons (1986).

[5] J. V. Noble, Phys. Rev. Lett. **46**, 412 (1981).

[6] I. Sick, Phys. Lett. **157B**, 13 (1985).

[7] P. J. Mulders, Nucl. Phys. **A459**, 525 (1986).

[8] D. H. Perkins, Page 131, Introduction to High Energy Physics, Addison-Wesley publishing company (1987).

[9] R. M. Sealock, *et al.*, Phys. Rev. Lett. **62**, 1350 (1989).

[10] H. J. Weyer, Page 445, Pions in Nuclei, Edited by E. Oset, it et al., World Scientific Publishing Co. (1992). (Integrated cross-section, $\sigma_{2N(I=0)}$ is plotted for various pion energies from various experiments).

[11] T. Hennino, *et al.*, Phys. Lett. **B283**, 42 (1992).

[12] T. Hennino, Page 83, RIKEN international workshop on Delta Excitation in Nuclei, Edited by H. Toki, it et al., World Scientific (1994).

[13] T. Udagawa, *et al.*, Phys. Lett. **B 245**, 1 (1990).

[14] J. Chiba,*et al.*, Phys. Rev. Lett. **67**, 1982 (1991).

[15] R. D. McKeown, *et al.*, Phys. Rev. Lett. **44**, 1033 (1980).

[16] W. J. Burger, *et al.*, Phys. Rev. Lett. **57**, 58 (1986) and Phys. Rev. C **41**, 2215 (1990).

[17] D. Ashrey, *et al.*, Phys. Rev. C **23**, 2173 (1981) (a compilation of $\pi^{\pm}$ nucleus cross-sections and true $\pi^{\pm}$ absorption cross-sections are given for Li, C, Al, Fe, Nb, and Bi at pion energies: 85, 125, 165, 205, 245, 315 MeV).

[18] T. Takaki, Phys. Rev. C **39**, 359 (1989).

[19] G. P. Capitani *et al.*, Nuovo Cimento **85A**, 37,(1985).

[20] E. Oset, *et al.*, Phys. Rev. C **53**, 305 (1996).

[21] G. E. Cross, *et al.*, Nucl. Phys. **A 593**, 463 (1995).

[22] L. B. Weinstein, *et al.*, Phys. Rev. C **50**, 350 (1994).

[23] R. K. Bock, *et al.* Data analysis techniques for high-energy physics experiments, Edited by M. Regler, Cambridge University Press (1990).

[24] E. J. Moniz, Nucl. Phys. **A354**, 535c (1981).

[25] R. Neuhausen, Nucl. Phys. B (Proc. Suppl.)**44**, 695 (1995).

[26] R. D. Ransome, *et al.*, Phys. Rev. Lett. **64**, 372 (1990); Phys. Rev. C **42**, 1500 (1900).

[27] R. W. Lourie, *et al.*, Phys. Rev. Lett. **56**, 2364 (1986).

[28] T. deForest, Jr., Nucl. Phys. **A392**, 232 (1983).

[29] J. Visschers Page 350, MC93 International conference on Monte Carlo Simulation in High Energy and Nuclear Physics, Edited by P. Dragovitsch, S. L. Linn, and M. Burbank, World Scientific (1994).

[30] A. Richter, *Trennung des longitudinalen, transversalen und longitudinal-transversal interferierenden Anteils des Wirkunsquerschnitts der Reaktion* $H(e, e'\pi^+)$ *in der Nähe der Pionschwelle*, Dissertation, Institut für Kernphysik, Universität Mainz, 1995.

[31] E. A. J. M Offermann, Ph.D. Thesis, NIKEF–K (1988).

[32] K. L. Brown, SLAC report-75, June 1982.

[33] R. D. Ransome (private communication based on previous experiments with LAMPF BGO ball).

[34] M. K. Jones, Phys. Rev. C **48**, 2800 (1993).

[35] Dissertation in preparation, Institut für Kernphysik, Universität Mainz, 1997.

[36] P. Christillin, Phys. Rep. **190**, 63 (1990).

[37] R. D. Ransome, *et al.*, Phys. Rev. C **45**, R509 (1992).

[38] R. D. Ransome, *et al.*, Phys. Rev. C **46**, 273 (1992).

[39] W. J. Burger, *et al.*, Phys. Rev. C **41**, 2215 (1990).

[40] J.W. Lightbody, Jr. and J.S. O'Connell, Computers in Physics, May/June, page 57, 1988.

[41] E. Quint, Ph.D Thesis, University of Amsterdam (1988).